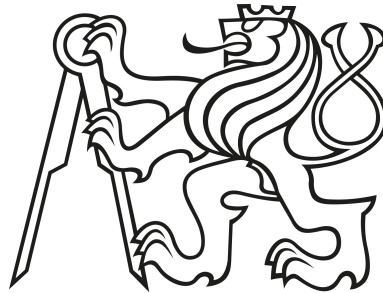


CZECH TECHNICAL UNIVERSITY IN PRAGUE
Faculty of Nuclear Sciences and Physical Engineering
Department of Physics



Master's Thesis

**Production of non-photonic electrons in U+U
collisions at 193 GeV in STAR experiment**

Bc. Katarína Gajdošová

Supervisor: Mgr. Jaroslav Bielčík, Ph.D.

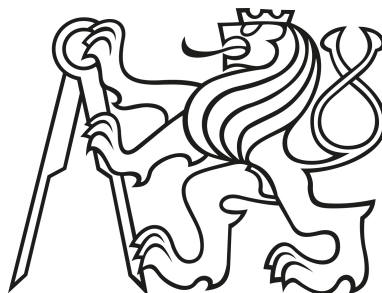
Consultants: Dr. Mustafa Mustafa, Ing. Olga Rusňáková

Prague, 2015

ČESKÉ VYSOKÉ UČENÍ TECHNICKÉ
V PRAZE

Fakulta jaderná a fyzikálně inženýrská

Katedra fyziky



Diplomová práce

**Produkce nefotonických elektronů v srážkách
 $U+U$ s energií 193 GeV v experimentu STAR**

Bc. Katarína Gajdošová

Vedúci práce: Mgr. Jaroslav Bielčík, Ph.D.

Konzultanti: Dr. Mustafa Mustafa, Ing. Olga Rusňáková

Praha, 2015

Prehlásenie

Prehlasujem, že som svoju diplomovú prácu vypracovala samostatne a použila som len literatúru a publikácie uvedené v priloženom zozname.

Nemám závažný dôvod proti použitiu tohoto školského diela v zmysle §60 Zákona č.121/1200Sb., o autorskom práve, o právach súvisiacich s autorským právom a o zmene niektorých zákonov (autorský zákon).

V Prahe dňa

Acknowledgements

I would like to give thanks to my supervisor, Mgr. Jaroslav Bielčík Ph.D., for his support and interest in my work, to my consultant Ing. Olga Rusňáková for her willingness to help, to Dr. Barbara Trzeciak for her bright advices and comments and finally to Dr. Mustafa Mustafa for his patience and unvaluable help and discussions. Of course I would like to also thank to my parents, grandmother, sister Zuzana Gajdošová and boyfriend Bc. Filip Křížek, for their support during my work.

Názov práce: **Produkcia nefotonických elektrónov v zrážkach U+U s energiou 193 GeV v experimente STAR**

Autor: Katarína Gajdošová

Odbor: Jadrové inžinierstvo

Druh práce: Diplomová práca

Vedúci práce: Mgr. Jaroslav Bielčík, Ph.D.
Katedra fyziky, Fakulta jaderná a fyzikálne inženýrská,
České vysoké učení technické v Praze.

Abstrakt:

Vlastnosti silnej interakcie spôsobujú uväznenie kvarkov v hadrónoch. V podmienkach vysokej hustoty a teploty je možné vytvoriť stav hmoty kde sa kvarky a gluóny chovajú ako by boli takmer voľné. STAR experiment, ktorý je umiestnený na Relativistickom urýchľovači ťažkých jadier, sa hlavne zaoberá štúdiom tohto horúceho a hustého média. Tento stav hmoty nie je možné pozorovať priamo a študujú sa len konečné spektrá vyletujúcich častíc. Elektróny pochádzajúce zo semileptonických rozpadov otvorených ťažkých mezónov sú dobrou sondou pre merania ťažkých kvarkov, ako napríklad c a b . Tieto kvarky sa vytvárajú počas počiatočných fáz jadro-jadrových zrážok. Preto sú merania ťažkých vóní dôležité pre štúdium procesov straty energie v QGP. V tejto práci je prezentované meranie spektier nefotonických elektrónov v uránových zrážkach v rozsahu priechnej hybnosti $p_T = 1.2 - 6.0$ GeV/ c .

Kľúčové slová: kvark-gluónová plazma, STAR, nefotonické elektróny

Title: **Production of non-photonic electrons in U+U collisions at 193 GeV in STAR experiment**

Author: Katarína Gajdošová

Abstract:

Properties of strong interaction cause that quarks are confined into hadrons. Under the conditions of high density and temperature it is possible to create a state of matter where quarks and gluons act as if they were free. The STAR experiment at the Relativistic Heavy-Ion Collider is dedicated to the study of this hot and dense hadronic matter. This state of matter cannot be observed directly and only final particle spectra are studied. The electrons originating from semileptonic decays of open heavy flavor mesons are a good proxy for heavy flavor quarks, such as c and b . These quarks are created during the early stages of a heavy-ion collision. Therefore, heavy flavor measurements are important for the study of energy loss processes in QGP. In this work the measurement of non-photonic electron spectra in uranium collisions is presented in a transverse momentum range of $p_T = 1.2 - 6.0$ GeV/ c .

Keywords: quark-gluon plasma, STAR, non-photonic electrons

Contents

Introduction	17
1 Heavy flavor physics in heavy-ion collisions	19
1.1 Quark-gluon plasma	20
1.1.1 Phase diagram of hadronic matter	20
1.1.2 Space-time evolution of a heavy-ion collision	21
1.2 Centrality of a heavy-ion collision	23
1.3 Nuclear modification factor	24
1.4 Jet quenching	26
1.4.1 Dead-cone effect	28
1.5 Elliptic flow	28
1.6 Collisions of deformed nuclei	30
1.7 Heavy flavor measurements	32
1.7.1 Quarkonia	32
1.7.2 Open heavy flavor	34
1.8 Measurements of non-photonic electrons	36
1.8.1 Measurements in p+p collisions	36
1.8.2 D and B meson contribution to NPE yield	37
1.8.3 Measurements in heavy-ion collisions	38
1.8.4 Measurements at lower beam energies	41
1.9 STAR measurements in uranium collisions	43
1.10 Future STAR plans	45
2 The STAR Experiment	47
2.1 Time Projection Chamber	48
2.1.1 How does TPC work	49
2.2 Time of Flight	50
2.3 Barrel Electromagnetic Calorimeter	51
2.4 Vertex Position Detector	51
2.5 Heavy Flavor Tracker	51
2.6 Muon Telescope Detector	53
3 Analysis of non-photonic electrons	55
3.1 Event and track quality cuts	56
3.2 Electron identification cuts	57
3.3 Determination of photonic background	59
3.4 Summary of selection criteria applied in NPE analysis	61

4	Reconstruction efficiencies and detector acceptance	63
4.1	Efficiency of $n\sigma_e$ cut of single electron tracks	63
4.2	Efficiency of single electron cuts using BEMC	64
4.3	Purity	65
4.4	Photonic electron reconstruction efficiency	69
4.5	Single track reconstruction efficiency	70
5	Non-photonic electrons	73
5.1	Systematic uncertainties	73
5.2	Nuclear modification factor	75
5.3	Statement about the author contribution	80
6	Discussion of results	81
	Conclusions	83
	Appendices	89
A	QA of EMC cuts	91
B	Checking the purity of PHE	95
C	Efficiency studies	97
D	List of public presentations and posters	105
	Extended abstract on Student scientific conference in Ostrava	107
	Poster on 53 rd International Winter Meeting in Nuclear Physics	113
	Proceedings on 53 rd International Winter Meeting on Nuclear Physics	115

List of Figures

1.1	Diagram of phase transition diagram between QGP and hadron gas.	21
1.2	A space-time diagram of a heavy-ion collision.	22
1.3	Illustration of centrality of a collision.	23
1.4	Multiplicity distribution with assigned bins of centrality.	24
1.5	Nuclear modification factor of charged hadrons.	25
1.6	A scheme of a pp and AA collision.	27
1.7	Azimuthal di-hadron correlations in STAR.	27
1.8	R_{AA} of different particles in ALICE experiment.	29
1.9	Transverse view of the overlap zone of a peripheral collision.	29
1.10	Measurements of elliptic flow at STAR.	30
1.11	Types of uranium collisions and energy density in U+U relative to Au+Au collisions.	31
1.12	Different configurations of a central U+U collision.	31
1.13	R_{AA} of Υ against centrality.	33
1.14	R_{AA} of J/ψ in Au+Au and Cu+Au collisions.	34
1.15	R_{AA} of NPE at different collisions measured by PHENIX.	34
1.16	R_{AA} of D mesons in Au+Au collisions at $\sqrt{s_{NN}} = 200$ GeV.	35
1.17	Invariant yield of NPE in p+p collisions at $\sqrt{s_{NN}} = 200$ GeV.	37
1.18	Azimuthal distribution of e-h paris.	38
1.19	Relative B meson contribution to the NPE yield.	38
1.20	R_{AA} of NPE in Au+Au collisions at $\sqrt{s_{NN}} = 200$ GeV from Year 2003.	39
1.21	R_{AA} of NPE in Cu+Cu and Au+Au collisions measured by PHENIX.	39
1.22	Nuclear modification factor of NPE in central Au+Au collisions at STAR.	40
1.23	Measurements of NPE v_2 compard to models.	40
1.24	R_{AA} of NPE from beauty decays in central Pb+Pb collisions.	41
1.25	Nuclear modification factor of NPE in Au+Au collisions at lower beam energies at STAR and PHENIX.	42
1.26	Elliptic flow measurements in Au+Au collisions at $\sqrt{s_{NN}} = 39, 62.4$ and 200 GeV.	42
1.27	R_{AA} of D mesons in U+U collisions at $\sqrt{s_{NN}} = 193$ GeV.	43
1.28	R_{AA} of D^0 mesons in U+U and Au+Au collisions versus centrality.	44
1.29	Quarkonia suppression in U+U and Au+Au collisions.	44
2.1	Relativistic Heavy Ion Collider RHIC.	47
2.2	Picture of the STAR detector.	48
2.3	Energy loss as function of momentum.	49
2.4	Time projection chamber.	49
2.5	Particle identification from TOF.	50
2.6	Picture of one module of BEMC.	52
2.7	Scheme of Heavy Flavor Tracker.	53

2.8	Reconstruction of D^0 meson signal with included HFT.	54
2.9	J/ψ signal as it would look like with MTD.	54
3.1	Distribution of event vertices.	56
3.2	$n\sigma_e$ of inclusive electrons as a function of p_T	58
3.3	Distribution of the ratio p/E_0	58
3.4	Distributions of difference between projected SMD and acutally fired SMD.	59
3.5	Distribution of invariant mass.	60
3.6	Distribution of $n\sigma_e$ of the global partner track.	60
3.7	Raw p_T spectrum of inclusive and photonic electron sample.	62
4.1	Distributions of $n\sigma_e$ of the primary electron track from photonic electron pairs.	63
4.2	$n\sigma_e$ efficiency.	64
4.3	Distribution of $n\sigma_e$ of global electron tracks from the photonic pairs.	65
4.4	Distribution of EMC efficiency.	65
4.5	Mean and width of the $n\sigma_e$ distribution.	66
4.6	The $n\sigma_e$ distribution of inclusive electrons.	67
4.7	Distributions of means and widths of 4-Gaussian fit.	67
4.8	The $n\sigma_e$ distributions of inclusive electrons.	68
4.9	The final purity distributions.	68
4.10	Distributions of photonic electron reconstruction efficiency.	69
4.11	The single track reconstruction efficiency.	70
5.1	Spectra of NPE and PHE.	74
5.2	Ratio NPE/PHE in U+U collisions compared to Au+Au collisions.	74
5.3	Invariant yield of NPE.	75
5.4	Confidence intervals of efficiencies which contribute to systematics.	76
5.5	Relative systematic uncertainty of the yield of NPE.	76
5.6	Spectra of NPE in p+p collisions.	78
5.7	Nuclear modification factor of NPE.	78
5.8	Relative statistical uncertainties of R_{AA}	79
5.9	Relative systematical uncertainties of R_{AA}	79
A.1	Distributions of p/E_0	91
A.2	Distributions of Δ_φ	92
A.3	Distributions of Δ_Z	93
B.1	Invariant mass distributions of electron pairs.	95
B.2	Distributions of $n\sigma_e$ of global partner tracks.	96
C.1	Distributions of $n\sigma_e$ of primary electron tracks.	97
C.2	Distributions of $n\sigma_e$ of global partner tracks without EMC cuts.	98
C.3	Distributions of $n\sigma_e$ of global partner tracks with EMC cuts.	99
C.4	Distributions of $n\sigma_e$ of inclusive electrons.	100
C.5	Distributions of $n\sigma_e$ of inclusive electrons at $1.2 < p_T < 1.4$ GeV/c.	101
C.6	Distributions of $n\sigma_e$ of inclusive electrons at $1.4 < p_T < 1.6$ GeV/c.	101
C.7	Distributions of $n\sigma_e$ of inclusive electrons at $1.6 < p_T < 1.8$ GeV/c.	102
C.8	Distributions of $n\sigma_e$ of inclusive electrons at $1.8 < p_T < 2.0$ GeV/c.	102
C.9	Distributions of $n\sigma_e$ of inclusive electrons at $2.0 < p_T < 3.0$ GeV/c.	103
C.10	Distributions of $n\sigma_e$ of inclusive electrons at $3.0 < p_T < 4.0$ GeV/c.	103

C.11 Distributions of $n\sigma_e$ of inclusive electrons at $4.0 < p_T < 5.0$ GeV/ c	104
C.12 Distributions of $n\sigma_e$ of inclusive electrons at $5.0 < p_T < 6.0$ GeV/ c	104

List of Tables

1.1	Basic properties of quarks.	19
1.2	Properties of quarkonia.	32
1.3	Properties of heavy mesons.	34
3.1	Summary of cuts applied in NPE analysis.	61
5.1	Contributions to systematic uncertainties.	77

Introduction

Quark-gluon plasma (QGP) is a state of matter where quarks and gluons, normally bound in hadrons, can move almost as free particles. This state can be created at very extreme conditions at high densities and temperatures as e.g. at the beginning of the Universe. Nowadays, we are able to create this form of matter in ultrarelativistic heavy-ion collisions at powerful colliders, such as the Relativistic Heavy Ion Collider at Brookhaven National Laboratory or the Large Hadron Collider at CERN.

This thesis is focused on the study of quark-gluon plasma with heavy flavor measurements. One of the most promising probes are the heavy quarks, c and b . These quarks are created before thermal equilibrium is established and QGP created, but they are affected by the strong interactions inside the medium and can lose energy. Study of open heavy flavor, hadrons containing one heavy quark, is one of the possibilities to investigate the behaviour of heavy quarks inside QGP and therefore, study its properties.

First chapter is dedicated to theoretical introduction of the physics of heavy-ion collisions, energy loss mechanisms of heavy quarks in QGP, experimental probes of these quarks and finally it presents recent results of these studies at RHIC and LHC.

The STAR experiment is one of the two main experiments at RHIC and it is designed for the study of strongly interacting medium. The Solenoidal Tracker at RHIC (STAR) consists of many subdetectors, such as the Time Projection Chamber which serves for tracking and particle identification (PID). The Time of Flight detector is able to measure velocities of particles what serves for better PID. Energy of particles can be measured by the Barrel Electromagnetic Calorimeter that also serves as a trigger detector. More detailed description of the STAR detector is provided in the second chapter.

In the rest of this thesis the analysis of non-photonic electrons (NPE) in uranium-uranium collisions at $\sqrt{s_{NN}} = 193$ GeV at the STAR experiment is presented. First, the selection of inclusive and photonic electron yield is described in chapter four. In the next chapter, the studies of detection efficiencies and detection acceptancies are shown. Finally, the spectra of NPE, their invariant yield as well as the nuclear modification factor are obtained and presented in chapter five, together with the estimation of systematical uncertainties.

Chapter six concludes this work with discussion of the obtained results.

Chapter 1

Heavy flavor physics in heavy-ion collisions

It is known for a couple of decades now that the fundamental blocks of matter are not protons, neutrons and electrons, but there are even smaller constituents of nucleons. The basic building blocks of matter are thus the so-called quarks and gluons and the strong interaction between them is described by a theory called Quantum Chromodynamics (QCD).

Currently 6 different flavors of quarks are known and they may be divided into 3 doublets as it is illustrated in 1.1.

$$\begin{pmatrix} u \\ d \end{pmatrix} \begin{pmatrix} c \\ s \end{pmatrix} \begin{pmatrix} t \\ b \end{pmatrix} \quad (1.1)$$

Basic properties of quarks are summarized in the Tab. 1.1. They are distinguished according their flavor, and each of them can carry one of three colors: red, green, blue. Additionally, each quark has also antiquark which carries an anticolor.

flavor	m [MeV/c ²]	Q[e]	S	C	B	T
u	2.3	$\frac{2}{3}$	0	0	0	0
d	4.8	$-\frac{1}{3}$	0	0	0	0
c	1275.0	$\frac{2}{3}$	0	1	0	0
s	95.0	$-\frac{1}{3}$	-1	0	0	0
t	173210.0	$\frac{2}{3}$	0	0	0	1
b	4180.0	$-\frac{1}{3}$	0	0	-1	0

Table 1.1: Basic properties of quarks. Taken from Ref. [1].

The up, down and strange quark are commonly labeled as light flavor quarks. The other three quarks, charm, bottom and top, are called heavy flavor quarks due to its large mass. Quark charge is a fraction of elementary charge, namely they have $Q = 2/3$ or $Q = -1/3$. Also, each quark flavor has a conserving quantum number. These are: strangeness S , charm C , beauty B and truth T . Only strange quarks have non-zero strangeness as well as only charm quarks has non-zero charm, bottom quarks beauty and top quarks truth.

The strong interaction between quarks is mediated via gauge bosons, gluons. They can be imagined as particles that are at the time of interaction exchanged by quarks. Gluons carry two colors so they are able to change the color of quark they are interacting with. According to QCD there are 8 different gluons.

At normal conditions the quarks are always bounded inside a hadron. They have never been seen as single particles. All hadrons are formed of quarks in a way that the resulting hadron must be colorless. The colors can be combined in analogy to the light that is, red with green and blue gives a colorless particle state. Also, when a color is combined with its anticolor, the result will be colorless. Particles denoted as mesons are formed of one quark and an antiquark and those formed of three quarks or three antiquarks are called baryons.

The strong potential, on the contrary to the electromagnetic, is increasing linearly with distance. This means, that it is not possible to separate two quarks which are bounded. At some point the energy increases such that a new quark-antiquark pair is created, so in the end two quark pairs exist. On the other hand, with decreasing distance (or with increasing energy) the strong force is decreasing and asymptotically approaches zero. Therefore, the quarks can be treated as almost free non-interacting particles. This phenomenon is called the asymptotic freedom.

1.1 Quark-gluon plasma

The main purpose of the STAR experiment is to investigate a hot and dense medium called the quark-gluon plasma (QGP) and spin structure of proton (however, this will not be discussed in this work). Fundamental building blocks of nature, quarks and gluons, are in deconfined state in this medium and can be taken as almost free particles. In order to achieve satisfactory conditions to establish QGP, high energy densities and temperatures are needed. Bjorken first estimated the energy density as $\epsilon \approx 1 - 10 \text{ GeV}/\text{fm}^3$ which should be sufficient for the establishment of local thermal equilibrium and adjacent creation of deconfined state of quarks and gluons [2]. By observation of direct photons the initial temperature of the system can be estimated. PHENIX experiment performed the measurements and calculated the initial temperature as $T_{init} \approx 221 \text{ MeV}$ while estimations from hydrodynamical models resulted in much higher initial temperatures $T_{init} \approx 300 - 600 \text{ MeV}$ [3]. In both cases these high temperatures and energy densities are high enough to create the quark-gluon plasma. In fact, the initial temperatures exceed the temperature of phase transition from hadron gas to QGP calculated by lattice QCD $T_c \approx 170 \text{ MeV}$ [4]. The complete description of the QGP is still not known. Perturbative quantum chromodynamics works well for matter created in proton-proton collisions, where no QGP is created, but it fails at description of the medium created in heavy-ion collisions due to present non-perturbative effects.

Nowadays, the quark-gluon plasma can be created in heavy-ion collisions at ultrarelativistic energies. Such collisions take place in synchrotron accelerators, where beams of heavy ions, such as nuclei of gold or lead, circulate in two independent beam pipes in opposite directions, and at the intersection point where a detector is located the heavy ions collide. These particles are accelerated to almost the speed of light, so as a consequence of Lorentz contraction along the direction of their movement they squeeze. At the moment of a collision, these pancakes pass through each other and as they are drawing apart, a “fire-ball” is created with sufficient conditions for the formation of QGP. The created system is expanding during first fm/c after the collision mainly in longitudinal direction because nuclei are receding with almost the speed of light.

1.1.1 Phase diagram of hadronic matter

Time scale of duration of a heavy-ion collision is about 10 fm/c [5]. The QGP is created at the beginning after thermalization of the system and it cools and expands rapidly until

the phase transition to hadronic gas occurs. The transition between quark-gluon plasma and hadron gas is still object of intense research. In Fig. 1.1 the phase transition diagram is shown in terms of temperature of the system T and baryo-chemical potential μ_b . The latter variable can be defined as the relative abundance of baryons over antibaryons. When $\mu_b = 0$, the matter and antimatter is equally present in the collision. On the other hand, when $\mu_b > 0$, there is more matter than antimatter in the collision. The definition can also be said in other words e.g., the baryo-chemical potential is the amount of energy that is needed to add a baryon into the system.

The quark-gluon plasma phase exists above the transition line where the temperatures or baryo-chemical potentials are high. The transition line represents the first order phase transition where the evolution of state variables, such as entropy, suffer from a discontinuity. For low baryo-chemical potentials and high temperatures the so called rapid cross-over takes place, which can be described as gentle transition between the two phases.

Modern accelerating facilities as LHC in CERN or RHIC in BNL can reach points of this diagram that lie at the cross-over region or even higher. For low μ_b the critical temperature of phase transition is estimated to be $T_{crit} \approx 170$ MeV [4]. The STAR experiment hosts a research program called the Beam Energy Scan (BES). Its purpose is to further investigate the transition region of the phase diagram of hadronic matter. Hints of quark-gluon plasma are studied in Au+Au collisions at different beam energies varying from $\sqrt{s_{NN}} = 7.7 - 62.4$ GeV [6].

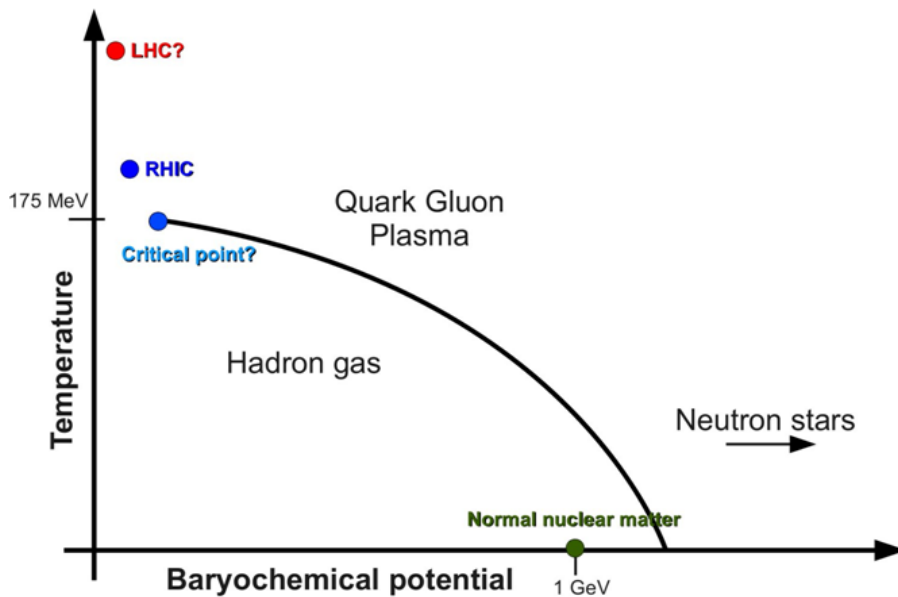


Figure 1.1: A phase diagram showing the phase transition between quark-gluon plasma and hadron gas. For low μ_b and temperature ~ 170 MeV a cross-over takes place, from critical point towards higher μ_b there is a first order phase transition. Taken from Ref. [7].

1.1.2 Space-time evolution of a heavy-ion collision

At a collision of heavy ions at sufficient center of mass energy after some formation time a new state of matter called quark-gluon plasma can be created. It is possible to divide the evolution of the created system into various stages. The diagram in Fig. 1.2 illustrates different moments of a heavy-ion collision which are described below. As was mentioned before, right after the collision the created system is expanding mainly in longitudinal

direction that allows us to describe the space-time evolution of the collision in terms of time t and direction of the incoming beam of particles z . The proper time τ is situated on hyperbolas of the diagram.

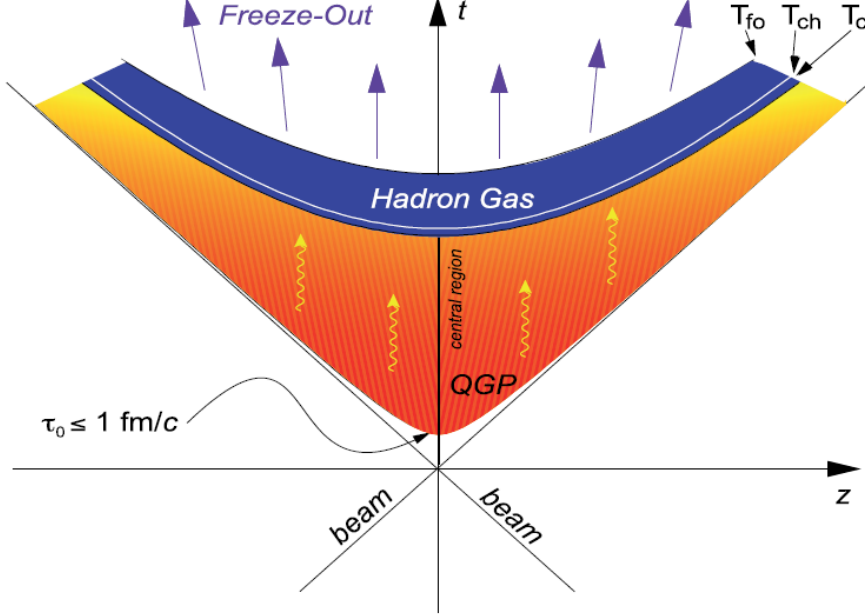


Figure 1.2: A space-time diagram of different stages of a heavy-ion collision. At proper time τ_0 the system comes to thermal equilibrium and QGP is created. At critical temperature T_c the phase transition to hadron gas takes place. T_{ch} is the temperature of chemical freeze-out and T_{fo} temperature of kinetic freeze-out. Taken from Ref. [8].

The evolution of the system after the collision can be divided into the following stages [5]:

- Right after the collision of nuclei the system is composed of excited virtual quanta and it will take time to deexcite and form quarks and gluons. Heavy quarks can be created in hard scatterings with large transferred momentum. The system is in the pre-equilibrium phase.
- After the formation time $\tau_0 \approx 1 \text{ fm}/c$ thermal equilibrium is established and the system is in a state of matter called quark-gluon plasma. This stage of the collision can be sufficiently described by hydrodynamics as plasma is almost an ideal fluid.
- At critical temperature $T_c \approx 170 \text{ MeV}$ the system undergoes a phase transition from QGP to hadron phase: quarks and gluons are no longer free but confined by the strong force into hadrons.
- At higher baryo-chemical potential one can distinguish between two types of freeze-outs. At $\tau_{ch} < \tau_{fo}$ there is a chemical freeze-out after which particles no longer suffer inelastic scatterings, but they can still lose their energy by elastic collisions with other particles of the system. The ratio of different particle species remains constant. At τ_{fo} the kinematic freeze-out takes place. At this point elastic collisions cease, particles do not lose their energy in scatterings with other particles and fly away into the vacuum. For low values of baryo-chemical potential these two freeze-outs occur at the same proper time.

Unfortunately, the detection systems are not able to record the short time in which all the above described steps occur (order of $\approx 10 \text{ fm}/c$). Only the final particle states can be detected and therefore, what actually happens at the time of a collision can be only estimated.

1.2 Centrality of a heavy-ion collision

Particle accelerators can collide heavy ions with different size and shape, for example gold, lead or uranium. Both have very big atomic numbers thus, if they collide, many nucleon-nucleon collisions occur. Due to finite size of colliding nuclei it is not possible to collide every time with the same configuration. The overlap region can of course vary from almost none to totally overlapped nuclei. In case the overlap region is small, less nucleons participate in collision while all nucleons collide in case of fully overlapped nuclei. At each configuration different energy densities or temperatures are present and this can affect the formation of QGP. The less nucleons participate the collision, the less energy density is achieved and the less probability is to create quark-gluon plasma. In order to distinguish between different types of heavy-ion collisions, the concept of centrality of a collision is applied.

Centrality of a collision is defined with the impact parameter b that is the distance between centers of colliding nuclei. When $b = 0$ the collision is central, for $0 < b < 2R$ we call the collisions peripheral, and for $b > 2R$ ultraperipheral. In Fig. 1.3 there is an illustration of different types of centralities of a heavy-ion collision.

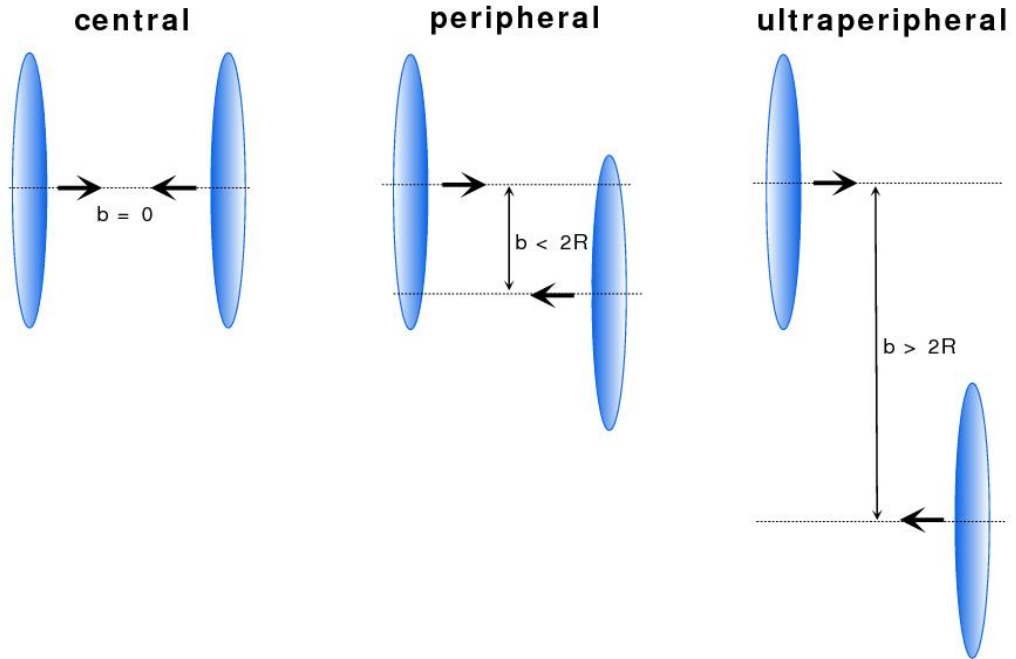


Figure 1.3: Illustration of different types of centralities of a collision of heavy nuclei. From left to right: central, peripheral and ultraperipheral collision.

Unfortunately, the impact parameter b is not possible to measure. One way in which one can define the centrality is through the Glauber model. This model assumes a nucleus-nucleus collision as a multiple nucleon-nucleon collisions. The nucleon-nucleon collision is characterized by total inelastic cross section σ_{ine} [9].

Estimation of the centrality of a collision can be made through the measurements of multiplicity of a collision, which is the number of particles produced in one collision. The more central is the collision, the more particles can be created. Therefore, the multiplicity distribution can be helpful in the determination of the centrality of a collision. In Fig. 1.4 the charged particle multiplicity distribution can be seen. As was said above, the most central collisions are those with highest particle multiplicity and viceversa. Also, logically, the most central collisions will not have such high cross section. This distribution is cut into various centrality bins according to the particle multiplicity, which was correlated with the Glauber model through the number of participants N_{part} and the impact parameter b . As can be noticed, the highest centrality also corresponds to the highest N_{part} as was already mentioned above, and the impact parameter b is equal to 0 at highest centrality.

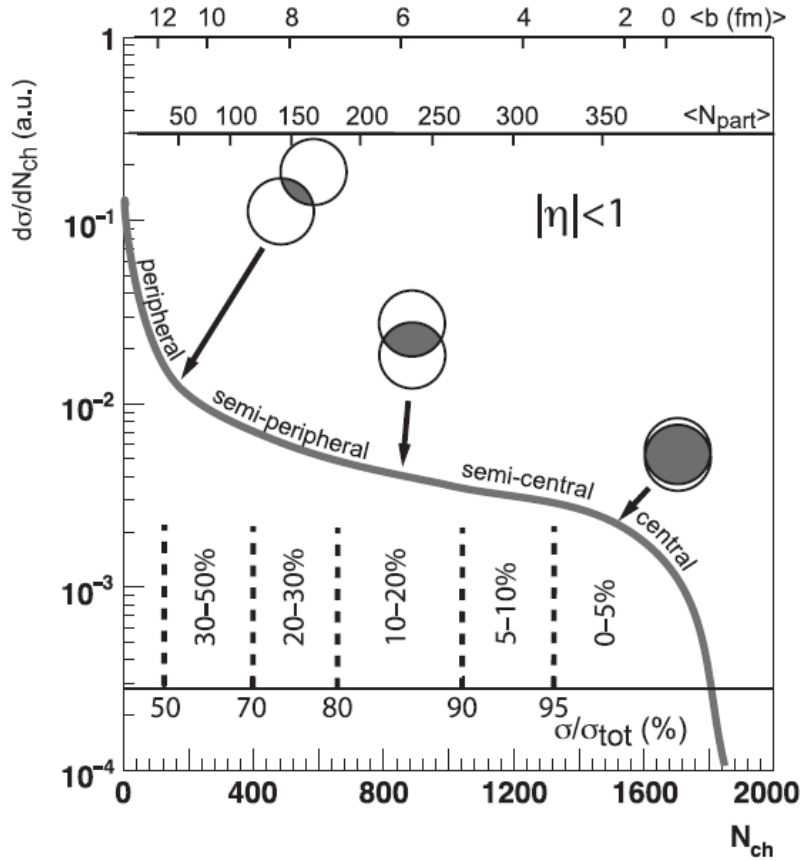


Figure 1.4: Charged particle multiplicity distribution divided into various bins of centrality which are also assigned through Glauber model to impact parameter b and number of particles that participated in collision N_{part} . Taken from Ref. [10].

1.3 Nuclear modification factor

Quark-gluon plasma cannot be observed directly due to its very short time of existence. Therefore, final particle spectra are studied as an indirect measurement of the new form of matter. For this purpose, one has to compare the measurements from heavy-ion collisions to a system where no QGP is created. Such a system is for instance a proton-proton collision. In case a strong interacting medium is created in collisions of heavy nuclei, there will be a difference in the final particle spectra in comparison to p+p collisions due to interactions of quarks and gluons in quark-gluon plasma.

An observable suitable for studying the effects of QGP on particle production is nuclear modification factor R_{AA} defined as a ratio of particle production in heavy-ion collisions to proton-proton collisions. In order to get relevant information, the particle productions have to be compared always at the same conditions which are the energy, centrality, transverse momentum p_T and rapidity y . The ratio is scaled by the mean number of binary collisions (nucleon-nucleon) in one heavy-ion collision $\langle N_{bin} \rangle$.

$$R_{AA} = \frac{1}{\langle N_{bin} \rangle} \frac{d^2 N_{AA}/dydp_T}{d^2 N_{pp}/dydp_T} \quad (1.2)$$

Quarks and gluons are expected to suffer an energy loss in QGP by interactions with the strongly interacting medium compared to p+p collisions where no such medium is present. Therefore, particles coming from p+p collisions observed with high p_T will not be detected at the same p_T bin when originate in heavy-ion collisions. Thus, by comparing the particle production from heavy-ion collisions to proton-proton collisions at high p_T , less particle production should be seen. Also, some particles that would have been formed are decomposed due to color screening of di-quark potential and then cannot be observed which causes a suppression of particle production too. More about this phenomena will be discussed below.

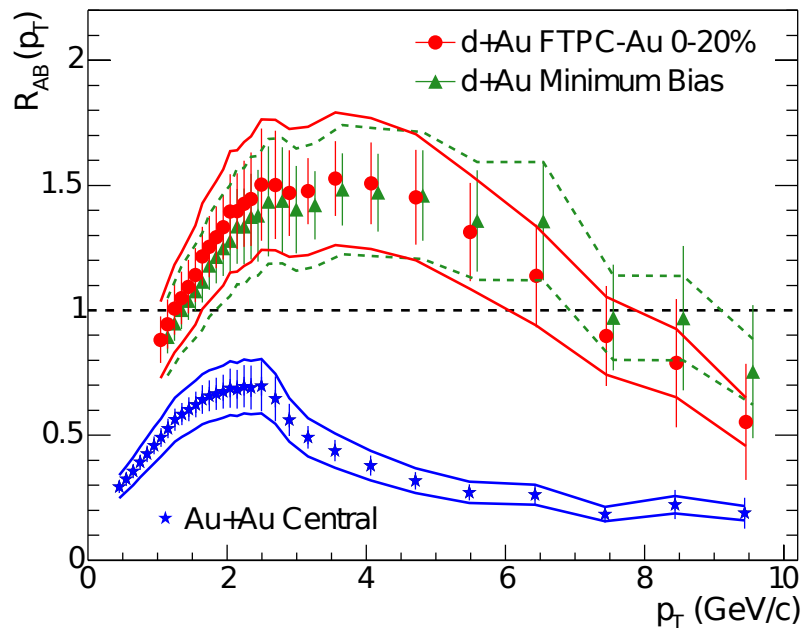


Figure 1.5: Nuclear modification factor of charged hadrons in d+Au and Au+Au collisions at the STAR experiment at $\sqrt{s_{NN}} = 200$ GeV. In d+Au collisions a Cronin effect can be seen and in heavy-ion collisions a suppression is observed. Taken from Ref. [11].

If the R_{AA} is equal to one, that means no QGP effects are observed and heavy ion collisions are just a superposition of numerous nucleon-nucleon (proton-proton) collisions. If $R_{AA} > 1$, it is called an enhancement which can be caused by Cold Nuclear Matter effects, such as Cronin effect. These effects can be studied for example in deuteron-gold collisions, where no QGP is formed, but multiple scatterings are present which leads to higher number of particles with low momentum than in p+p collisions. Finally, if $R_{AA} < 1$, it is commonly denoted as a suppression. Particles lose energy or they are melted in QGP, so the final production is smaller than the production from p+p collisions. This situation

is illustrated in Fig. 1.5. In d+Au collisions a Cronin effect is observed and in central Au+Au collisions a strong suppression is present at $p_T \geq 3$ GeV/ c .

If no reference data from p+p collisions are provided, other form of nuclear modification factor can be studied, namely the R_{CP} . It is defined as ratio of particle production in central heavy-ion collisions with respect to peripheral heavy-ion collisions. As it was said above, in central collisions the energy density is higher and also partons must pass longer distance through the created QGP therefore, a suppression may be observed. The bigger the centrality is in the numerator and smaller in the denominator, the bigger may be the magnitude of suppression. The fraction is again scaled by mean number of binary collisions in one central/peripheral heavy-ion collision. The b_1 and b_2 represent impact parameters at central and peripheral collisions, respectively.

$$R_{CP} = \frac{\langle N_{bin} \rangle(b_2) d^2 N_{AA}(b_1)/dydp_T}{\langle N_{bin} \rangle(b_1) d^2 N_{AA}(b_2)/dydp_T} \quad (1.3)$$

1.4 Jet quenching

As was mentioned before, the quark-gluon plasma cannot be observed directly. The study of appropriate probes that can reveal information about interaction of particles with strong matter becomes important. One of these useful probes is the study of jet properties which is a consequence of the phenomenon called jet quenching.

Two energetic partons are created in hard processes with large transferred momentum. In case they are created close to the surface of the fireball, one of them flies out of this medium and the second one goes in the opposite direction through the strongly interacting medium. As the parton passes through QGP, it can lose energy by interactions with this medium. Experimentally a jet of particles created from fragmentation of the parton are observed. A scheme of this process can be seen in the Fig. 1.6. On the left side of the figure there is a proton-proton collision, where no QGP is created. As two quarks collide in a hard process, two partons originate in opposite directions forming a jet of particles. There is no medium that could cause strong interactions, so there are two fully evolved jets in both directions. On the right side of the figure there is a nucleus-nucleus collision where a QGP is formed. In hard process two partons are created near the surface of the fireball. One parton propagates through the medium and the resulting jet is quenched, while the second jet is almost unquenched.

The above mentioned phenomenon can be clearly seen when one studies azimuthal distribution of hadrons with high p_T in heavy-ion collisions. It should be seen that associated opposite jets are quenched after passing through QGP. An example of this distribution is shown in the Fig. 1.7. A hadron (trigger particle) with transverse momentum $p_T \geq 4$ GeV/ c is selected in azimuth angle φ_{trigg} and the distribution of hadrons with $p_T \geq 2$ GeV/ c is studied dependent on $\Delta\varphi = \varphi - \varphi_{trigg}$. The azimuthal correlation around angle φ_{trigg} is defined as “near-side” and the opposite domain around $\Delta\varphi \approx \pi$, where in case of no QGP formed the associated opposite jet can be found, as “away-side”. In the Fig. 1.7 a clear signal of opposite jet is visible in p+p and d+Au collisions, while in Au+Au collisions the opposite jet totally disappears. We interpret this as a consequence of energy loss of opposite parton passing through strongly interacting medium [11].

As a consequence of jet quenching a suppression of production of particles with high transverse momentum ($p_T \gtrsim 2$ GeV/ c) is observed. These particles were created mainly during hard processes with large transferred momentum during the early stages of a collision. There is also the so-called soft production which consists of particles created inside the hot medium and thus their resulting momenta are smaller. In this work we are going

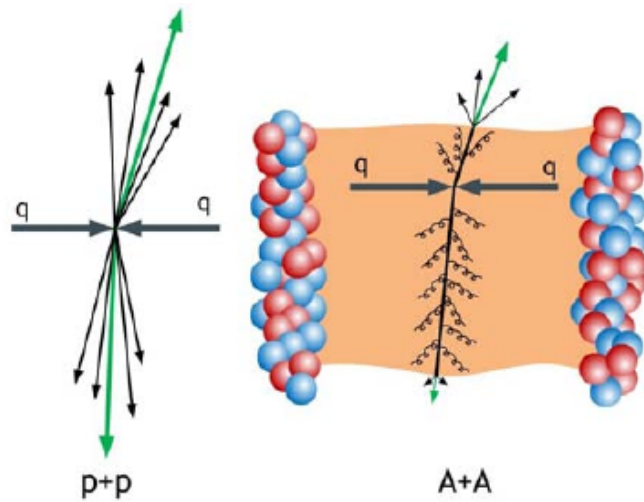


Figure 1.6: Jet quenching - a scheme of a pp and AA collision. In pp collisions there is no QGP, outgoing particles are not quenched by the interaction with QGP. In AA collisions a strongly interacting medium is created and as a consequence the production of particles with high p_T is suppressed. Taken from Ref. [12].

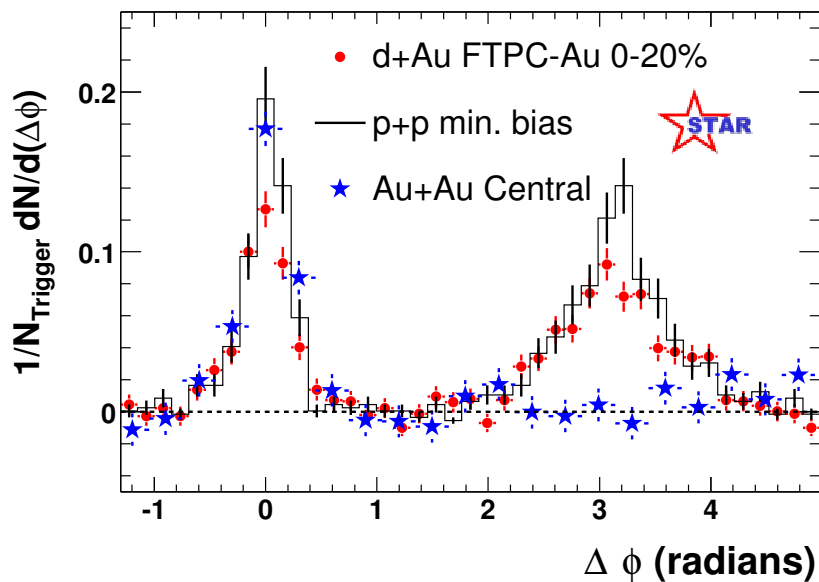


Figure 1.7: Azimuthal di-hadron correlations from di-jet production at STAR at the energy $\sqrt{s_{NN}} = 200$ GeV. Trigger particle with $p_T \geq 4$ GeV/c is at angle $\Phi = 0$, “away-side” signal measured for particles with $p_T \geq 2$ GeV/c is at angle $\Delta\Phi = \pi$. Taken from Ref. [11].

to focus only on hard production. High-energetic partons lose their energy via interactions with the QGP before they can hadronize, so they lose part of their transverse momentum. Particles formed of these partons will also have smaller values of p_T . Thus, they no more belong to a group of particles with high transverse momenta, which leads to suppression of these particles in comparison with system where no QGP is present. This behaviour should be seen in terms of nuclear modification factor R_{AA} . It is defined according the formula 1.2 as ratio of particle production in heavy-ion collisions to p+p collisions. Thus, when studying the production of particles with high p_T , this ratio should be below 1, what is called suppression.

Particles which do not interact via the strong force do not feel the influence of quark-gluon plasma. If such a particle is created at the time of a collision of two nuclei, it will survive the passage through the strongly interacting medium with very high probability and finally will be detected. These particles are of strong interest due to their capability of carrying information about initial conditions present at heavy-ion collision even before or at the time of creation of QGP. The nuclear modification factor of particles that interact only via electromagnetic or weak force, such as γ , W^\pm and Z^0 , should therefore be equal to 1.

1.4.1 Dead-cone effect

There are mainly two types of energy loss of quarks in QGP: collisional and radiative. The gluon bremsstrahlung dominates in radiative losses. The so called dead-cone effect is expected and it means that for heavy quarks the amount of gluon radiation is smaller than that of light quarks [13].

The radiation of gluons is suppressed at angles smaller than the ratio of particle's mass and energy $\theta < m/E$. Thus, the bigger the quark mass is, the larger is the angle where the gluon radiation is suppressed resulting in smaller energy loss of a heavy quark.

If the dead-cone effect is in fact true and dominant in energy loss effects of quarks in QGP, it should be visible also as different magnitude of suppression of different quarks. Namely, the suppression of particles formed of light quarks should be the highest, while on the other hand the suppression of open heavy flavor mesons should be smaller $R_{AA}^{u,d,s} < R_{AA}^c < R_{AA}^b$. However, this pattern is not seen when we measure final hadrons because it is smeared by other effects. Recent results of the ALICE experiment in Pb+Pb collisions at $\sqrt{s_{NN}} = 2.76$ TeV confirm this: no significant difference in the behaviour of nuclear modification factors of different particles (Fig. 1.8) is observed. Only at small range of transverse momenta $2 < p_T < 6$ GeV/ c there is a hint of decreasing nuclear modification factor with decreasing quark mass [14].

1.5 Elliptic flow

Another observable called the elliptic flow can be studied in peripheral collisions in order to know more about the properties of QGP. The geometric asymmetry of the overlap zone in non-central collisions is later transformed into the anisotropy of distributions of final particle momenta caused by interactions between particles. The so-called almond shape of the reaction zone has non-zero excentricity as is shown in Fig. 1.9. In this picture the minor axis lies in the reaction plane which is defined by the beam axis and the impact parameter b . The pressure gradients at the reaction zone are higher in the direction of minor axis which eventually leads to non-zero elliptic flow.

The elliptic flow v_2 is defined as the second coefficient of Fourier expansion of particle

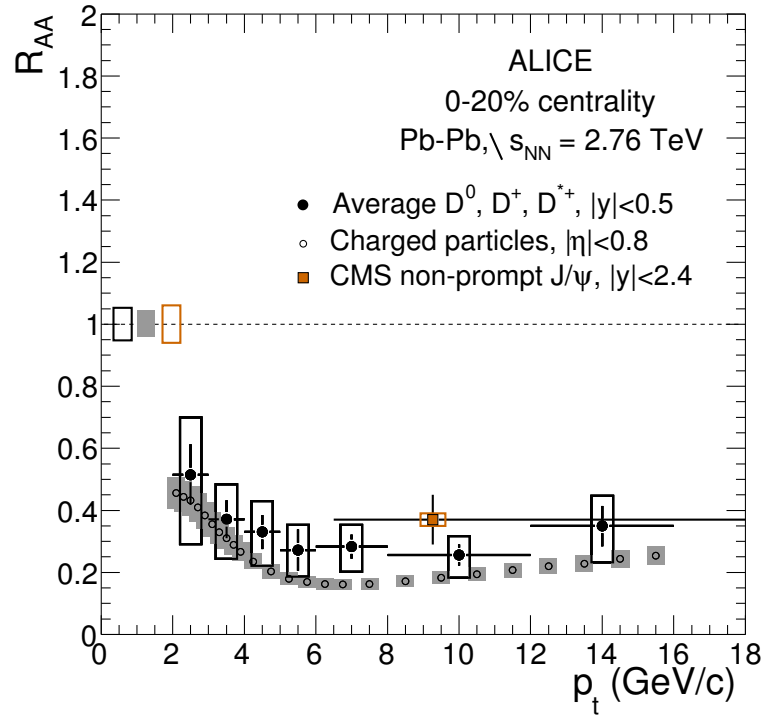


Figure 1.8: Nuclear modification factor of charged particles composed of light quarks, D mesons and B mesons measured at ALICE in central Pb+Pb collisions at $\sqrt{s_{NN}} = 2.76$ TeV [14].

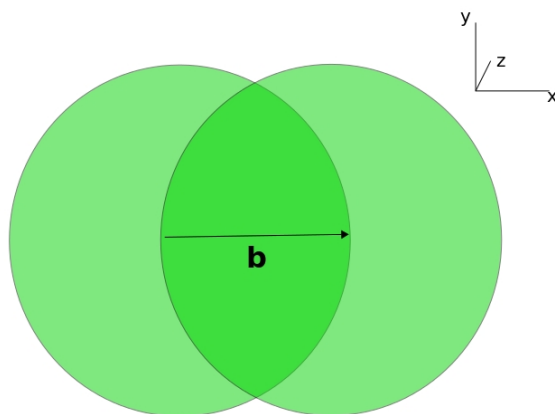


Figure 1.9: Transverse view of the overlap zone of a peripheral collision. The impact parameter b connects the centers of the nuclei.

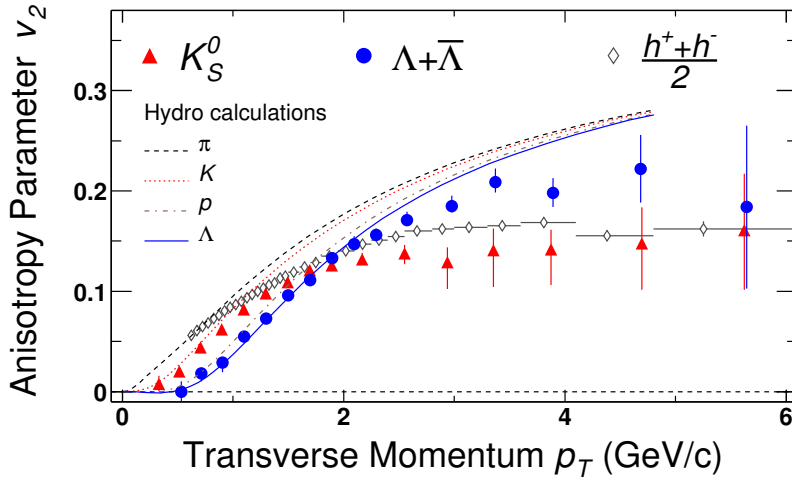


Figure 1.10: Measurements of elliptic flow of different identified particle species at STAR compared to hydrodynamical models. Taken from Ref. [16].

production in terms of the azimuthal angle φ with respect to the reaction plane:

$$\frac{dN_i(b)}{p_T dp_T dy d\varphi} = \frac{1}{2\pi} \frac{dN_i(b)}{p_T dp_T dy} [1 + 2v_1^i(p_T, b) \cos\varphi + 2v_2^i(p_T, b) \cos(2\varphi) + \dots]. \quad (1.4)$$

Measurements of elliptic flow performed at STAR show (Fig. 1.10) that the elliptic flow is non-zero which is an indication of particle interactions and fast thermalization of the system after the collision [15]. Also, the number-of-constituent-quark scaling indicates that the momentum anisotropy sets in early stages of the collision where the system is composed of partons what can be seen, for instance, in [16]. There is a difference between baryon and meson v_2 which after the scaling vanishes.

1.6 Collisions of deformed nuclei

The particle accelerators usually collide heavy nuclei which are symmetric, such as nuclei of gold on RHIC or lead nuclei on LHC. As was mentioned above, high energy densities present at these types of collisions are needed in order to create a hot and dense medium called quark-gluon plasma. In Year 2012 RHIC collided nuclei of uranium, which are significantly deformed in comparison to gold or lead nuclei and can reveal new interesting facts about QGP.

Due to prolonged shape of uranium nuclei the collisions can be classified not only according centrality, but also according the orientation of the nuclei with respect to each other which can of course affect the initial conditions at the collision point leading to the creation of QGP. Two basic types of an U+U collision are sketched in Fig. 1.11 (left). Collision where longer axes of nuclei are parallel to the beam axis are the so-called “tip-on-tip”. These collisions can provide higher energy densities and partons will have to pass larger length through the QGP. On the other hand, the “side-on-side” (or “body-on-body”) collisions where the short uranium axes are parallel to the beam axis, energy densities are similar to symmetric nuclei collisions and the path length is shorter. Also, the temperature in U+U collisions is expected to be higher [17].

In the Fig. 1.11 (right) relative energy density obtained in U+U to Au+Au collisions is plotted in different centrality bins. The nuclei are averaged over all possible orienta-

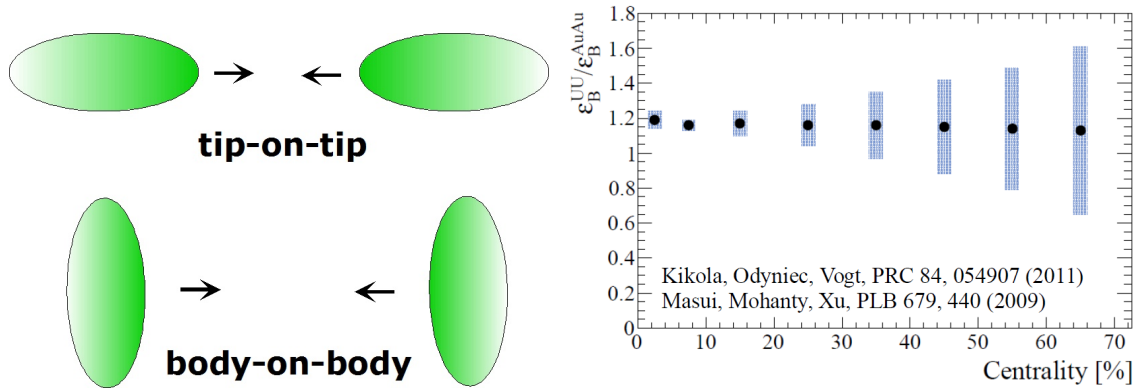


Figure 1.11: Left: Schematic of two basic types of an uranium collision: tip-on-tip and side-on-side (body-on-body). Right: Energy density in U+U versus Au+Au collisions achieved at different collision centralities. Taken from Ref. [17].

tions. It can be seen that the energy density is in general 20% higher in U+U than in Au+Au collisions [17]. Moreover, solely the tip-on-tip collisions can achieve up to 20-30% more energy density than the orientation-averaged collisions. The enhancement of energy density is most obvious in the most central uranium collisions [17].

According to the above discussed facts one would expect larger suppression of particle production in central uranium collisions. The effect could be even more visible from experimental data as in central collisions mostly tip-on-tip collisions happen. This is caused by the manner of how centrality of a collision is defined experimentally. The illustration in the Fig. 1.12 can be more explanatory. The so called Zero Degree Calorimeters located few meters away from the STAR detector around the beam pipe are designed to obtain the energy of particles which did not participate the heavy-ion collision. When a collision was peripheral, there is large energy deposit in ZDCs, while in a central collision there is almost no entry in ZDC calorimeters. In the Fig. 1.12 all three collisions of uranium nuclei are central. The first two configurations will be treated as central because there will be no energy deposition in ZDC. On the contrary, even if the third case is a central collision ($b = 0$), not all nucleons will participate the collision and thus it will not be classified by ZDC as central. As eventually the centrality bins are identified according the particle multiplicity, the first configuration will be “more central” as the second one, because following the Ref. [17] in tip-on-tip collisions there is higher particle multiplicity.

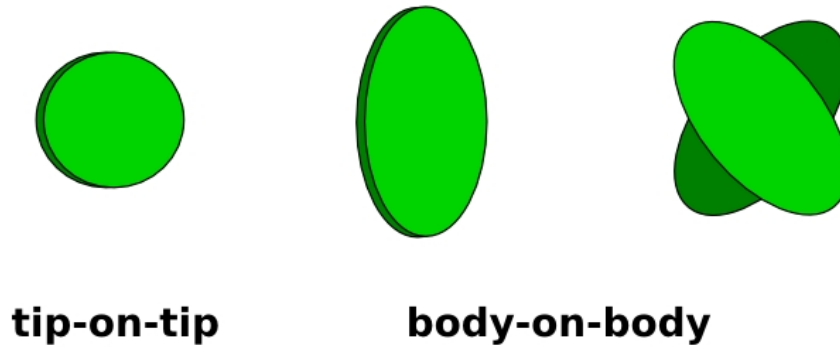


Figure 1.12: Various configurations of central uranium collisions. From left to right: tip-on-tip, side-on-side (all nucleons participate the collision), side-on-side (part of nucleons do not participate the collision).

1.7 Heavy flavor measurements

As was already mentioned at the beginning of this chapter, heavy quarks are created mainly in hard processes during first stages of a heavy-ion collision which makes them a good probe for the study of QGP. While the initial production of heavy quarks does not depend on the formation of QGP, the strongly interacting medium affects the production of particles composed of heavy quarks. Main effects studied in heavy flavor measurements are suppression of quarkonia and open heavy flavor at high p_T in comparison with suppression of light hadrons composed of light quarks. These measurements are described below in more detail in separate sections.

1.7.1 Quarkonia

Quarkonia are particles that consist of one heavy quark and antiquark with the same flavor. Particles composed of charm quarks are called charmonia, and hadrons composed of bottom quarks are bottomia. Quarkonia at their ground state are strongly coupled e.g., J/ψ for charmonia and $\Upsilon(1S)$ for bottomia. There are other less bounded states of quarkonia at higher states. In the Tab. 1.2 basic types of quarkonia are shown together with their quark content, mass and binding energy E_b .

quarkonium	content	mass [MeV/c ²]	E_b [GeV]
J/ψ	$c\bar{c}$	3096.92	0.64
χ_c	$c\bar{c}$	3510.66	0.22
ψ'	$c\bar{c}$	3686.11	0.05
$\Upsilon(1S)$	$b\bar{b}$	9460.30	1.10
$\Upsilon(2S)$	$b\bar{b}$	10023.26	0.53
$\Upsilon(3S)$	$b\bar{b}$	10355.20	0.20

Table 1.2: Properties of quarkonia: quark content, mass and binding energy E_b . Taken from Ref. [1], [18].

Because of the shape of the confining potential that is described by relation 1.5 where σ is the string tension and α is the gauge coupling, quarkonia with different confining potential have different radius r_c [19].

$$V(r) = \sigma r - \frac{\alpha}{r} \quad (1.5)$$

Quarkonia that are strongly confined have smaller radius and viceversa. This property is important as one is then able to use quarkonia as a thermometer of nuclear matter. For temperatures $T > T_c$ the potential of quarkonia changes due to Debye screening of free color charges as

$$V(r) = -\frac{\alpha}{r} \exp[-r/r_D(T)], \quad (1.6)$$

where $r_D(T)$ is Debye screening radius [19]. When the screening radius is smaller than the radius of quarkonia, heavy quarks coupled in pairs cannot see each other because of the color screening. As the temperature increases, the Debye screening radius decreases, and more tightly bounded states melt in QGP. As J/ψ and $\Upsilon(1S)$ are the ground states of quarkonia and have the smallest radius r_c , they will melt last at temperatures $T \gtrsim 2T_c$ [19].

This fact is also observed in the data from ALICE experiment. In the Figure 1.13 nuclear modification factor of two different states of bottomia is plotted against number of

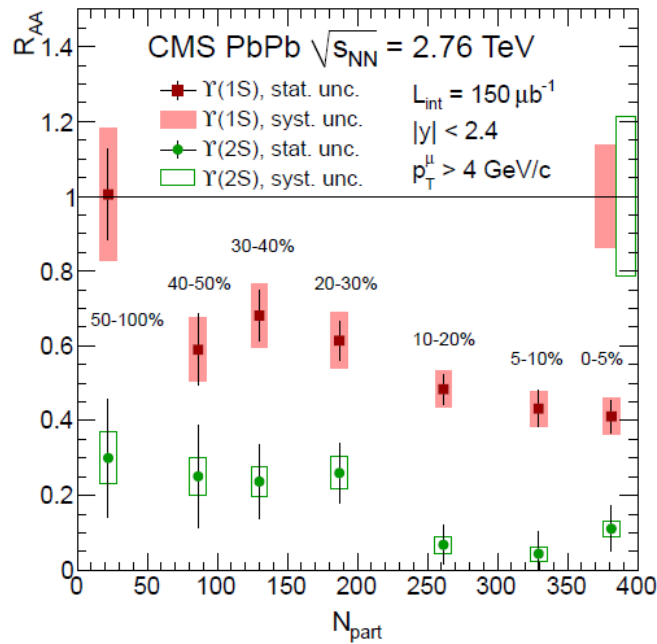


Figure 1.13: R_{AA} of $\Upsilon(1S)$ and $\Upsilon(2S)$ against centrality in Pb+Pb collisions at energy $\sqrt{s_{NN}} = 2.76$ TeV. Taken from Ref. [20].

participants (that is, centrality). The $\Upsilon(2S)$ state is more suppressed than $\Upsilon(1S)$ because it is less bounded, so it deconfines already at lower temperatures and its final production will be lower. Another phenomenon caused by the presence of QGP can be seen. The suppression of both Υ states is increasing with the number of participants.

Except the suppression caused by color screening in QGP, the so called “normal suppression” of quarkonia due to Cold Nuclear Matter effects modifies the final quarkonia production and can be studied in proton-nucleus collisions. This aspect is caused by re-scattering dissociation of the primordially produced quark-antiquark pairs when traversing cold hadronic matter. This suppression also has to be taken into account in nucleus-nucleus collisions. In this case, the particle yield in A+A collisions to “normal yield” is studied [19].

Measurements of the quarkonium suppression due to Cold Nuclear Matter effects were studied in asymmetric Cu+Au collisions at PHENIX experiment. The result can be seen in Fig. 1.14 (left) where measurements of J/ψ in Au+Au and in Cu+Au collisions are shown. The backward rapidity represents the “Au-going” direction and forward rapidity the “Cu-going” direction. The magnitude of suppression of charmonia in Au+Au collisions is similar to backward rapidity R_{AA} , while the “Cu-going” suppression is clearly different, namely lower, than that of Au+Au collisions. This difference between the forward-backward rapidity can be explained by the suppression caused by cold nuclear matter effects as can be seen in Fig. 1.14 (right) where the ratio of forward-to-backward rapidity is compared to model [21]. The additional suppression to the one originating in CNM effects is therefore caused by the effects of hot medium, the QGP [22].

The CNM effects on particle suppression can also be seen in Fig. 1.15. The measurements of heavy flavor electrons in d+Au, Cu+Cu and Au+Au central collisions at $\sqrt{s_{NN}} = 200$ GeV were done by the PHENIX experiment [23]. In the Fig. 1.15 a rising suppression can be seen going from d+Au collisions towards heavy-ion collisions. In d+Au collisions there is no QGP present and CNM effects dominate what results in an enhancement of R_{AA} . On the other hand, a strong suppression in Au+Au collisions is a

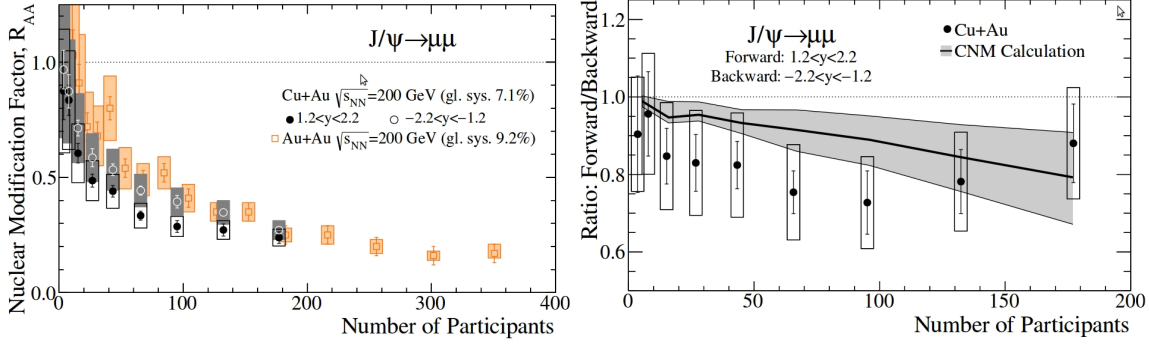


Figure 1.14: Left: R_{AA} of J/ψ in Au+Au and Cu+Au collisions at $\sqrt{s_{NN}} = 200$ GeV measured by the PHENIX Collaboration [22]. Right: Ratio of J/ψ suppression at forward to backward rapidity in Cu+Au collisions compared to theoretical model [21], [22].

hint of the presence of QGP. At collisions of smaller nuclei, Cu+Cu, there is an interplay between the effects of QGP and CNM [23].

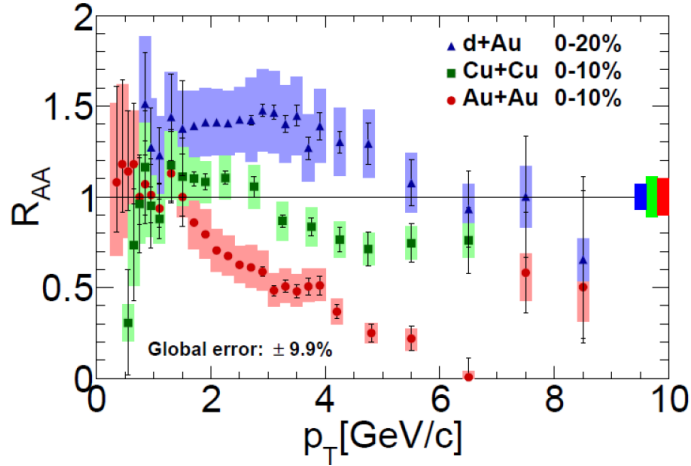


Figure 1.15: R_{AA} of heavy flavor electrons at d+Au, Cu+Cu and Au+Au collisions at $\sqrt{s_{NN}} = 200$ GeV measured by PHENIX. Taken from Ref. [23].

1.7.2 Open heavy flavor

Open heavy flavored particles are those composed of one c or b quark and one light quark. Such particles are D and B mesons containing one charm quark and one bottom quark, respectively. In the Tab. 1.3 the most abundant examples of D and B mesons are listed together with their masses and quark composition.

meson	content	mass [MeV/c ²]	meson	content	mass [Mev/c ²]
D^0	$c\bar{u}$	1864.84	B^0	$d\bar{b}$	5279.58
D^+	$c\bar{d}$	1869.61	B^+	$u\bar{b}$	5279.26
D_s^+	$c\bar{s}$	1968.30	B_s^0	$s\bar{b}$	5366.77

Table 1.3: Properties of open heavy flavor mesons. Taken from Ref. [1].

An important part of the study of open heavy flavor is the suppression of high p_T particles caused by interactions of heavy quarks with the quark-gluon plasma. As was

described before in the section 1.4.1, according to dead-cone effect, heavy quarks should lose less energy in this strongly interacting medium than light quarks because the gluon emission is suppressed in angles smaller than m/E . This should be seen in the plot of nuclear modification factor. The bigger the energy loss is, the smaller is the R_{AA} . Ideally the difference between nuclear modification factors of light, c and b quarks, that is of light hadrons, D and B mesons, should be observed. While the ALICE experiment can see a small hint of difference in R_{AA} at intermediate p_T (Fig. 1.8), the STAR experiment do not recognize between the magnitudes of suppression of light hadrons and D mesons, as can be inferred from the Fig. 1.27. At 0-10% central Au+Au collisions the suppression of D mesons is similar than that of light hadrons marked with the grey band.

Hadronic decay channel of open heavy flavor

D and B mesons can decay via hadronic or semileptonic decay channels. The hadronic decay channel of D^0 mesons is studied via pairing of pions π and kaons K and by calculating their invariant mass. Recent STAR publications of D meson measurements in p+p collisions at $\sqrt{s} = 200$ GeV [24] and Au+Au collisions at $\sqrt{s_{NN}} = 200$ GeV [25] describe the method of obtaining the D meson sample via hadronic decay channel: The high background contribution is described by the mixed-event method, where one particle of the pair $K\pi$ is taken from another event. Such uncorrelated particle pairs should describe the background and are subtracted from the signal. The remaining combinatorial background is further subtracted after fitting it with polynomial function.

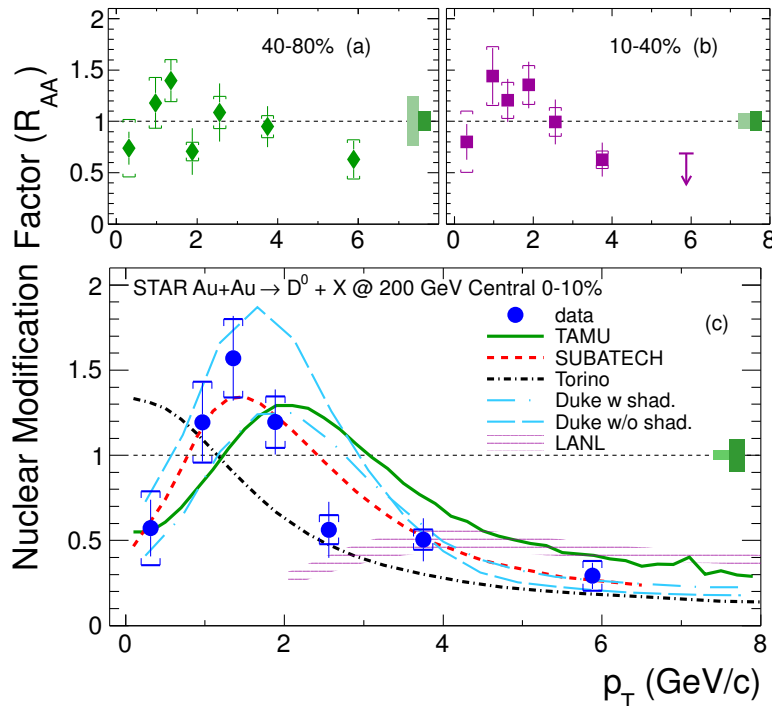


Figure 1.16: Nuclear modification factor of D mesons in Au+Au collisions at $\sqrt{s_{NN}} = 200$ GeV at various centrality classes. The R_{AA} at 0-10% most central collisions is compared to theoretical models. Taken from Ref. [25].

There are also other open charm hadronic decays studied, such as $D^+ \rightarrow K^- \pi^+ \pi^+$, $D^{*+} \rightarrow D^0 \pi^+$ or $D_s^\pm \rightarrow \phi \pi^\pm$. These decays are mainly studied at the ALICE experiment [26], [27], [28], and the final charm cross section or R_{AA} is calculated by combination of

all D meson measurements.

The nuclear modification factor of D mesons, reconstructed via the hadronic decay channel, measured at STAR is shown in Fig. 1.16, for three centrality classes. In peripheral collisions, no suppression is observed [25]. On the other hand, in 0-10% of most central collisions the suppression is significant at $p_T > 3$ GeV/ c . Various model calculations are compared to the data described in detail in Ref. [25]. Generally, the TAMU and SUBATECH group calculations follow the pattern of the data well. There is also a strong indication that Cold Nuclear Matter effects are important at low and intermediate p_T and can cause the enhancement of R_{AA} [25].

Non-photonic electrons

D and B mesons can also decay via semileptonic decay channel $D(B) \rightarrow e\nu_e X$, where X stands for mostly some light hadron. This study of open heavy flavor is also performed at the STAR experiment. In this measurement no invariant mass peak of heavy meson is reconstructed, but the continuous spectrum of electrons from heavy meson decay is studied. The background is mainly composed of the so-called photonic electrons which are created in pairs e^+e^- mainly in γ conversions $\gamma \rightarrow e^+e^-$ or Dalitz decays $\pi^0 \rightarrow \gamma e^+e^-$. The desired heavy flavor electrons are then denoted as non-photonic electrons (NPE), as they are produced alone without any electron pair.

The analysis of NPE has advantages over the hadronic decay channel studies. First, the branching ratio of semileptonic decay channel is higher than the hadronic channel. Also, during data taking STAR is able to trigger on high-energy electrons in the Electromagnetic Calorimeter (BEMC). This kind of trigger is called NPE trigger. It is fired only when the Calorimeter detects a hit with a deposited energy higher than a certain threshold.

The STAR experiment has also performed various studies of open heavy flavor mesons via semileptonic decay channel which are described in more detail in the next section.

1.8 Measurements of non-photonic electrons

The exact procedure of the analysis of non-photonic electrons will be discussed in next chapters as the main topic of this thesis. However, it is appropriate to present here results on NPE at the STAR experiment together with PHENIX measurements and finally some brief description of ALICE results.

1.8.1 Measurements in p+p collisions

Measurements of NPE in p+p collisions at the energy $\sqrt{s} = 200$ GeV is important as a test of perturbative QCD calculations and also as a baseline for the studies of heavy flavor production in heavy-ion collisions, namely the nuclear modification factor R_{AA} . The published STAR results from Year 2008 were studied only at $p_T > 2.5$ GeV/ c [29]. The final NPE invariant spectra agree well with the theoretical calculations of Fixed Order Next-to-Leading Logarithm (FONLL) of pQCD [30] within theoretical uncertainties. The NPE spectra were moreover separated into D and B meson contribution according the results of electron-hadron azimuthal correlations in Ref. [37], which is described in more detail below.

Recent STAR preliminary results on NPE spectra in p+p collisions at $\sqrt{s} = 200$ GeV were done using the data sample from Year 2009 and 2012. In Year 2009 data, the NPE spectra are extended towards low p_T while in Year 2012 data the spectra are obtained up to $p_T = 14$ GeV/ c . The spectra are plotted together in the Fig. 1.17 also with the published

STAR data from Year 2008 and PHENIX results from Year 2005 [31]. The spectra are plotted only up to $p_T = 8$ GeV/c for better comprehensibility.

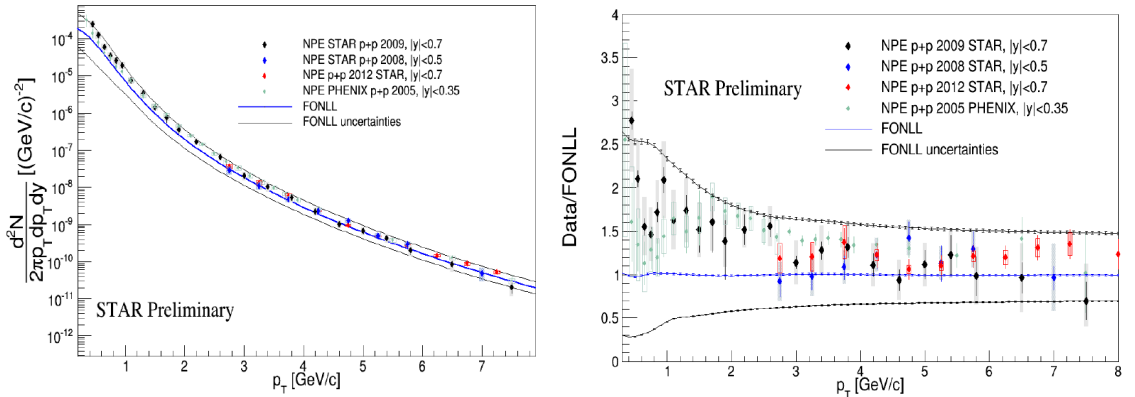


Figure 1.17: Left: Invariant yield of non-photonic electrons compared to FONLL pQCD calculations from Ref. [30]. Published STAR data from Year 2008 [29], PHENIX results from Year 2005 [31], as well as the preliminary STAR results from Years 2009 and 2012 are shown. Right: Ratio of measured invariant yield of non-photonic electrons to FONLL pQCD theoretical calculations. Taken from Ref. [29], [30], [31].

The NPE spectra agree well with each other and are also contained within the theoretical uncertainties of FONLL pQCD calculations. For better understanding the ratio of data to FONLL was drawn in the Fig. 1.17 (right). It can be inferred from the plot that the data are shifted towards the upper boundary of FONLL uncertainty but they still follow the FONLL calculations within the range of error bars.

The ALICE experiment also published results of heavy flavor electrons originating in semileptonic decays of open heavy flavor mesons. They measured electrons both from D and B meson decays [32] and electrons originating only in B meson decays [33] in p+p collisions at the energy of $\sqrt{s_{NN}} = 2.76$ TeV. The spectra are compared to three different theoretical pQCD calculations and in all cases the data agree well with the calculations within the uncertainties [32], [33]. Measurements of electrons from decays of D and B mesons in p+p collisions at $\sqrt{s_{NN}} = 7$ TeV and only B meson semileptonic decays at the same collisions and energy were also published by the ALICE experiment [34], [35]. Again, both heavy flavor electron spectra are consistent with pQCD theoretical calculations within uncertainties.

1.8.2 D and B meson contribution to NPE yield

Non-photonic electrons originate in semileptonic decay channels of open heavy flavor mesons, namely D and B . Theoretical studies were made on the relative contribution of these mesons to the NPE spectra in Ref. [36]. This paper showed that D meson decays dominate at low p_T , while at high p_T there is an equal charm and bottom contribution to NPE.

As STAR detector did not possess any silicon vertex detector close to the beam pipe which would be able to reconstruct the decay vertices of heavy flavor mesons, the e-h azimuthal correlations had to be made in order to separate the relative D and B meson contribution. An example of distribution of azimuthal angle between NPE and hadron is shown in the Fig. 1.18. The data are fitted with a function that represents a combination of simulated charm and bottom distributions by PYTHIA. The basic function shape is

$y = x * D + (1 - x) * B$, where D and B are the relative contributions. By adapting this function to the distribution of azimuthal angle one can extract the parameter x .

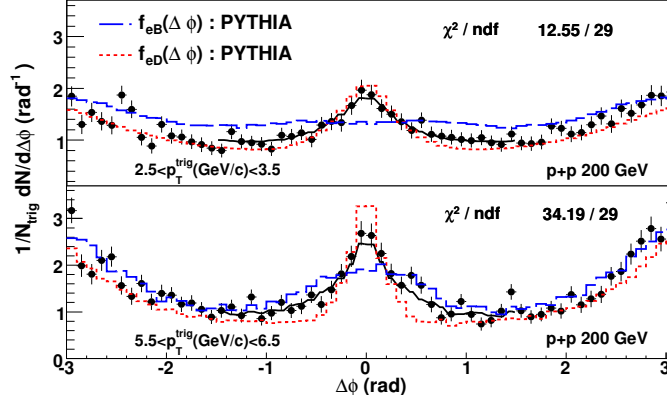


Figure 1.18: Distribution of azimuthal angle between non-photon electron and hadron in p+p collisions at $\sqrt{s} = 200$ GeV from the STAR experiment. Taken from Ref. [37].

In the Fig. 1.19 the relative contribution of B mesons to the NPE yield, i.e. $B/(D+B)$, is plotted as a function of transverse momentum. The rise of bottom contribution with increasing p_T is visible as was expected from theoretical calculations discussed above [37].

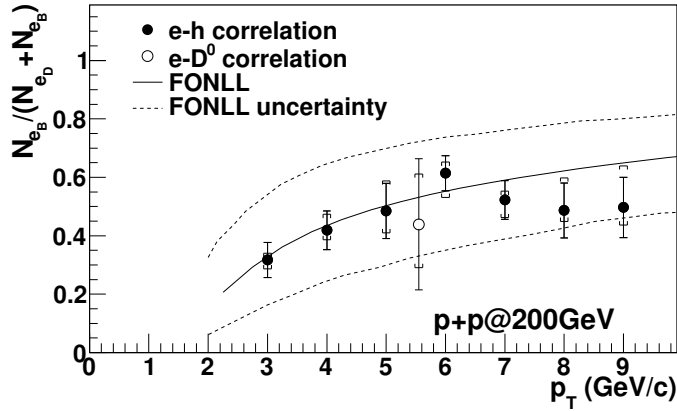


Figure 1.19: Relative B meson contribution to the non-photon electron yield. Taken from Ref. [37].

1.8.3 Measurements in heavy-ion collisions

The effects of QGP on heavy quarks can be studied in heavy-ion collisions. STAR experiment published results of nuclear modification factor of NPE in Au+Au collisions at $\sqrt{s_{NN}} = 200$ GeV taken in Year 2003 [38]. The R_{AA} reveal a large suppression at high p_T , which indicates the energy loss of heavy quarks due to strong interaction in QGP [38], as can be seen in the Fig. 1.20.

Results on NPE nuclear modification factor in Cu+Cu and Au+Au collisions at $\sqrt{s_{NN}} = 200$ GeV were published also by the PHENIX experiment [39], [40]. The data reveal a strong suppression of non-photon electrons at high p_T in the most central collisions in both collisional systems (Fig. 1.21).

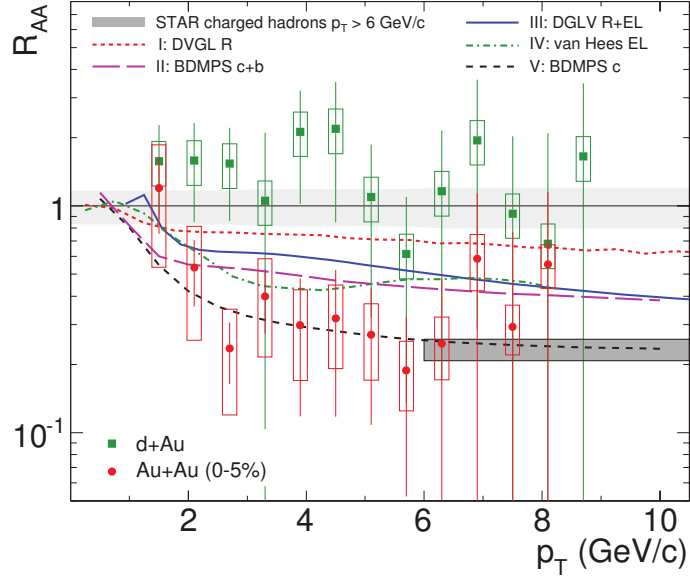


Figure 1.20: Nuclear modification factor of NPE in Au+Au collisions at $\sqrt{s_{NN}} = 200$ GeV from Year 2003. Taken from Ref. [38].

Recent preliminary results on R_{AA} of NPE in 0-10% central Au+Au collisions from Year 2010 at $\sqrt{s_{NN}} = 200$ GeV at STAR experiment also show large suppression at high p_T which can be seen in the Fig. 1.22. The nuclear modification factor is also compared to theoretical models based on different types of energy loss of heavy quarks inside the QGP.

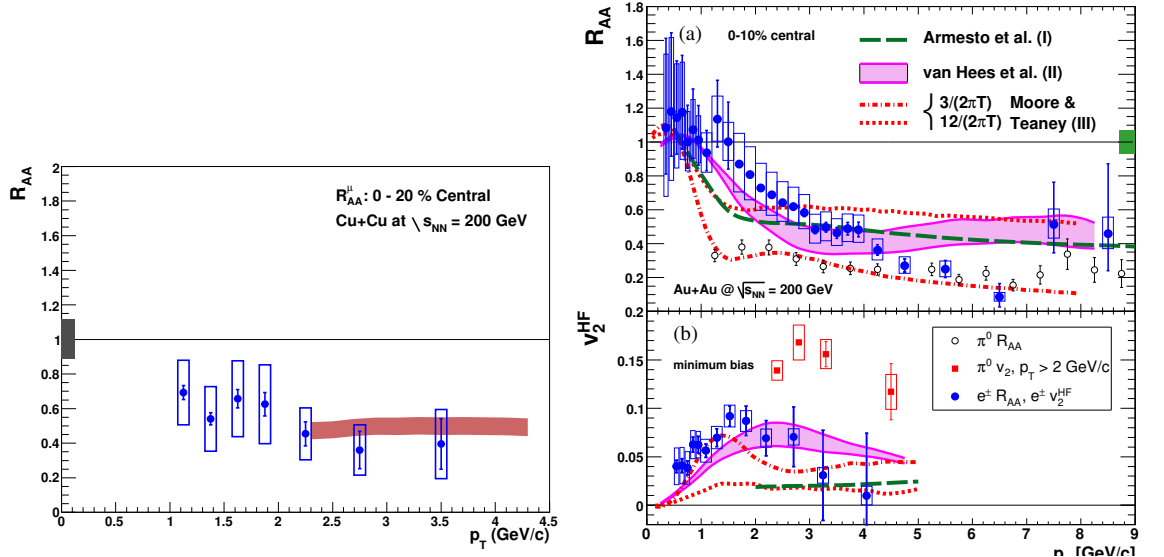


Figure 1.21: Left: R_{AA} of NPE in 0-20% central Cu+Cu collisions measured by PHENIX together with theoretical calculations [39]. Right: R_{AA} of NPE in 0-10% central Au+Au collisions measured by PHENIX together with theoretical predictions [40].

The DGLV Rad. model [41] marked with dashed green line considers only gluon radiation energy loss mechanism and does not describe the suppression at high p_T . A DGLV model which moreover includes the collisional energy loss (DGLV Rad. + El.) predicts larger suppression compared to the previous one. The non-perturbative approach

to quark energy loss presented by He *et al.* [42] is marked with magenta line. The BAMPS partonic transport model [43], [44] marked with black dashed line calculates the quark energy loss due to elastic collisions with the medium. A collisional dissociation model represented by the red line uses the energy loss caused by the dissociation of heavy mesons in the strongly interacting medium [45]. This model, together with the Ads/CFT model [46], agree well with the data at high p_T . Finally, the model described by Gossiaux *et al.* [47], [48] calculates the radiative and collisional energy loss using pQCD description with non-perturbative corrections.

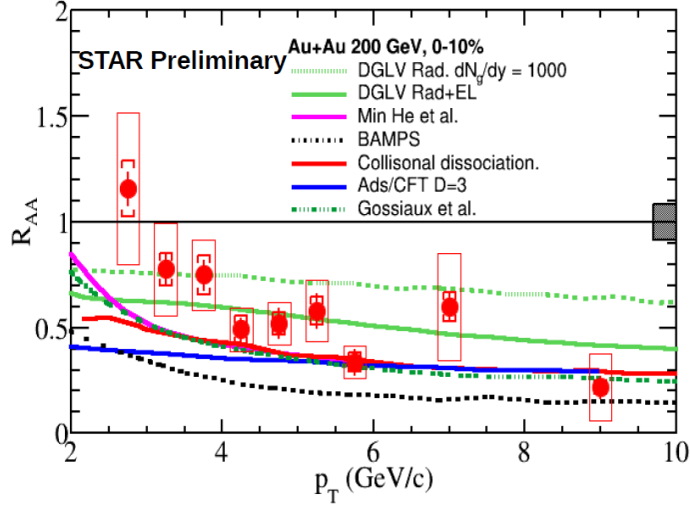


Figure 1.22: Preliminary results on nuclear modification factor of NPE in 0-10% Au+Au collisions at $\sqrt{s_{NN}} = 200$ GeV compared to theoretical models described in more detail in the text.

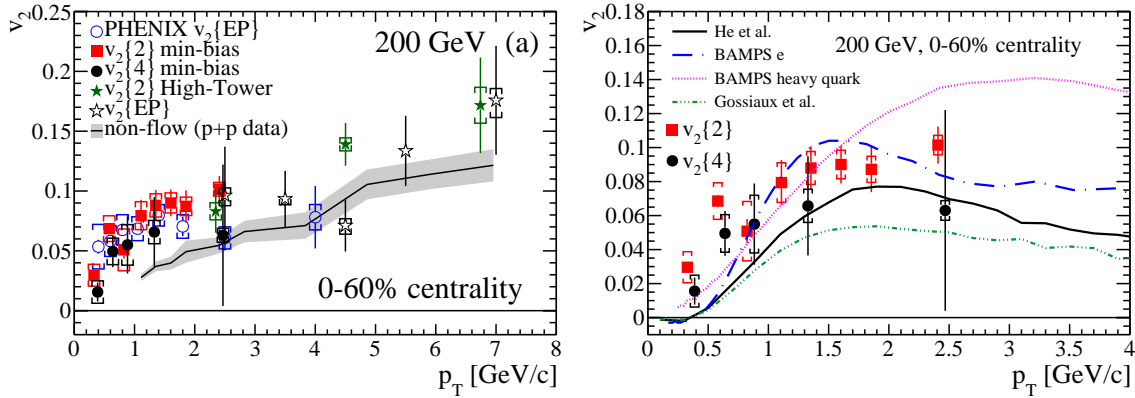


Figure 1.23: Left: Results on measurements of NPE v_2 from STAR and PHENIX. The non-flow contribution at high p_T is marked with the black line and its uncertainties by the grey band. Right: The v_2 measurements compared to theoretical models [42], [43], [44], [47], [48]. Taken from Ref. [50].

Measurements of NPE elliptic flow were studied in Au+Au collisions at $\sqrt{s_{NN}} = 200$ GeV at STAR [50]. Figure 1.23 (left) shows STAR results using 2- and 4-particle correlations and event-plane method, $v_2\{2\}$, $v_2\{4\}$ and $v_2\{EP\}$, respectively. More detailed description of this analysis procedure is given in Ref. [49]. At low p_T we observe finite v_2 which is also seen by the PHENIX experiment marked with blue circles. At $p_T > 4$ GeV/c the increasing flow can be described by jet-like correlations from non-flow data from p+p

collisions which is represented by the black line.

On the right side of the Fig. 1.23 the elliptic flow data are compared with theoretical models which were also used for the description of R_{AA} and are explained in more detail above or in Ref. [50]. Generally, models which are able to reproduce experimental results of v_2 are not able to follow the magnitude of suppression in NPE R_{AA} . However, it can be concluded from the measurement that charm quarks interact strongly with the medium leading also to finite elliptic flow [50].

The ALICE experiment is able to distinguish between charm and bottom contribution to non-photonic electrons. In Fig. 1.24 the nuclear modification factor of electrons originating in decays of B mesons is shown. There is a clear evidence of strong suppression at high p_T which indicates energy loss of beauty quarks in the quark-gluon plasma [51].

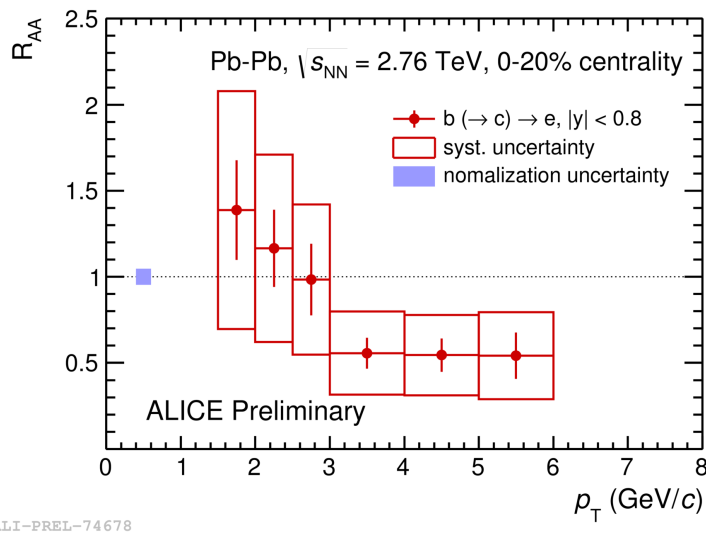


Figure 1.24: R_{AA} of non-photonic electrons from beauty decays in central Pb+Pb collisions at $\sqrt{s_{NN}} = 2.76$ TeV. Taken from Ref. [51].

1.8.4 Measurements at lower beam energies

Another preliminary result on nuclear modification factor was done by STAR Collaboration in Au+Au collisions at the energy of $\sqrt{s_{NN}} = 62.4$ GeV and is shown in the Fig. 1.25 (left). The baseline measurements are not available at these beam energies with satisfactory precision therefore, the Au+Au spectra had to be divided by theoretically calculated p+p spectra using pQCD [52]. Contrary to 200 GeV collisions, the R_{AA} does not reveal any suppression pattern. In fact, the data are consistent with unity within theoretical uncertainties. This can be caused by Cold Nuclear Matter effects, which seems to be more dominant at these energies and need to be studied further.

The PHENIX experiment also obtained results on nuclear modification factor of NPE in Au+Au collisions at $\sqrt{s_{NN}} = 62.4$ GeV [53]. As can be seen in the Fig. 1.25 (right) the R_{AA} is consistently larger than one, which coincides with the STAR measurements.

Elliptic flow was also measured at lower beam energies as can be seen in Fig. 1.26. v_2 obtained with 2-particle correlations at $\sqrt{s_{NN}} = 39, 62.4$ and 200 GeV is shown as a function of p_T . At lower beam energies no flow is observed. These results are statistically lower than that at $\sqrt{s_{NN}} = 200$ GeV [50].

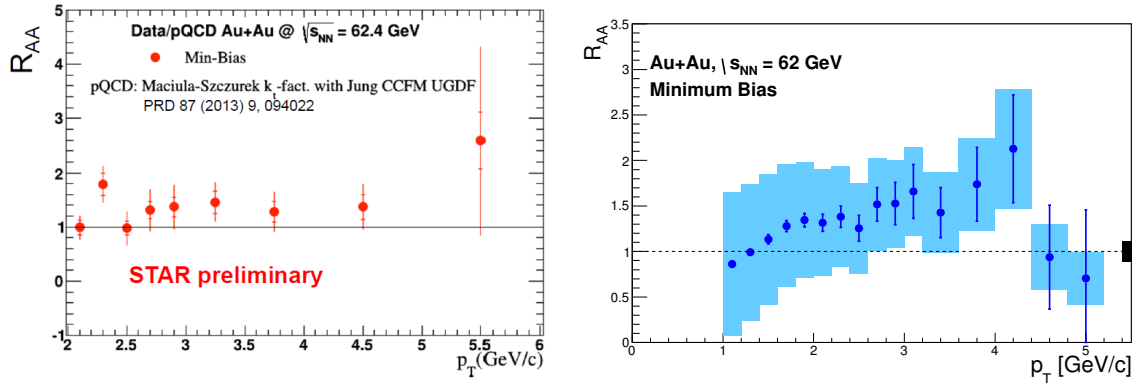


Figure 1.25: Left: Preliminary results on nuclear modification factor of NPE in minimum-bias Au+Au collisions at $\sqrt{s_{NN}} = 62.4$ GeV at STAR. Right: The R_{AA} measurement in minimum-bias Au+Au collisions at $\sqrt{s_{NN}} = 62.4$ GeV at PHENIX experiment. Taken from Ref. [53].

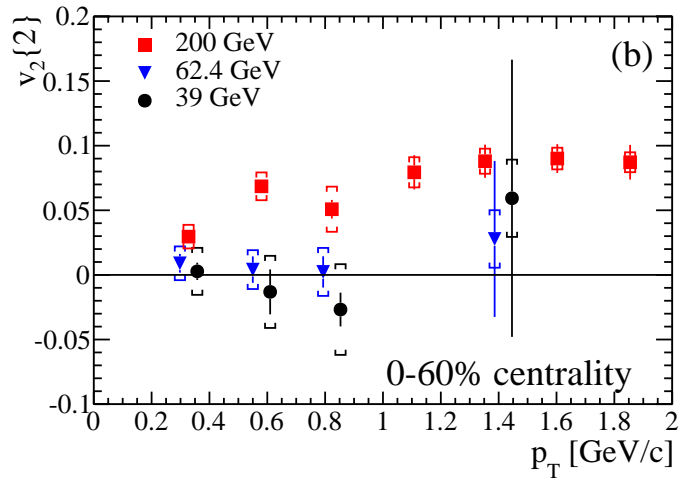


Figure 1.26: Elliptic flow measurements in Au+Au collisions at $\sqrt{s_{NN}} = 39, 62.4$ and 200 GeV. Taken from Ref. [50].

1.9 STAR measurements in uranium collisions

Collisions of uranium nuclei were taken by the STAR experiment at energy $\sqrt{s_{NN}} = 193$ GeV in Year 2012. Measurements of heavy flavor mesons were performed and the preliminary results will be discussed in this section.

Studies of suppression of D mesons in uranium collisions at the energy of $\sqrt{s_{NN}} = 193$ GeV were compared to Au+Au collisions at $\sqrt{s_{NN}} = 200$ GeV. As was mentioned above, more suppression is expected in U+U with respect to Au+Au collisions with increasing centrality. Recent preliminary results of D meson measurements via hadronic decay channel in U+U collisions at different centrality classes are shown in the Fig. 1.27.

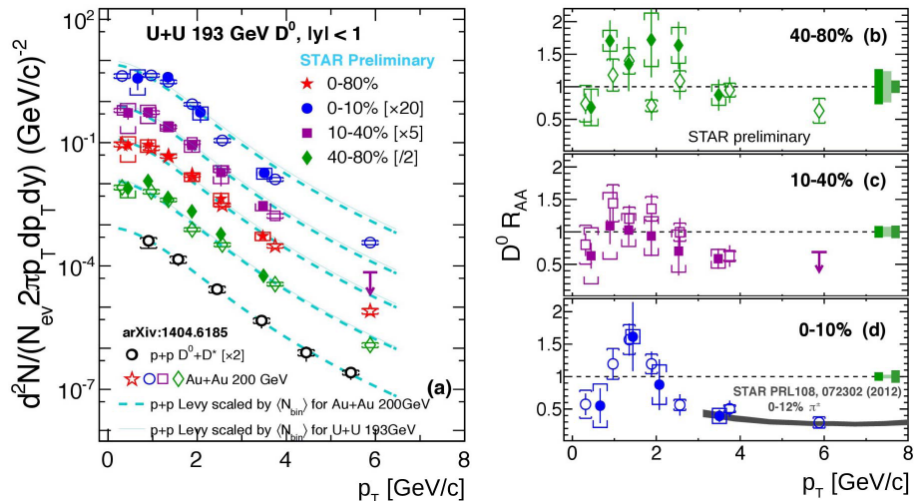


Figure 1.27: Preliminary results on D meson suppression in U+U collisions compared to Au+Au collisions [25]. On the left, the spectra at different centrality classes are shown together with the p+p baseline. On the right side the nuclear modification factor of D mesons in U+U and Au+Au collisions at different centralities is shown and at 0-10% central collisions compared to suppression of light hadrons.

On the left side of the Fig. 1.27 the spectra of D mesons are plotted at 0-10%, 10-40% and 40-80% central U+U and Au+Au collisions together with minimum-bias data and spectra from p+p collisions used as baseline. The data are scaled with different scaling factor for better comprehensibility. On the right side of the Fig. 1.27 the nuclear modification factor R_{AA} is shown in the above mentioned centrality classes of U+U and Au+Au collisions. The suppression magnitude of D mesons is the same in both uranium and gold collisions and at central collisions also to pion suppression. It can be inferred from these results that the larger suppression caused by larger energy density expected in uranium collisions is not visible at 0-10% centrality given the uncertainties.

Dependence of the nuclear modification factor of D^0 mesons on centrality is shown in Fig. 1.28 in Au+Au and U+U collisions at $\sqrt{s_{NN}} = 200$ GeV and $\sqrt{s_{NN}} = 193$ GeV, respectively. The R_{AA} of pions is also included in the figure in order to show that both light and heavy flavor suffer the same magnitude of suppression. The data from U+U collisions are extended towards higher $\langle N_{part} \rangle$ and it can be seen that the trend of suppression is the same.

Results on quarkonium production in U+U collisions at $\sqrt{s_{NN}} = 193$ GeV are shown in Fig. 1.29. On the left panel the R_{AA} of J/ψ is plotted as a function of p_T for U+U minimum-bias collisions and is compared to results from Au+Au minimum-bias collisions at $\sqrt{s_{NN}} = 200$ GeV [54]. The magnitude of suppression from both collision systems is the same within uncertainties.

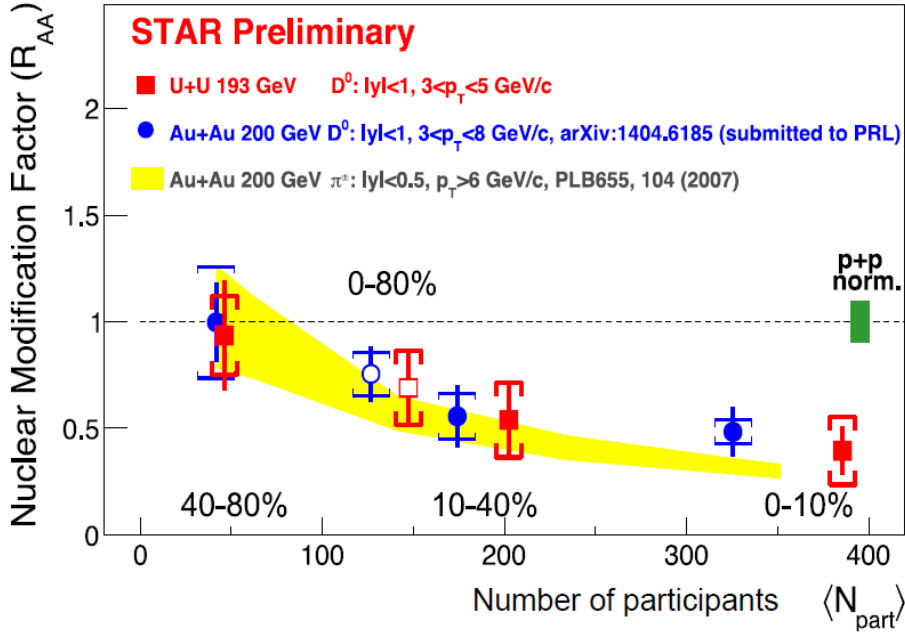


Figure 1.28: Preliminary results on D^0 meson suppression in U+U and Au+Au collisions as a function of centrality ($\langle N_{part} \rangle$). The yellow band represents the R_{AA} of pions in Au+Au collisions at $\sqrt{s_{NN}} = 200$ GeV.

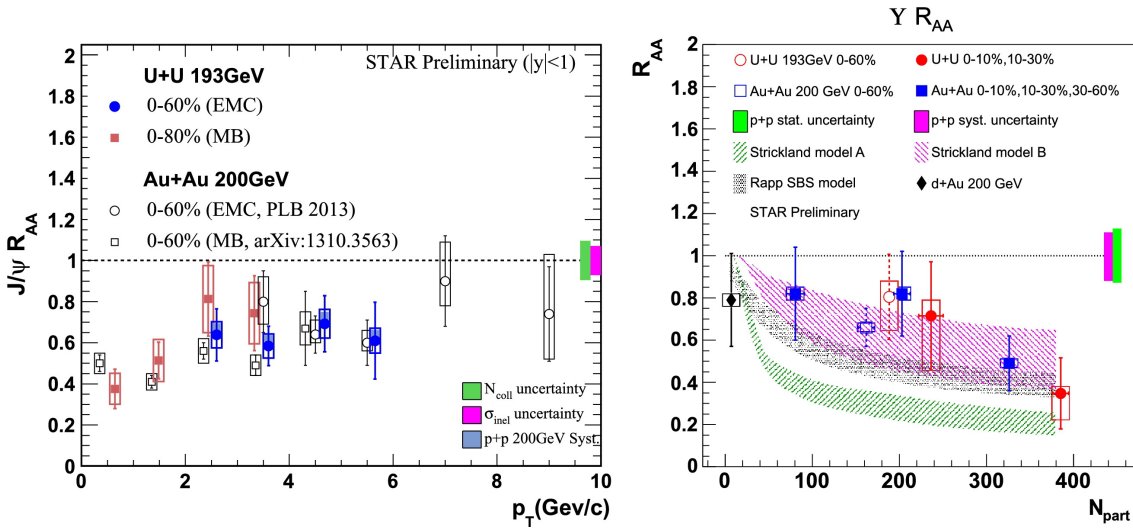


Figure 1.29: Left: Nuclear modification factor of J/ψ as a function of p_T in min-bias U+U collisions at $\sqrt{s_{NN}} = 193$ GeV and min-bias Au+Au collisions at $\sqrt{s_{NN}} = 200$ GeV [54]. Right: R_{AA} of Υ with respect to number of participants in U+U collisions at $\sqrt{s_{NN}} = 193$ GeV, d+Au and Au+Au collisions at $\sqrt{s_{NN}} = 200$ GeV [55] compared to theoretical models [56], [57].

Suppression of Υ production is plotted as a function of centrality in Fig. 1.29 (right) in U+U collisions at $\sqrt{s_{NN}} = 193$ GeV and also Au+Au and d+Au collisions at $\sqrt{s_{NN}} = 200$ GeV [55]. A strong suppression in central events is observed in U+U collisions and is consistent with the magnitude of suppression in Au+Au collisions. The results are compared to theoretical models [56], [57].

1.10 Future STAR plans

As could be inferred from the overview of measurements done at RHIC, a variety of collision systems at different beam energies were studied. Despite the already achieved results there are still many interesting physics topics which need to be investigated. Many of them are subjects of future plans of RHIC and STAR experiment.

Heavy flavor observables are an important probe to test the properties of QGP via their interactions with this medium. Results obtained up to now can be done with even more precision using the two new detectors installed at STAR: Heavy Flavor Tracker (HFT) and Muon Telescope Detector (MTD). Thus, next two years STAR will be focused on the heavy flavor measurements because the HFT will allow us to study the decay vertex of charm mesons and with MTD the muon decay channel of quarkonia can be measured. The need for the study of Cold Nuclear Matter effect leads to planned collisions of heavy nucleus with polarized proton. These collision system will also allow us to know more about the spin structure of proton.

The Beam Energy Scan II program is planned for 2018-2019. Energies of collisions of gold nuclei will range from 5 to 20 GeV in order to determine the critical point of the phase diagram of hadronic matter and study the QCD phase structure in more details. In this period also collisions of smaller nuclei are planned, such as Si+Si, Cu+Cu and In+In.

After further upgrade of the detector system even the decay vertices of B mesons could be observed. Also, more precise measurements of jets could be performed during the Years 2020 and 2023. Again collisions of polarized proton and heavy nucleus will be on the schedule in order to further study the CNM effects.

Transition from RHIC to eRHIC awaits us in 2025 which means turn away from the studies of QGP and focus on the gluon structure of hadronic matter. Collisions of electrons with protons or heavy nuclei will take place. This will also require the upgrade of the experiments which will be known as eSTAR and sPHENIX. More about the future RHIC plans can be found in Ref. [58], [59].

Chapter 2

The STAR Experiment

The Relativistic Heavy Ion Collider (RHIC) (Fig. 2.1) located in Brookhaven National Laboratory in state New York USA is only dedicated accelerator for studies of quark-gluon plasma. It started its performance in the Year 2000 with the aim of observing the hot and dense form of matter and to study the spin structure of proton. Two experiments are now active on this accelerator: PHENIX and STAR. The STAR detector is better suited for the study of QGP and was used for the analysis described in this thesis, therefore it is going to be presented in more detail below. RHIC is unique due to its ability to collide various collisional systems at various beam energies. Collisions taken with this accelerator are p+p, d+Au, Cu+Au, Cu+Cu, Au+Au and U+U. The center of mass energy of p+p collisions can rise up to 500 GeV, while heavy ions are collided at energies 200 GeV for Au+Au and 193 GeV for U+U. The Beam Energy Scan (BES) program let the gold nuclei collide at various energies from $\sqrt{s_{NN}} = 7.7$ GeV to $\sqrt{s_{NN}} = 62.4$ GeV in order to scan the boundary of the phase transition from hadronic matter to QGP [6].

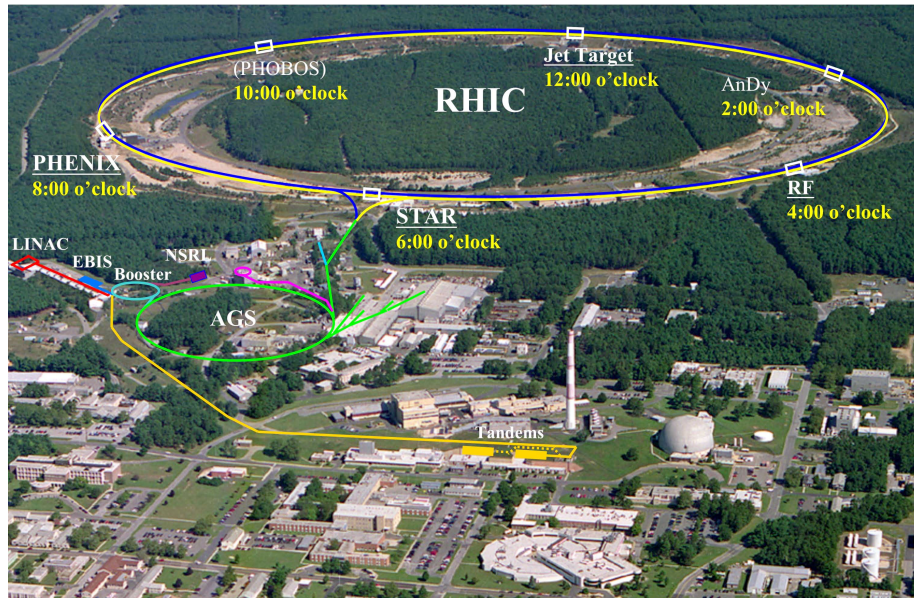


Figure 2.1: Relativistic Heavy Ion Collider RHIC together with other systems which pre-accelerate the beams of protons and heavy nuclei.

STAR (Solenoidal Tracker at RHIC) is located at one of the six intersection points of RHIC beam pipes. It covers 2π azimuth around the beam pipe, two units of pseudorapidity around midrapidity and is composed of various systems. The most important

detectors for heavy flavor physics are the Time Projection Chamber, Time of Flight, Barrel Electromagnetic Calorimeter and lately added new detectors Heavy Flavor Tracker and Muon Telescope Detector. A magnet covers all the above mentioned detectors except the MTD. The magnet is needed for creating a magnetic field with strength of 0.5 T to bend trajectories of charged particles which helps in particle identification. A picture of the STAR detector is shown in Fig. 2.2.

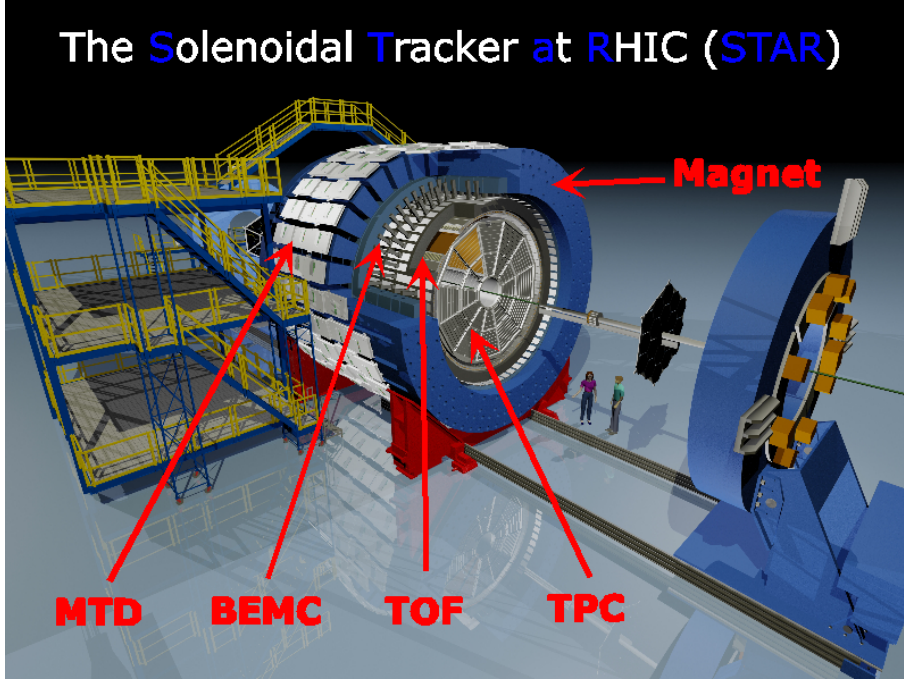


Figure 2.2: A scheme of the STAR detector. Picture done by Alex Schmach.

2.1 Time Projection Chamber

The Time Projection Chamber is the main subdetector of STAR. It is designed to detect trajectories of charged particles and to provide particle identification via their energy loss. TPC is cylindrically shaped gas detector with long response. Its inner radius is 50 cm and the outer radius 200 cm. It is 420 cm long and covers 2π in azimuth and pseudorapidity $|\eta| \leq 1$ [60]. It can distinguish pions from kaons up to $p \sim 0.6$ GeV/c, as can be seen from the Fig. 2.3.

When a particle traverses some material, it loses energy by ionization or radiation. In case of TPC the ionization losses are important and can be described by Bethe-Bloch formula [1]

$$-\left\langle \frac{dE}{dx} \right\rangle = K \frac{Z}{A} \frac{z^2}{\beta^2} \left[\frac{1}{2} \ln \frac{2m_e c^2 \gamma^2 \beta^2 T_{max}}{I^2} - \beta^2 - \frac{\delta(\beta\gamma)}{2} \right], \quad (2.1)$$

where K is a constant, Z and A are proton number and atomic number of the material respectively, z is proton number of incoming particle, I is mean excitation energy, T_{max} is maximum transfer energy for one collision and the last member $\delta(\beta\gamma)/2$ is a correction for density effects at high energies [1]. Every particle loses different amount of energy when traversing the same material. Therefore, by investigating the shape of Bethe-Bloch function the particle identification can be performed. In Fig. 2.3 an example of particle identification is shown. The colored curves are fits using the Bethe-Bloch formula for different particles.

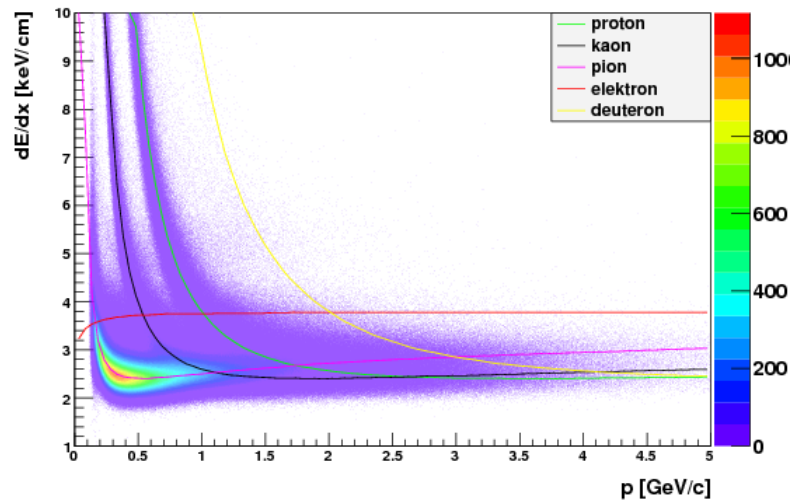


Figure 2.3: Energy loss as a function of momentum. The colored curves represent a fit using the Bethe-Bloch formula for different particles.

2.1.1 How does TPC work

Time Projection Chamber is composed of central high voltage cathode and two anodes located at both sides. A schematic picture of TPC can be seen in Fig. 2.4.

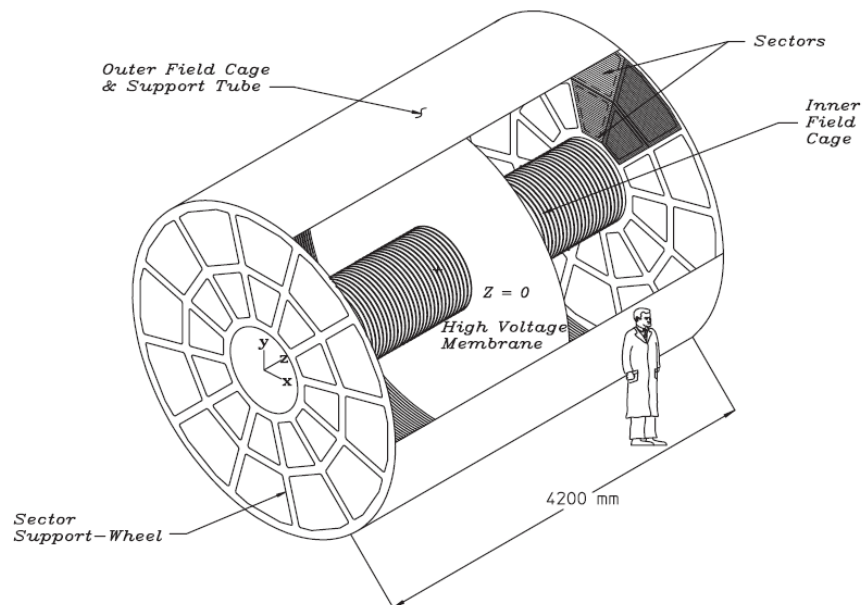


Figure 2.4: Time projection chamber. Taken from Ref. [61].

There is an electric field parallel to the beam pipe and also a parallel magnetic field created by the magnet that is wrapping every subdetector of STAR except MTD. The TPC is filled with gas thus, when a particle traverses this medium, it ionizes molecules of the gas and electron-ion pairs are formed. Created ions are gathered by electrodes of corresponding opposite charge. Right before the anodes the electric field is stronger. Incoming electrons will then have enough energy to ionize the gas and create even more electron-ion pairs. Townsend avalanches are created that are needed for signal readout.

During avalanches there are a lot of positively charged ions generated which cause the decrease of intensity of electric field. For that reason there is a ground grid that collects positive ions and it also divides the region of avalanches from the rest of TPC [62].

Anodes consist of endcap wire chambers, where anode wires are distributed uniformly. Parallel to these wires there are series of cathode square stripes. This configuration allows us to determine the projection of particle track on $x - y$ plane. The x coordinate is obtained from the position on the anode wire, the y coordinate from a cathode strip from parallel line to the anode wire and finally the z coordinate is given by the time in which electrons reach the anode. By this procedure the 3D reconstructed particle trajectory is obtained [62].

The gas that the TPC is filled with is a compound of 90% of Argon and 10% of Methan. The noble gas is convenient because it does not need to attach another electrons so there will not be problems with electron losses due to their binding with molecules of the gas. The organic gas is important due to its ability to quench UV photons which can cause molecule excitations and adjacent non-willing creation of electron-ion pairs. There will be a change of gas mixture from Argon-Methane to Helium(50%) and Ethane(50%) what will increase the efficiency [61].

2.2 Time of Flight

The Time of Flight (TOF) detector is an important subsystem of STAR for the improvement of particle identification. It is capable of distinguishing pions from kaons up to $p \sim 1,5 \text{ GeV}/c$ and protons from $p \sim 1 \text{ GeV}/c$ up to $p \sim 3 \text{ GeV}/c$. In Fig. 2.5 an example of particle identification is shown. The colored curves represent a theoretical predictions of inverse β according to the formula 2.2. Comparing to Bethe-Bloch functions obtained from TPC (Fig. 2.3) it is clear that TOF can distinguish better between the particles up to higher momenta than TPC.

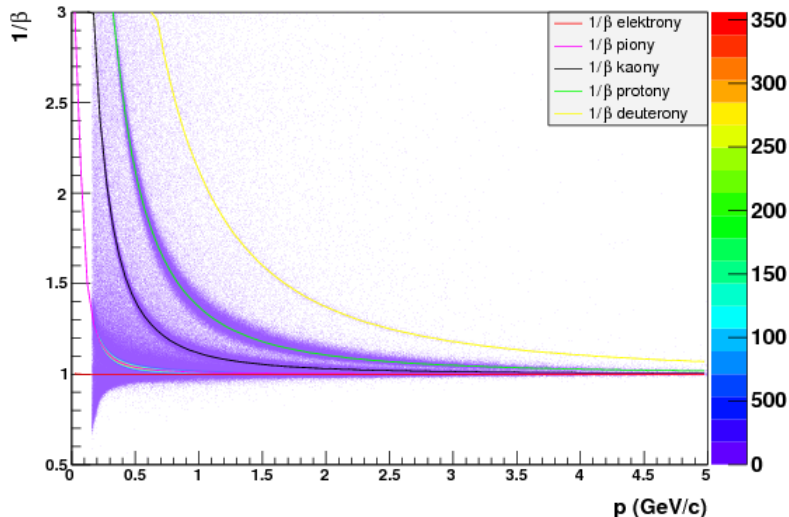


Figure 2.5: Particle identification using Time of Flight. The colored curves are theoretical values from calculation of the inverse β .

The ToF is able to measure the time of flight of the particle, where the starting time is determined by Vertex Position Detector (VPD) and the end time by ToF. From the time difference and known distance which particle travels between the two detectors it is

possible to calculate the velocity β . Together with the momentum obtained from TPC one can identify the particle, i.e. calculate its mass according to following formula

$$m = p \sqrt{\frac{1}{\beta^2} - 1}. \quad (2.2)$$

The Time of Flight detector surrounds the TPC and it covers full azimuth 2π and pseudorapidity $|\eta| \leq 1$. It works on the base of Multi-gap Resistive Plate Chambers (MRPC) which has good time resolution around 100 ps and high detection efficiency of more than 95% [63].

2.3 Barrel Electromagnetic Calorimeter

The Barrel Electromagnetic Calorimeter (BEMC) is important part of STAR as it measures the energy of particles and it also serves for high-tower triggers. High-tower trigger is fired when there is an event with at least one hit with energy higher than some threshold value [64].

The BEMC again covers full azimuth 2π , pseudorapidity $|\eta| \leq 1$ and its inner radius is 220 cm. It consists of 120 calorimeter modules and each module is composed of 40 towers thus the entire BEMC has 4800 towers in total. Inside every module there are lead and scintillator plates alternating. When particle passes through, a shower is created in lead plate, and the signal is read out in the adjacent scintillator plate. Scintillator is a very promising material for the detection of energy of particles due to its fast response and its signal which is proportional to the amount of γ created in the scintillating part [64].

There are also Shower Maximum Detectors (SMD) at a distance of $5X_0$ from the front face, where usually the showers created by incoming particles reach their maximum. X_0 is radiation length i.e., the distance in which the electron loses its energy to $1/e$ of its original value. The SMD detectors are important in the analysis of NPE for better electron identification. The SMD detectors are arranged in η direction and in ϕ direction. These detectors are needed to provide good spatial resolution because the towers are larger than the size of EM shower caused by electron. In Fig. 2.6 a picture of one BEMC module is shown.

2.4 Vertex Position Detector

A detector is needed which would be able to provide information about the interaction vertex. Such a detector is called the Vertex Position Detector (VPD). It consists of two parts, one on each side of STAR, which are wrapped around the beam pipe. This detector is capable of detecting the collision time and therefore is used as trigger detector which can send signal to other detectors to start taking data.

The VPD is detecting prompt photons which are created at the time of a collision and are moving in forward direction towards the VPDs. Thus, the detector consists of Pb converter, scintillator and finally a photomultiplier. From the knowledge of the distance between the two VPD assemblies and time when the prompt γ arrived, the time and position of the collision can be calculated. Taken from Ref. [65].

2.5 Heavy Flavor Tracker

The Heavy Flavor Tracker (HFT) is a silicon pixel detector, that is designed to improve the analysis of heavy flavor measurements. It will be able to distinguish the decay vertices

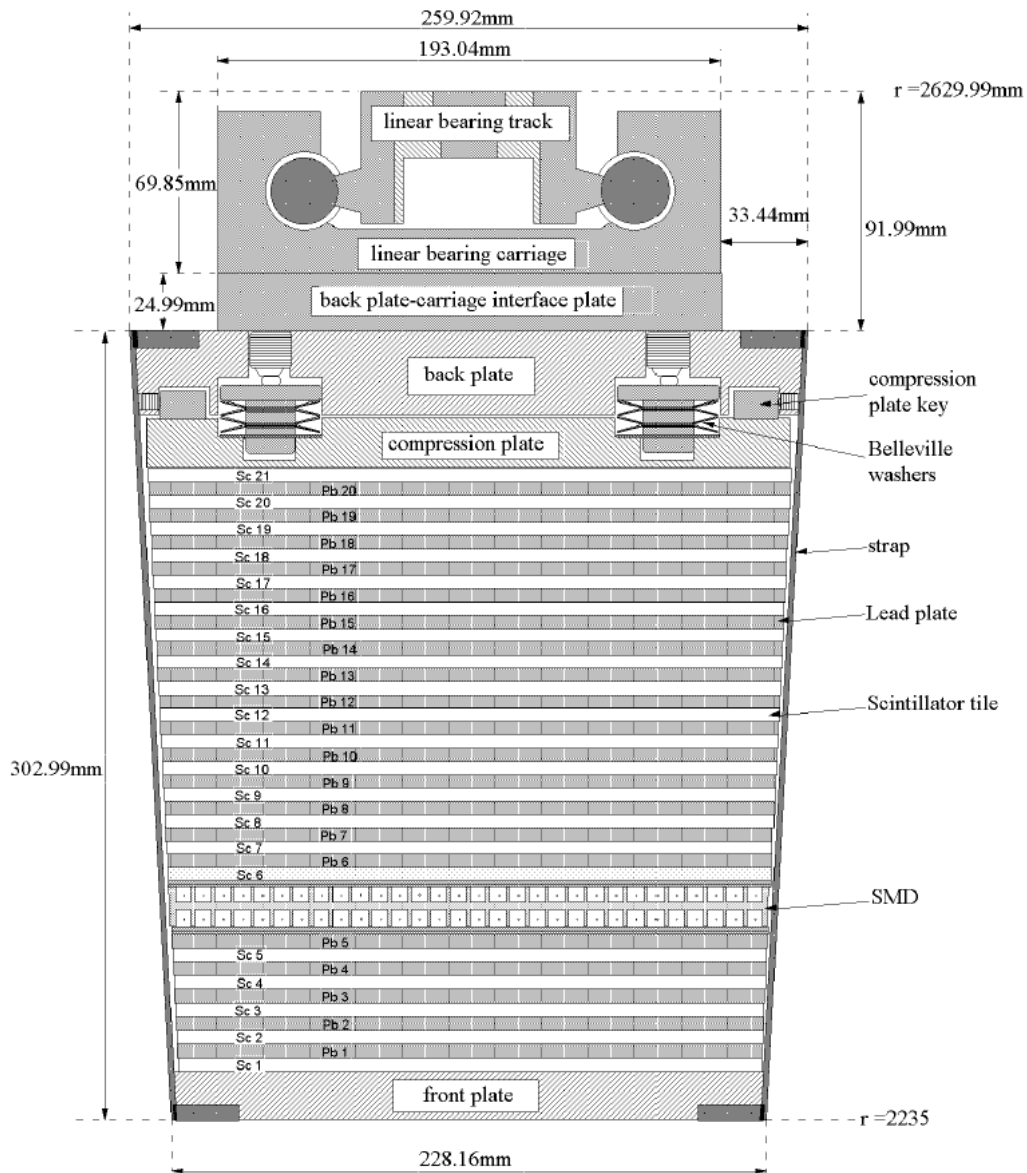


Figure 2.6: Picture of one module of BEMC. Taken from Ref. [64].

of D and B mesons, which will significantly help in the precision of data analysis. In Fig. 2.7 a scheme of this detector is shown. It is placed close to the beam pipe, and it consists of approximately $2\text{ cm} \times 2\text{ cm}$ silicon plates [66]. The closure of HFT to the beam pipe is required because of the very short path traversed by heavy flavor mesons before they decay.

In Fig. 2.8 there is a D^0 meson signal from simulation using the hits in the HFT detector. Various selection criteria on secondary decay vertices of D mesons are applied and are shown on different pictures. The signal is clearly visible above the background. We are not able to see such a good signal in D meson reconstruction in present analysis.

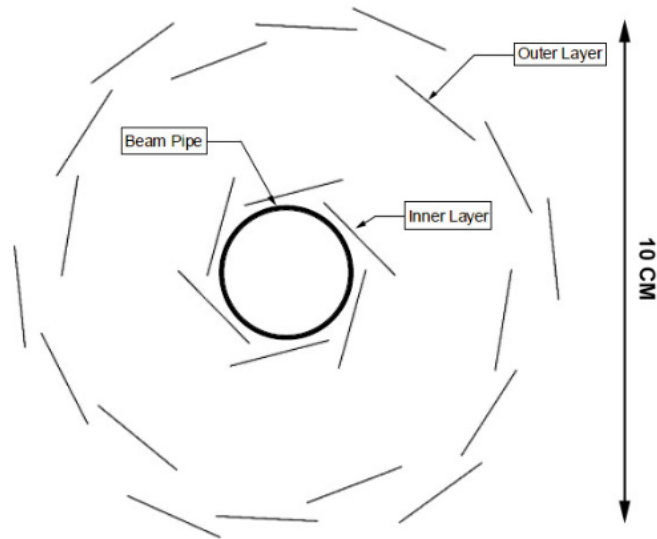


Figure 2.7: Scheme of Heavy Flavor Tracker - transverse cut. Taken from Ref. [66].

2.6 Muon Telescope Detector

The Muon Telescope Detector (MTD) is a newly installed detector that is located on top of the magnet of STAR. Main advantage of this detector is very low hadronic background due to its position. Mainly muons will pass through the steel backlegs of the magnet to MTD while almost all other particles, mainly hadrons, will be stopped in the amount of material of STAR. Therefore, it will be possible to see clear peaks of particles decaying into muons with low noise. An example is shown in Fig. 2.9. With MTD one can study J/ψ and Υ via the muonic decay channel. Because of small background the distinction between different Υ states will be achievable.

The MTD detector will be placed 400 cm away from the interaction point on top of steel backlegs of the magnet. However, MTD trays are not installed on all 30 backlegs because it was required to leave a free space for operations on BEMC. On 3 backlegs there are only three MTD trays and on the rest there are 5, so in total MTD is composed of 117 trays. The time resolution is $< 100\text{ ps}$ and spatial resolution is $\sim 1\text{ cm}$. MTD uses the same electronics as TOF, namely LMRPC (Multi-gap Resistive Plate Chamber with Long Strips). MTD covers $\sim 40\%$ of azimuth and $|\eta| < 0,5$ [67].

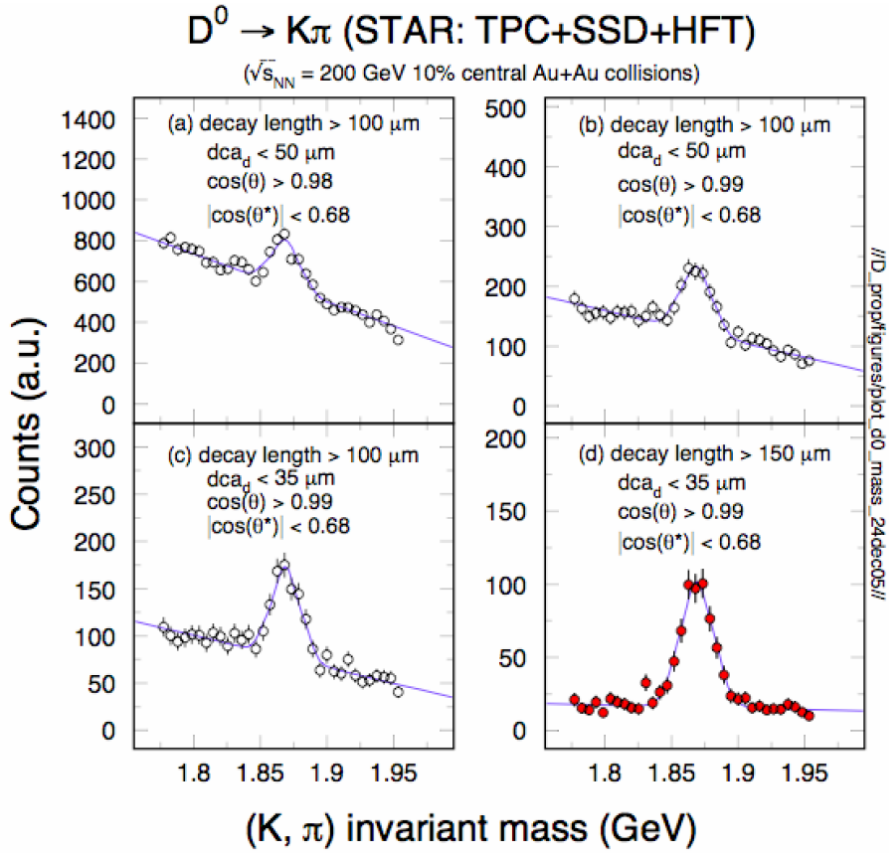


Figure 2.8: Reconstruction of D^0 meson signal with HFT included using simulated data. Various selection topological criteria are applied. Taken from Ref. [66].

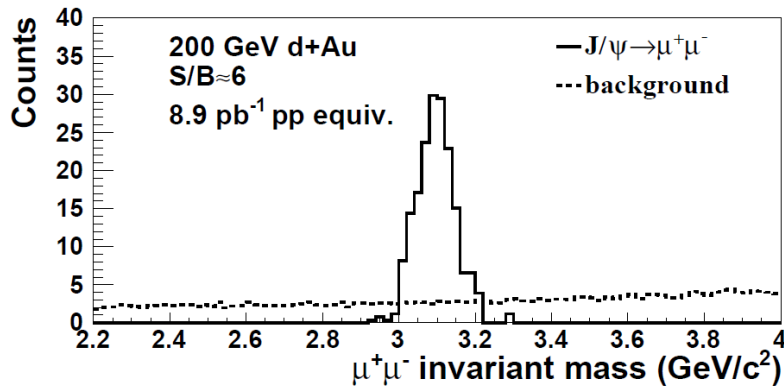


Figure 2.9: J/ψ signal as it would look like with MTD. Taken from Ref. [67].

Chapter 3

Analysis of non-photonic electrons

Electrons which originate mainly from semileptonic decays of open heavy flavor mesons, such as D and B , are called non-photonic electrons. This measurement is a good proxy for the study of energy loss processes of heavy quarks inside the quark-gluon plasma. In contrast to a p+p collision, the quark created in a heavy-ion collision have to pass through the strongly interacting medium which causes its energy loss via collisions with other partons or gluon radiation etc. A sensitive variable for such effects is the nuclear modification factor, which in case of the presence of QGP reveals a suppression pattern. In addition, the suppression in very central U+U collisions should be higher than in Au+Au central collisions. For this purpose, the analysis of NPE in 0-5% central U+U collisions is being performed and is described in detail in the following chapters.

The yield of non-photonic electrons is calculated according the formula 3.1

$$N_{npe} = N_{inc} * \epsilon_{purity} - N_{pho}/\epsilon_{pho}, \quad (3.1)$$

where the N_{inc} is the inclusive electron yield, N_{pho} is the photonic electron yield, ϵ_{purity} represents the purity of inclusive electrons and ϵ_{pho} is the photonic electron reconstruction efficiency. However, in this non-photonic electron yield there is contribution from decays of vector mesons, such as J/ψ . The final invariant yield of non-photonic electrons is calculated as

$$\frac{1}{2\pi p_T} \frac{d^2 N}{dp_T dy} = \frac{1}{2} \frac{1}{2\pi p_T} \frac{1}{\Delta p_T} \frac{1}{\Delta y} \frac{N_{npe}}{N_{events}} \frac{1}{\epsilon_{emc} \epsilon_{n\sigma_e} \epsilon_{rec}}, \quad (3.2)$$

where N_{events} is the number of events used for the analysis, ϵ_{emc} is the efficiency of the EMC cuts, $\epsilon_{n\sigma_e}$ is the efficiency of the $n\sigma_e$ cut and ϵ_{rec} is the efficiency of the single track reconstruction.

In the following sections, the calculation of each variable entering the above mentioned formulas will be discussed in detail. The data sample used for this analysis comes from U+U collisions at $\sqrt{s_{NN}} = 193$ GeV taken during the Year 2012 (run12) at the STAR experiment. After the measurement of collisions of particle beams the data sample consists of raw information from the detector readout. This data sample is then reconstructed and stored in the so-called muDst, which contains useful physical information about the tracks. The aim of an analysis is to further process the muDst files on large STAR computer farms and select only information needed for the specific type of analysis and save them in ROOT trees in form of picoDst. These data are eventually combined and the final results are obtained. This process can take up to several weeks.

The available data sample from uranium collisions contains minimum bias collisions, 0-1% and 0-5% central collisions. For the analysis described in this work only the 0-5% centrality events are selected because we would like to observe higher suppression in U+U

than in Au+Au collisions. Going to higher centrality events would be even more convenient, however, there is not enough statistics in this data sample. The *protected central 0-5%* collisions were selected by applying the following central5 triggers according the internal STAR notation: 400102, 400122, 400132, 400142. Protected events are corrected for effects of the pile-up. This phenomenon occurs when there is small window between the readout of tracks from different events thus, there is a contamination of particles coming from the previous event. The total number of events was 77M, from which 40M passed the event cuts described in the next section. In this analysis the TPC and BEMC detectors were used for particle identification, tracking and extraction of energy information.

3.1 Event and track quality cuts

In order to obtain a non-photonic electron sample, one has to first select the inclusive electron sample using various cuts which are going to be described below. Event cuts are used in order to select only events with vertices at the center of the detector so that the particles created in hadronization process are detected by the full detector acceptance. The position of vertices in the beam direction z has to be smaller than 30 cm from the center ($-V_z \leq 30$ cm) and the difference between the vertex reconstruction from TPC and VPD ($V_z^{VPD} - V_z^{TPC}$) has to be smaller than 3 cm. Figure 3.1 shows that the majority of events are situated at the center of STAR. The green lines represent the event cuts. After these selection criteria the amount of data sample used for the analysis of non-photonic electrons is ≈ 40 M events.

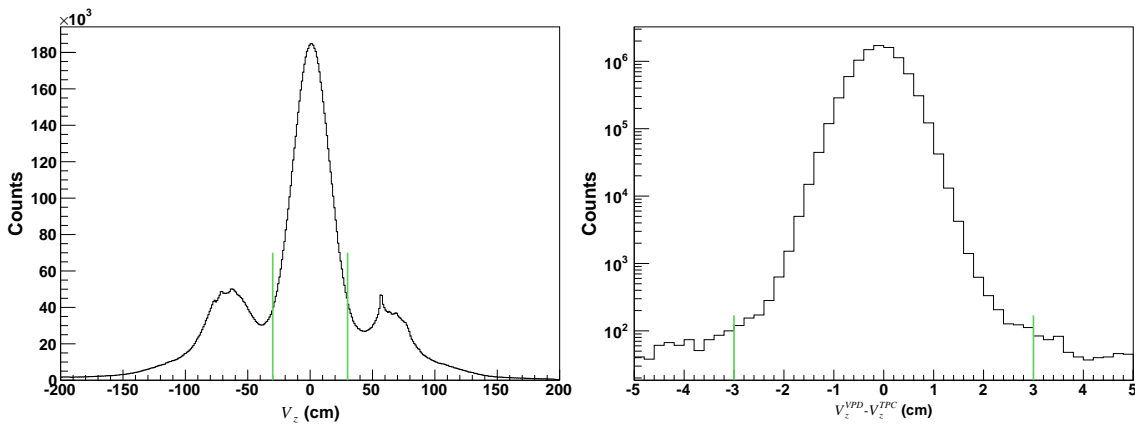


Figure 3.1: Left: Distribution of the position of event vertex in the beam direction. Right: Distribution of the difference between the vertex position reconstructed via the TPC and VPD. Green lines represent the event cuts.

After the event selection, the track quality cuts are applied on the so-called primary tracks. They are defined as primary because at the time of fitting the TPC points, also the collision vertex is included (that is, we force the track to originate in collision vertex). On the other hand the so-called global tracks are obtained by fitting the TPC points without the event vertex included. This different fitting procedures thus cause differences in the momentum of a track. The primary tracks are sufficient for e.g. analysis of J/ψ as the decay electrons are expected to originate at collision vertex. In the analysis of NPE the global variables are important because many tracks from photonic electron background can be created at different part of the detector far away from the collision vertex.

The tracking is done using the TPC detector. Tracks are reconstructed on the basis of fitting the points that are created by gas ionization in the TPC chamber. There is a

maximum number of track points in TPC due to finite number of the readout cathodes and anodes as was described in the second chapter. The track is required to have $n\text{Hits} \geq 20$ so that the fit would be of high quality. Another cut on the ratio of fitted points to the maximum number of points $n\text{Hits}/n\text{PossHits} > 0.52$ is applied. This is to avoid the double counting of one trajectory: sometimes the trajectory points can be splitted and read out as two different trajectories which leads to small $n\text{Hits}/n\text{PossHits}$ ratio. Another cut on the so called number of dE/dx hits in TPC was used. Not all points that are used to fit the trajectory of a particle have ideal signal and for that reason not all TPC points are used for the calculation of particle's energy loss. The applied cut is thus $d\text{EdxHits} \geq 15$.

The tracks have to originate in the same event vertex (the so called primary tracks) and for this reason a cut on the distance of the closest approach (DCA) of the track to the vertex is used. As the vertex is obtained by track extrapolation, they don't need to end up directly at one point. However, those that indeed originate in the vertex should be at least close to it. Therefore, the applied cut is $|DCA| < 1.5$ cm.

The pseudorapidity of tracks has to be $|\eta| < 0.7$ in order to make sure to use the full detector acceptance. The last track quality cut is applied on the first track point in TPC detector in the transverse direction. As non-photonic electrons will originate almost directly at the collision point, tracks that are created in the gas chamber mostly due to γ conversions have to be removed. The applied cut is $\text{firstPoint} < 73$ cm.

In this analysis we want to focus on high p_T region as the suppression pattern is visible at these transverse momenta. The cut applied is therefore $p_T > 1.2$ GeV/ c . Because the tracks are selected using this p_T cut, there is no need of usage of ToF detector, as its ability to separate electrons from hadrons decreases (see for instance Fig. 2.5).

The above mentioned cuts together with other described later on are summarized in Tab. 3.1.

3.2 Electron identification cuts

The cuts described above were used for a quality assurance of all tracks created in a collision. Several cuts are needed in order to identify the electron tracks, e.g. the cut on specific ionization energy loss in the TPC. The normalized energy loss is defined as

$$n\sigma_e = \frac{\ln \frac{\langle dE/dx \rangle^{mea}}{dE/dx^{th}}}{\sigma_{dE/dx}}, \quad (3.3)$$

where the indices ‘‘mea’’ and ‘‘th’’ mean measured and theoretical values, respectively. $\sigma_{dE/dx}$ is the experimental resolution. $n\sigma_e$ distribution of electron should have a Gaussian pattern centered around 0. However, the cut used in this analysis is $-0.5 < n\sigma_e < 2.5$ in order to suppress the contamination from pion tracks at negative values as can be seen in Fig. 3.2. The electron entries are almost not visible in comparison to the large presence of pions at negative $n\sigma_e$. In this plot all event, primary track and electron identification cuts (described below) were applied except the $n\sigma_e$ cut in order to demonstrate the large hadron contamination.

For the rest of the electron identification cuts the BEMC detector is used. A clustering algorithm was applied to group together 4 towers of the BEMC which are closest to the tower that was actually fired by an electron. This group of towers is called a BEMC point. The energy of the fired tower and position of SMD detectors in z and φ direction are extracted from each BEMC point. Then, the particle track is projected towards the BEMC and the respective positions of SMDs are obtained. The cuts which are going to be described below were determined using the pure electron sample, which can be

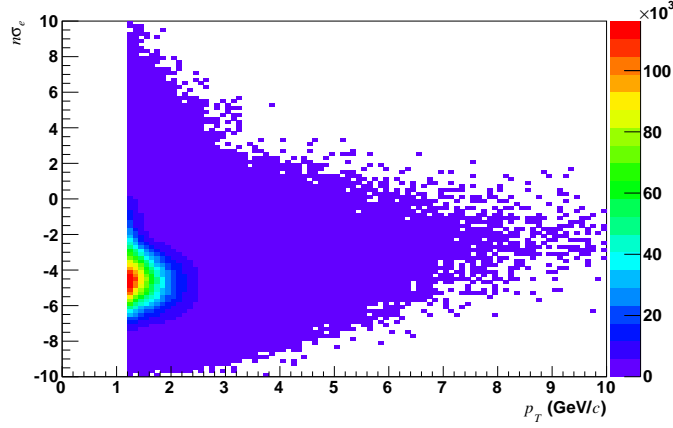


Figure 3.2: Distribution of $n\sigma_e$ of inclusive electrons as a function of p_T . All event, primary track and electron identification cuts were applied except the $n\sigma_e$ cut.

accomplished by the reconstruction of photonic electrons. The procedure of the photonic electron pairs selection is described in the following section 3.3.

First electron identification cut using the information from the BEMC detector is the ratio of the electron momentum and energy. Electrons are stopped in the BEMC, thus they deposit all of their energy in the detector. Their mass is negligible in comparison with their high momentum, therefore the ratio of their momentum and total energy should be equal to one. However, the cut used in this analysis is applied on the ratio p/E_0 , where E_0 is the energy of the most energetic tower from the BEMC point. Thus, the ratio has some distribution concentrated around one. The cut used in this analysis is therefore $0.3 < p/E_0 < 2$. In the Fig. 3.3 the p/E_0 distribution at one p_T bin is shown which was used for the determination of electron identification cuts. The entries of the unlike-likesign distribution (which is the pure electron distribution) are within the boundaries of the cut highlighted by the green lines.

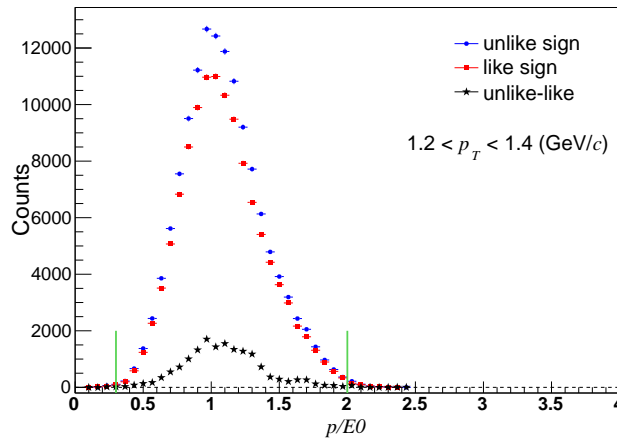


Figure 3.3: Distribution of the ratio p/E_0 for unlike sign electron pairs (blue dots), like sign electron pairs (red dots) and the unlike-like sign pairs (black stars) at one p_T bin. The plots at other p_T bins can be found in the Appendix.

The Shower Maximum Detectors are distributed in η (or z) and φ direction and are denoted as SMDE and SMDP, respectively. It is required that each track has to have

1 or more hits in both SMD detectors. Moreover, cuts on the difference between the projected SMD detector and actually fired SMD in both directions are applied. As the SMDE has good resolution only along the η direction and the SMDP only along the azimuthal direction, the cuts require a given maximum distance between the projected and fired SMDE in the η direction and SMDP in the φ direction, namely $|\Delta_Z| < 0.3$ cm and $|\Delta_\varphi| < 0.015$ rad. In the Fig. 3.4 the distributions of Δ_Z and Δ_φ of electron tracks are shown in one p_T bin. Again, the entries from pure electron sample are within the boundaries of the cuts marked with green lines.

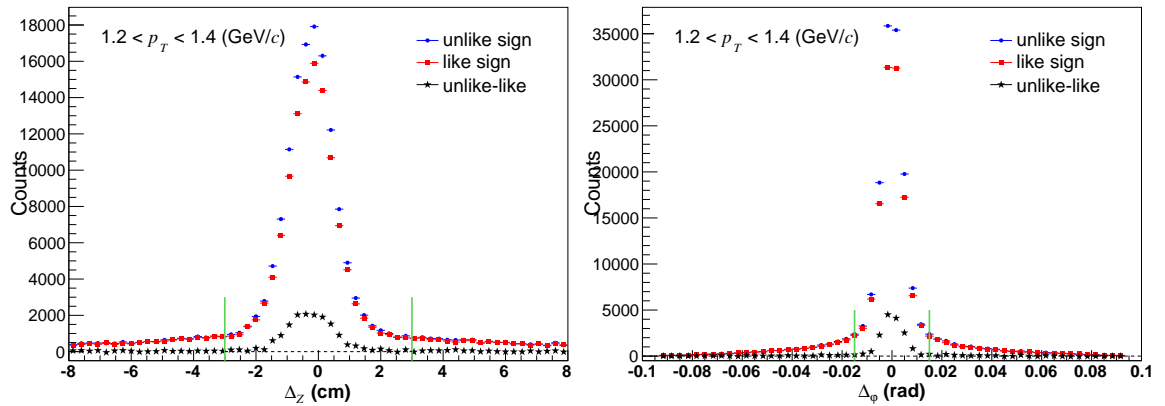


Figure 3.4: Distributions of difference between the projected SMDE(P) and actually fired SMD in η and φ direction for unlike sign electron pairs (blue dots), like sign electron pairs (red dots) and the unlike-like sign pairs (black stars). The plots at other p_T bins can be found in the Appendix.

3.3 Determination of photonic background

The measurement of non-photonic electrons is accompanied by large background which mainly comes from the so-called photonic electrons. These are created in pairs with opposite signs: $e^+ + e^-$ and primarily comes from photon conversions $\gamma \rightarrow e^+e^-$ or Dalitz decays $\pi^0(\eta) \rightarrow e^+e^-\gamma$.

After selecting the inclusive electron sample which was described above, the electron tracks are grouped together in pairs in the following way. Every primary track which already passed the cuts described in previous sections is combined with every global track. The global tracks have to be also sorted so that only electrons participate on pairing. The global track selection criteria are the following: $p_T > 0.2$ GeV/c, $n\text{Hits} \geq 20$, $\frac{n\text{Hits}}{n\text{PossHits}} > 0.52$ and finally $|n\sigma_e| < 3$.

Each pair then has to pass a set of cuts called pair cuts. First, the distance of closest approach of the pair tracks has to be smaller than 1 cm, $|p\text{DCA}| < 1$ cm, because the background electrons are always created in pairs in one point. Second, the cut on invariant mass of the electron pairs $m_{ee} < 0.24$ GeV/c² was applied. This should cover maximal mass which e^+e^- pair can have: from massless γ up to electrons from Dalitz decays of π or η . All electrons from γ conversions and from Dalitz decays are contained within this cut. In the Fig. 3.5 the invariant mass distribution of electron pairs is plotted for pairs with the same sign (like-sign) and opposite sign (unlike-sign). Photonic electrons are always created with opposite charges. The like-sign distribution should therefore describe the combinatorial background. After subtracting the like-sign pairs from unlike-sign pairs,

pure photonic electron sample remains. This can be verified by looking at the unlike-like sign distribution. Only at very low m_{ee} there are entries and towards higher m_{ee} there are only fluctuations around zero.

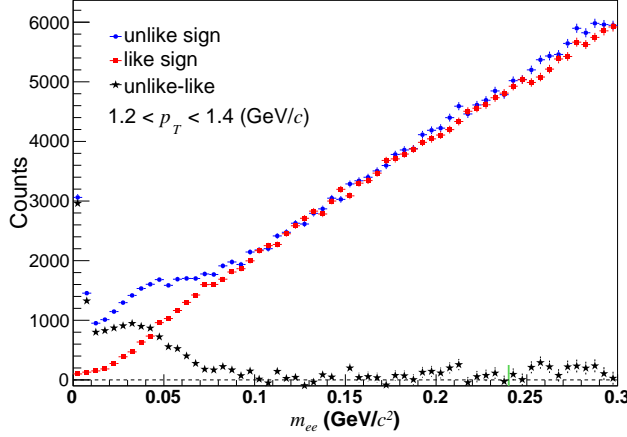


Figure 3.5: Distribution of invariant mass for unlike sign electron pairs (blue dots), like sign electron pairs (red dots) and the unlike-like sign pairs (black stars). The plots at other p_T bins can be found in the Appendix.

Another way of checking the pure electron sample is to plot the $n\sigma_e$ distribution of the global partner track of a pair for unlike sign, like sign and unlike-like sign pairs. After all electron identification cuts the unlike-like sign distribution should follow a perfect Gaussian. In the Figure 3.6 the $n\sigma_e$ distribution of global partner electron track is plotted in one p_T bin. The unlike-like distributions are fitted with a Gaussian function. As can be seen from the parameters of the fit, the unlike-like distribution follows a Gaussian shape very well, although the mean is shifted towards negative numbers, which is caused by bad calibration.

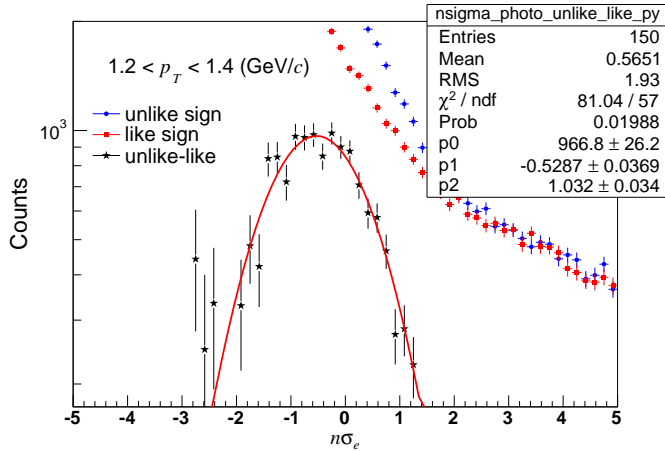


Figure 3.6: Distribution of $n\sigma_e$ of the global partner track for unlike sign electron pairs (blue dots), like sign electron pairs (red dots) and the unlike-like sign pairs (black stars) at one p_T bin. The plots at other p_T bins can be found in the Appendix.

3.4 Summary of selection criteria applied in NPE analysis

In the Tab. 3.1 there is a summary of all cuts which have been applied in the analysis of non-photonic electrons in 0-5% central U+U collisions at $\sqrt{s_{NN}} = 193$ GeV.

SELECTION CRITERIA	DESCRIPTION OF THE CRITERIA
Event cuts	
$ V_z < 30$ cm	Position of event vertex in the beam direction
$ V_z^{TPC} - V_z^{VPD} < 3$ cm	Difference between position of event vertex reconstructed in TPC and VPD
DCA < 1.5 cm	Distance of closest approach of a track to the collision vertex.
Track cuts	
nHits ≥ 20	Number of hits in TPC gas
$\frac{nHits}{nPossHits} > 0.52$	Ratio of hits in TPC to maximum possible hits
dEdxHits ≥ 15	Number of hits in TPC used for the calculation of energy loss dE/dx
$p_T > 1.2$ GeV/c	Transverse momentum of particles
$ \eta < 0.7$	Selection of midrapidity region in terms of pseudorapidity
firstPoint < 73 cm	First detected track point in TPC in trasverse direction
Electron identification cuts	
$ \Delta_z < 3$ cm	Difference between associated and actually fired SMDE in the beam direction
$ \Delta_\varphi < 0.015$ rad	Difference between associated and actually fired SMDP in azimuthal direction
$0.3 < p/E_0 < 2$	Ratio of particle's momentum and energy of the most energetic tower from the EMC cluster
$-0.5 < n\sigma_e < 2.5$	Normalized energy loss of electron
nSMDE > 1	Number of fired SMDE
nSMDP > 1	Number of fired SMDP
Global Partner Cuts	
$p_T > 0.2$ GeV/c	Transverse momentum of global partner tracks
$ n\sigma_e < 3$	Normalized energy loss of global partner track
nHits ≥ 20	Number of hits in TPC of global partner track
$\frac{nHits}{nPossHits} > 0.52$	Ratio of hits in TPC to maximum possible hits of global partner tracks
Pair cuts	
$ pDCA < 1$ cm	Distance of closest approach of electron pairs
$m_{ee} < 0.24$ GeV/c ²	Invariant mass of electron pairs

Table 3.1: Summary of selection criteria applied in the analysis of non-photonic electrons in 0-5% central U+U collisions at $\sqrt{s_{NN}} = 193$ GeV.

Using the above mentioned cuts a raw p_T spectrum of the inclusive electron sample and the photonic electron sample can be drawn. The histogram can be found in the Fig. 3.7. The data in this histogram are just summed yields of electrons and their antiparticles, positrons. The amount of signal at $p_T \gtrsim 4$ GeV/c is decreasing, especially the one of photonic electrons. At $p_T > 6$ GeV/c the abundance of inclusive and photonic electrons

is not sufficient to perform analysis. Therefore, the corrections on the raw spectra and the final spectra of non-photonic electrons are studied only up to $p_T = 6 \text{ GeV}/c$, which is going to be described in the following sections.

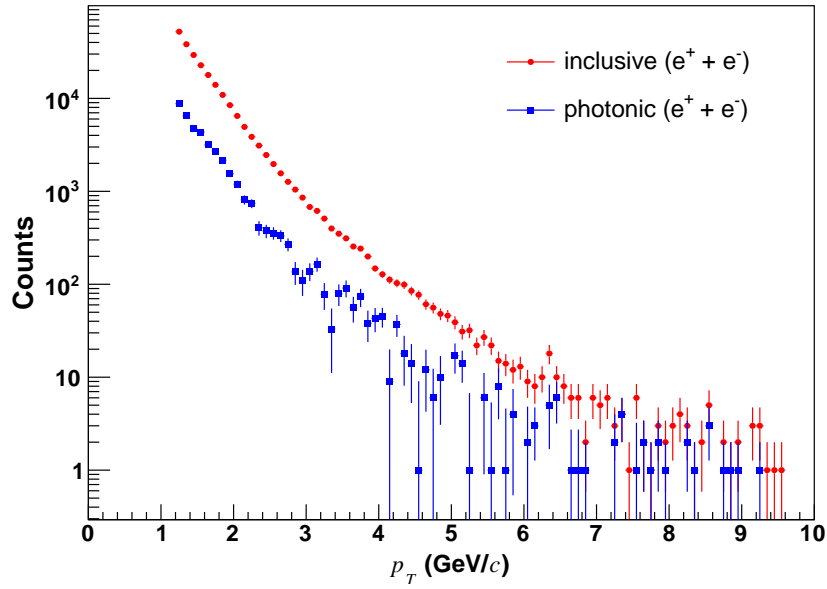


Figure 3.7: Raw p_T spectrum of the inclusive and photonic electron sample.

Chapter 4

Reconstruction efficiencies and detector acceptance

Even after the application of all above mentioned cuts, the data sample does not contain all non-photonic electrons created in the collision, or some tracks are still not correctly identified as electrons. It is not possible to reject all hadron contamination of the electron sample, as can be seen for example in the $n\sigma_e$ distributions of primary electron tracks (Figure 4.1), where there is a large π contamination. It is important to consider the exact value of cut on $n\sigma_e$: whether we cut on $|n\sigma_e| < 3$ with many π tracks included, or we cut $-0.5 < n\sigma_e < 2.5$ and then lose many of real electron tracks. Once the cut is selected, the efficiencies of the applied cuts are needed to be calculated and subsequently correct the spectra by using them. The efficiency is in general defined as the ratio of yield with given cut to the yield without the cut.

4.1 Efficiency of $n\sigma_e$ cut of single electron tracks

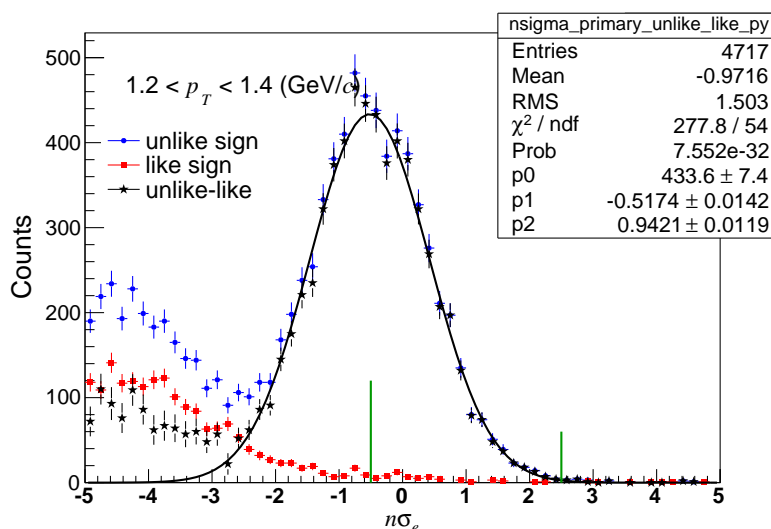


Figure 4.1: Distribution of $n\sigma_e$ of primary electron track from photonic electron pairs for unlike sign (blue dots), like sign electron pairs (red dots) and the unlike-like sign pairs (black stars) for one p_T bin. The green lines represent the $n\sigma_e$ cut. The plots at other p_T bins can be found in the Appendix.

In order to calculate the efficiency of the $n\sigma_e$ cut, the inclusive electron yield with all cuts except the $n\sigma_e$ cut has to be obtained. However, the $n\sigma_e$ cut is very important for the selection of electron tracks. As in the efficiency study one wants to be sure that the obtained electron sample is still pure, much tighter cuts on invariant mass and $n\sigma_e$ of global tracks are applied: $m_{ee} < 0.01 \text{ GeV}/c^2$, $-1 < n\sigma_e(\text{global}) < 3$. In order to check the pure electron sample the distribution of $n\sigma_e$ of electron primary tracks is shown in the Fig. 4.1. These distributions are obtained without the $n\sigma_e$ cut on primary tracks and with the above mentioned tighter cuts. It can be seen that the above mentioned applied cuts resulted in almost pure electron sample, as the $n\sigma_e$ distribution is well described by a Gaussian function.

Finally, the $n\sigma_e$ efficiency can be calculated as the ratio of electron yield with all cuts including the tight invariant mass and $n\sigma_e$ of global track and with the $n\sigma_e$ of primary track cut to the electron yield without the cut on $n\sigma_e$ of primary track. Or, we can say that it is the ratio of integral under the Gaussian fit of $n\sigma_e$ within the green lines in Fig. 4.1 to integral under the whole Gaussian. The result is shown in the Fig. 4.2. The efficiency is about 0.5, which is consistent as the $n\sigma_e$ cut rejects almost a half of the Gaussian. The efficiency is fitted with a constant function and also with a polynomial of first order. The polynomial fit was used further in the analysis. The resulting dependence of the $n\sigma_e$ efficiency on p_T is similar to other analyses done at Au+Au collisions at similar energies.

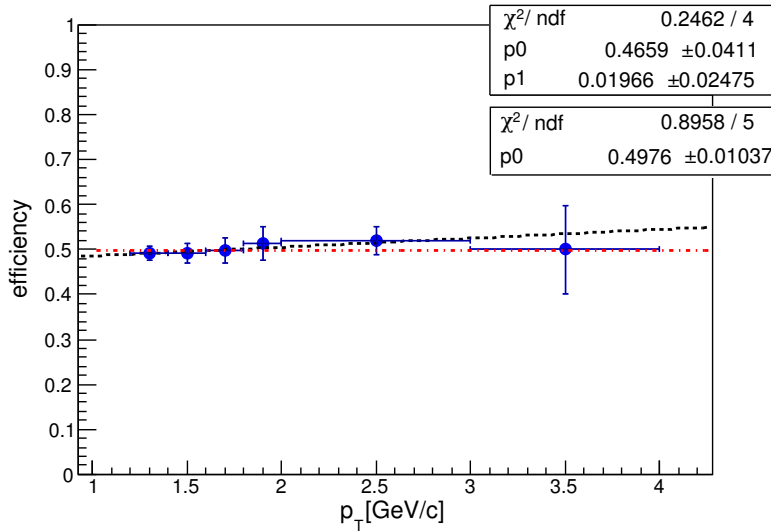


Figure 4.2: $n\sigma_e$ efficiency as a function of p_T . The efficiency is fitted with a constant function and polynomial of first order.

4.2 Efficiency of single electron cuts using BEMC

The EMC efficiency is a summary notation for efficiency of all cuts using the BEMC detector, which are the following: $|\Delta_Z| < 3 \text{ cm}$, $|\Delta_\varphi| < 0.015 \text{ rad}$, $0.3 < p/E_0 < 2$, $n\text{SMDE} > 1$ and $n\text{SMDP} > 1$. Again, a check of purity of the electron sample has to be done because without the EMC cuts a large hadron contamination is present. This is done via the study of a Gaussian distribution of the $n\sigma_e$ of global tracks from photonic electron pairs. Tighter cut on the invariant mass is used ($m_{ee} < 0.01 \text{ GeV}/c^2$) in order to assure for the purity of electron sample used for the efficiency calculation. In the Fig. 4.3 can be seen that the distribution of $n\sigma_e$ of global tracks follows the Gaussian distribution

with the EMC cuts included or not.

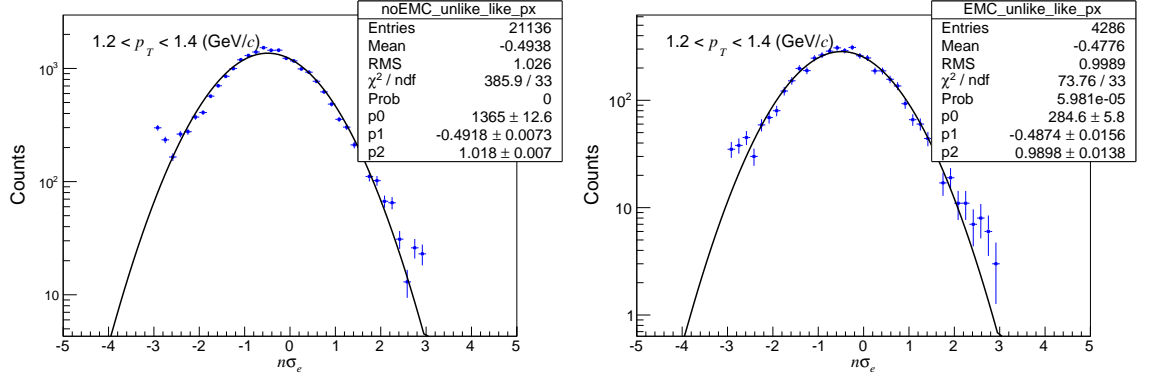


Figure 4.3: Distribution of $n\sigma_e$ of global electron tracks from the photonic pairs at one p_T bin without the EMC cuts (left) and after the EMC cuts (right). The plots at other p_T bins can be found in the Appendix.

The EMC efficiency is calculated as ratio of the electron yield with all cuts including the tight invariant mass cut and the EMC cuts to the electron yield without the EMC cuts. The EMC acceptance is implicitly included in the calculation: as the tracks in the numerator passed the cuts using the EMC, it means they were reconstructed in the EMC. The distribution of the efficiency of EMC cuts can be found in the Fig. 4.4. At low p_T the efficiency has values of ~ 0.2 and it rises towards ~ 0.6 at higher p_T . The efficiency is fitted with a polynomial function of second order.

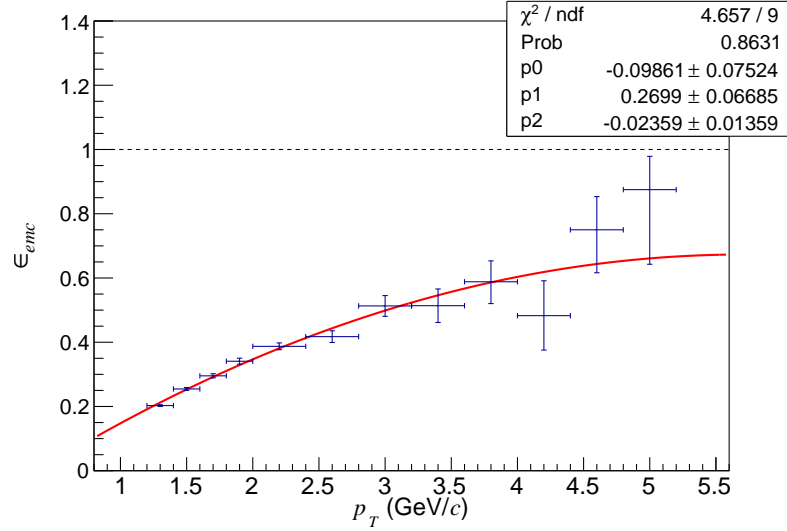


Figure 4.4: EMC efficiency as a function of p_T . The distribution is fitted with a polynomial function of second order.

4.3 Purity

The fraction of real electrons in the selected inclusive electron sample is called the purity of the sample. Even after the application of all electron identification cuts there is still some hadron contamination in the electron sample, as can be inferred from the $n\sigma_e$ distribution

of electrons in Fig. 4.1: at negative values there are still entries from mostly pions which results in a small deviation of data points from the Gaussian function. Looking at the distribution of dE/dx in Fig. 2.3 it can be seen that pion band cross the electron one which makes the hadron subtraction difficult.

The distribution of normalized energy loss of inclusive electrons without the $n\sigma_e$ cut at different p_T bins is used for the calculation of purity efficiency. At higher p_T range which is used in this analysis, the electron band of the energy loss is hardly distinguishable from other particles because they overlap. Therefore, the $n\sigma_e$ distribution is fitted with 4-Gaussian function (3-Gaussian at high p_T). The means and widths of individual Gaussians for $p+K$ and π are obtained from theoretical Bichsel functions and used as initial input fit parameters. The mean of electron Gaussian should be equal to zero and the width equal to one. However, these parameters are shifted from expected values due to bad calibration in the TPC detector. Therefore, one has to obtain these prior to 4-Gaussian fitting.

The same $n\sigma_e$ distribution of primary electron tracks from photonic electron pairs (pure electron sample) used for the calculation of $n\sigma_e$ efficiency (Fig. 4.1) is used for the determination of mean and width of the electron Gaussian. The distributions are fitted with a Gaussian function at different p_T bins. The resulting means and widths are shown in the Fig. 4.5. The mean is shifted towards negative values and the width is around one. The result is used for initial definition of the parameters of 4-Gaussian fit of $n\sigma_e$ distribution of the inclusive electron sample.

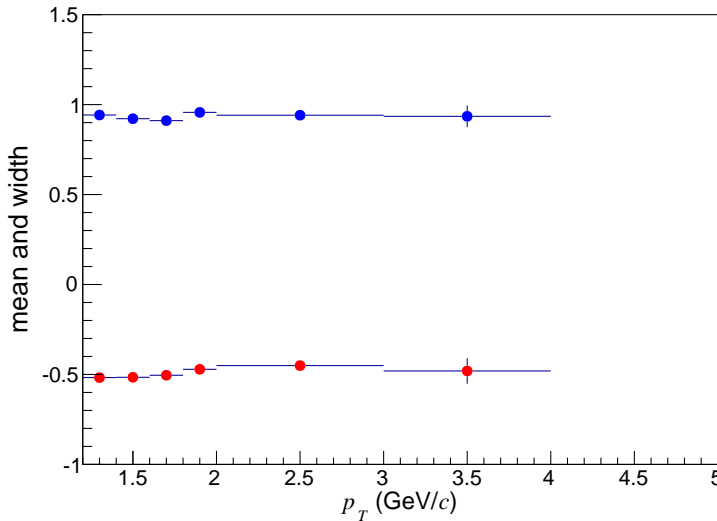


Figure 4.5: Mean and width of the $n\sigma_e$ distribution of primary electrons of the pure photonic electron sample.

In the Fig. 4.6 the $n\sigma_e$ distribution of inclusive electrons is plotted at one p_T bin and fitted with 4-Gaussian function. The same procedure is done at different p_T bins and at $p_T > 3$ GeV/c the 3-Gaussian function is used. The entries at positive values of $n\sigma_e$ at low p_T are the so called merged pions and are denoted with the green line. These are just mistakenly interpreted two tracks as one. The protons and kaons are fitted with one Gaussian, as their bands of energy loss are almost on top of each other. The fit function is marked with magenta color. Pions are marked with blue and finally electrons with red color. The purity is then calculated as ratio of the integral between the boundaries of $n\sigma_e$ cut under the electron Gaussian to the integral under the multi-Gaussian fit.

The hadron contamination in the inclusive electron sample is very large, as can be

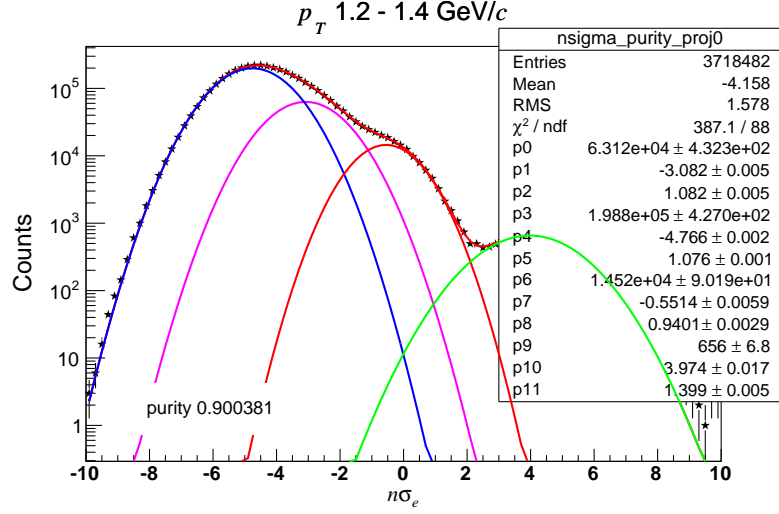


Figure 4.6: The $n\sigma_e$ distribution of inclusive electrons at one p_T bin fitted with 4-Gaussian function. The magenta line represents $K + p$, the blue line stands for π , red for electrons and finally the green line are merged pions. The plots at other p_T bins can be found in the Appendix.

seen in the Fig. 4.6. Therefore, the 4-Gaussian fit meets with obstacles especially at the p_T range where the Gaussians of π , K and p are crossing each other. At each p_T bin the mean and width of π , K , p and e is extracted from multi-Gaussian fit of $n\sigma_e$ distribution of inclusive electrons and plotted in Fig. 4.7. It is clear, especially when one looks at the width distribution, that there is difficulty to properly describe hadrons while the electron fit parameters yields satisfactory values. In order to improve the fitting and consequently the purity results, the further studies of means and widths of π , K and p are also needed. This will be the subject of future work on the analysis of non-photonic electrons.

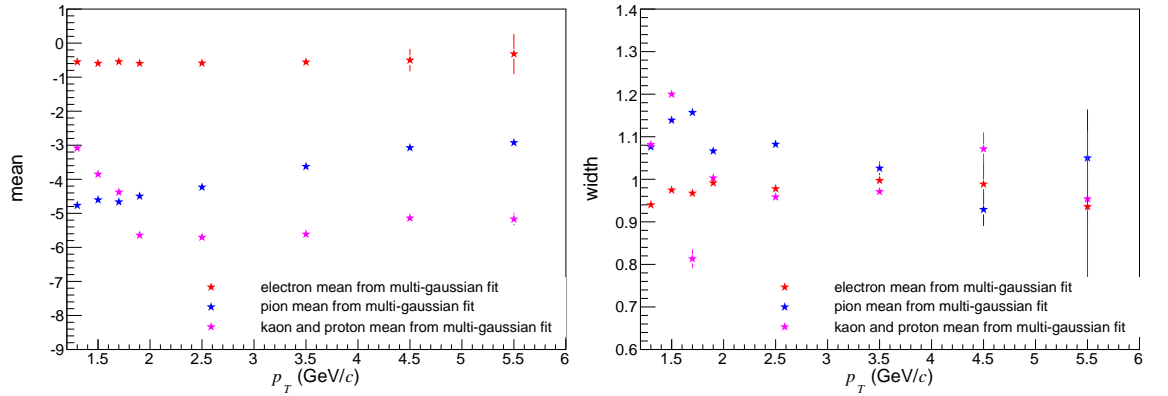


Figure 4.7: Distributions of means and widths of π , K , p and e extracted from multi-Gaussian fit of $n\sigma_e$ distribution of inclusive electrons at each p_T bin.

In order to estimate the systematical uncertainty of purity, the $n\sigma_e$ distributions are fitted again, but this time with different constraints put on the electron Gaussian. The mean or width of the Gaussian is allowed to vary by 1σ or 2σ deviation. The purity was calculated at each fit. This procedure is shown in the Fig. 4.8 at one p_T bin. In the Fig. 4.9 (left) the obtained purities at each fit and p_T bin are shown. There is almost no difference between the fits with different constraints and points are therefore plotted on

top of each other. The final purity is then calculated as the mean of purities obtained at each p_T bin from different fits and the systematical error is the largest difference between the mean value and one of the four values at each p_T bin. The final result can be seen in the Fig. 4.9 (right).

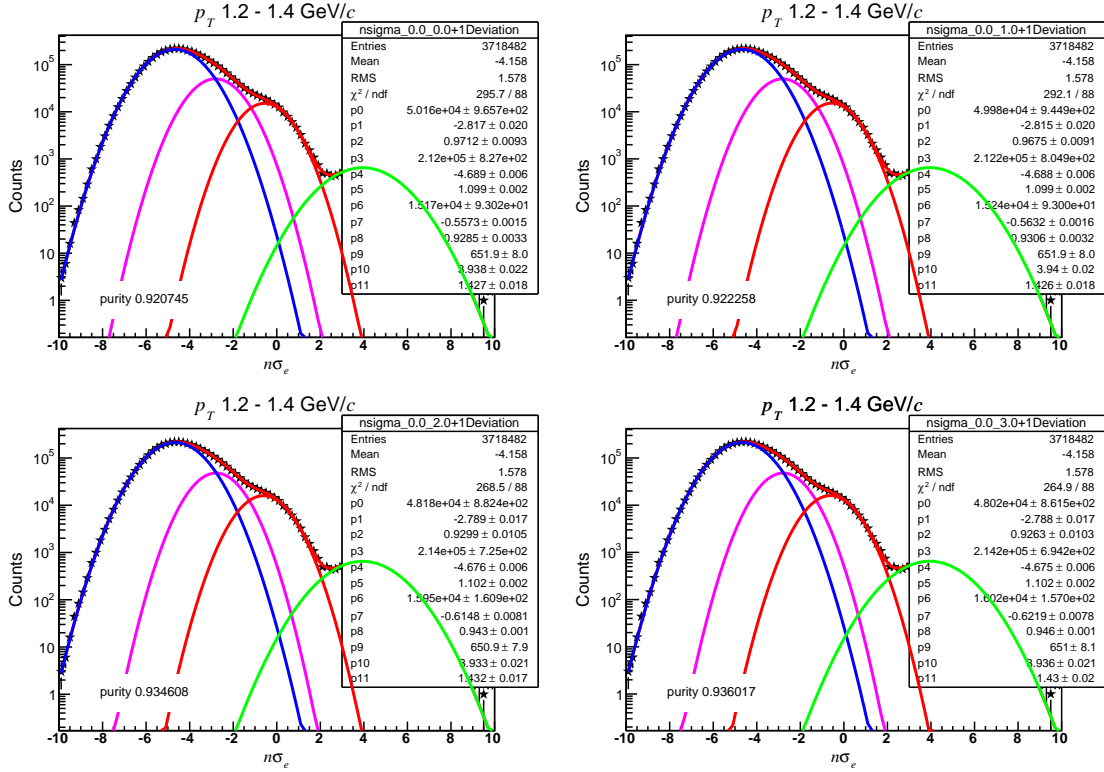


Figure 4.8: The $n\sigma_e$ distributions of inclusive electrons at different p_T bins. The distributions are fitted with different constraints on electron Gaussian. The plots at other p_T bins can be found in the Appendix.

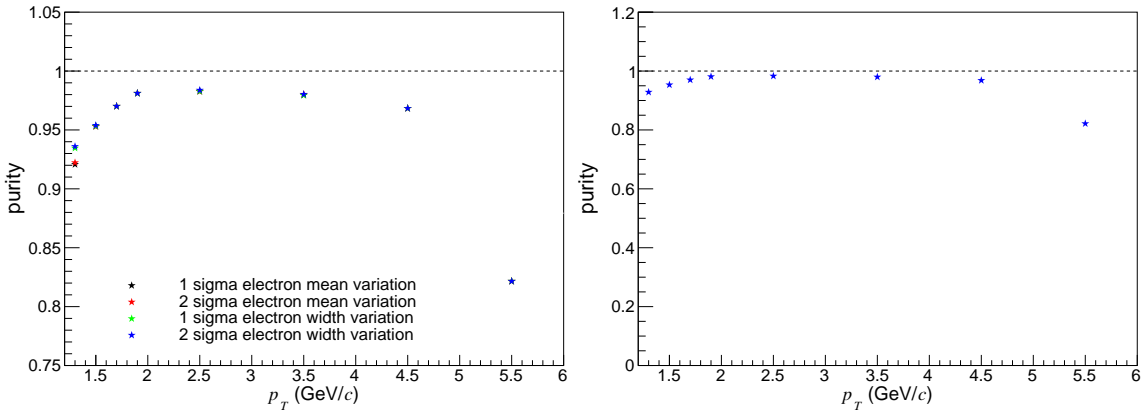


Figure 4.9: Left: The purity vs. p_T distribution from fits with different constraints. Right: The final purity vs. p_T distribution.

4.4 Photonic electron reconstruction efficiency

The last two efficiencies which are going to be discussed in this chapter are calculated from the embedding data. The detector cannot reconstruct all the electron pairs that are produced in conversion of γ and Dalitz decays. This inefficiency has to be corrected. For that purpose the full simulation of STAR detector may be used. Monte Carlo simulated tracks are embedded into a real collision and propagated through the detector using GEANT. Then the detector response to each particle is simulated. These simulations are then mixed with real detector readout at raw data level and reconstructed using the same reconstruction chain used in real data reconstruction. The output are trees with informations about simulated tracks (MC tracks) and the reconstructed tracks. One then has to run over the MC track entries and find appropriate track partner from trees of reconstructed tracks and apply the same cuts which are used in the real data analysis in order to calculate desired efficiencies. Reconstructed tracks are associated with MC tracks if they have more than 20 common TPC hits.

The photonic electron reconstruction efficiency is the efficiency of global and pair cuts applied on global partner tracks and electron pairs. It is defined as the ratio of tracks which passed all the cuts to the primary tracks whose global partners do not obey the global and pair cuts. It can be expressed with the formula 4.1. The cuts mentioned in this section are listed in the Tab. 3.1.

$$\epsilon_{pho} = \frac{\text{track, electron identification, global partner and pair cuts}}{\text{track and electron identification cuts}} \quad (4.1)$$

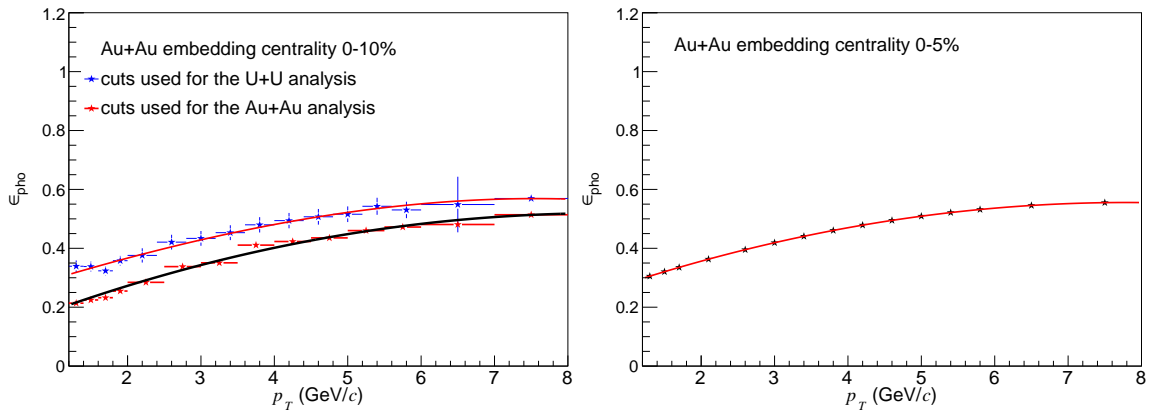


Figure 4.10: Left: The comparison of distributions of photonic electron reconstruction efficiency at 0-10% centrality calculated using the selection criteria used in Au+Au and U+U analysis. Right: The extrapolated distribution of photonic electron reconstruction efficiency towards 0-5% centrality.

For this analysis of NPE in U+U collisions the Au+Au embedding was used because the U+U embedding was not available yet. It is not expected that there will be large difference between the embedding from U+U and Au+Au collisions. The ROOT trees from Au+Au embedding were taken from previous analysis of Au+Au collisions data. As the selection criteria in Au+Au analysis are different from U+U analysis, the calculation of efficiencies was done with cuts used in this analysis. The difference can be seen in the Fig. 4.10 (left), where the photonic electron reconstruction efficiency in 0-10% centrality is shown with different selection criteria. The result obtained by using the cut applied in the analysis of U+U collisions is higher than Au+Au collisions. The difference is mainly

caused by the difference in the cut on p_T of global partner track. While in the analysis of U+U collisions $p_T(\text{global}) > 0.2 \text{ GeV}/c$, in the analysis of Au+Au collisions this cut is $p_T(\text{global}) > 0.3 \text{ GeV}/c$. This comparison was done as a cross check.

Information for 0-5% centrality was not available for Au+Au embedding, so extrapolation to 0-5% was done. First, efficiency versus centrality was plotted at each p_T bin and extrapolated towards 0-5% centrality. Then, the result of the extrapolation at each p_T bin was obtained and final ϵ_{pho} distribution plotted in Fig. 4.10 (right).

4.5 Single track reconstruction efficiency

The correction for the reconstruction efficiency of single tracks and the TPC detector acceptance calculation is described in this section. The efficiency of the single electron tracks is calculated using the embedding data and in the same manner as other efficiencies described above: it is defined as the ratio of tracks which passed the track cuts to all tracks generated in a collision within the pseudorapidity acceptance which is used in this analysis: $|\eta| < 0.7$. The track cuts are the following: $\text{DCA} < 1.5 \text{ cm}$, $\text{nHits} \geq 20$, $\frac{\text{nHits}}{\text{nPossHits}} > 0.52$, $\text{dEdxHits} \geq 15$, $\text{firstPoint} < 73 \text{ cm}$. The cut on p_T of the track is not included in the efficiency calculation in order to obtain a full curve starting at $p_T = 0 \text{ GeV}/c$. The omission of this cut will not affect the final efficiency distribution because it just select tracks with a given p_T . On the other hand, the rest of the cuts will have influence on the reconstruction efficiency because by applying cut on e.g. nHits, we loose some tracks with bad reconstruction in the TPC which would otherwise be used for the analysis.

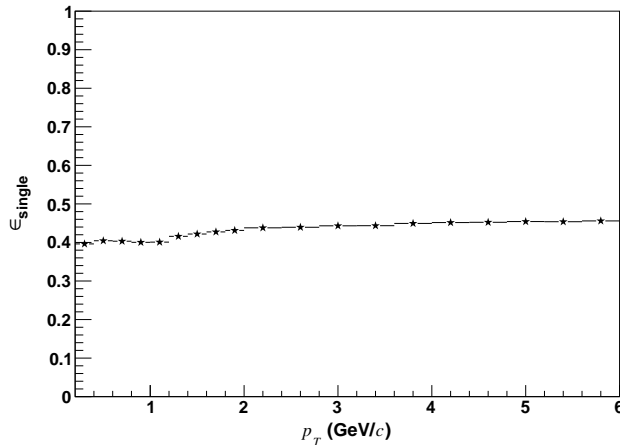


Figure 4.11: The distribution of single track reconstruction efficiency obtained from Au+Au embedding.

The acceptance of the TPC is included in the calculation of single track reconstruction efficiency as it can be correlated with the track cuts. The acceptance describes how many of all tracks created in the collision actually enter the TPC. Some of them can have too small energy to reach the TPC or can go in the direction of dead zones between the sectors of TPC. The acceptance can be expressed in the form of a ratio of tracks which enter the TPC to all tracks created in a collision. This, expressed in terms of the Monte Carlo variables of simulated tracks from embedding, is the ratio of MC tracks which were reconstructed by the detector, to all tracks generated in MC simulation within the $|\eta| < 0.7$.

Again, the Au+Au embedding was used for the calculation of single track reconstruction efficiency. The information for 0-5% data were included in the trees so no extrapola-

tion was needed. The result is plotted in the Fig. 4.11. The value of ~ 0.4 is similar to that from similar analyses in STAR experiment.

Chapter 5

Non-photonic electrons

The yield of non-photonic electrons can be calculated using the formula 3.1. We would like to note that all results presented in this thesis related to the U+U collisions were discussed in STAR collaboration but has not been yet approved for public use as preliminary results.

The data and the correction efficiencies were discussed in the previous sections. The raw spectra of non-photonic electrons are plotted in the Fig. 5.1 together with the photonic electron spectra which are divided by the photonic electron reconstruction efficiency ϵ_{pho} . The bin normalization was not done at this point, as later at the time of calculation of invariant yield of NPE the normalization is taken into account. It can be seen that at low p_T up to 2 GeV/ c the background represented by the photonic electron sample dominates. At higher p_T the number of NPE is higher than the background, but there is still high contamination from the conversion electrons or Dalitz decays.

This phenomenon can be seen clearer in the Fig. 5.2, where the ratio of non-photonic electrons to background is plotted. The ratio is below 1 at low p_T and slightly increases at higher p_T . The ratio is also compared to the preliminary data from Au+Au collisions at the energy $\sqrt{s_{NN}} = 200$ GeV, which were provided by Daniel Kikola after private communication. The background in U+U collisions is more significant than in Au+Au collisions as can be inferred from the fact that the ratio from U+U collisions is smaller, especially at transverse momentum range of $3.5 < p_T < 5.0$ GeV/ c . The ratio of NPE/PHE is dependent on detector setup. Material close to the collision point may result in larger conversion probability and then to large photonic yield. The setup of the detector at Au+Au data from Year 2010 and U+U data from Year 2012 is similar. Therefore, similar NPE/PHE ratio is expected. The values of the ratio are the same for both collisions at lower p_T . At high p_T there seems to be larger background from photonic electrons in U+U collisions. This deviation is expected to be covered by the ϵ_{pho} obtained from U+U embedding.

The invariant yield of non-photonic electrons is obtained according the formula 3.2. In the previous sections the procedures for calculation of the variables which enter the formula were described. The resulting yield of NPE can be found in the Fig. 5.3. The statistical uncertainties marked with vertical error bars come from the statistical errors of non-photonic electron spectra N_{npe} . Contribution to systematic uncertainties plotted as the blue boxes will be discussed in the next section. Clearly, two data points at $p_T = 4.6$ GeV/ c and $p_T = 5.4$ GeV/ c deviate from the overall p_T -dependence of U+U NPE yield. This difference is not covered by the errors and needs to be studied further.

5.1 Systematic uncertainties

Systematic uncertainties of yield of NPE have several sources. First, there is contribution from the estimation of photonic electron reconstruction efficiency. In this analysis the

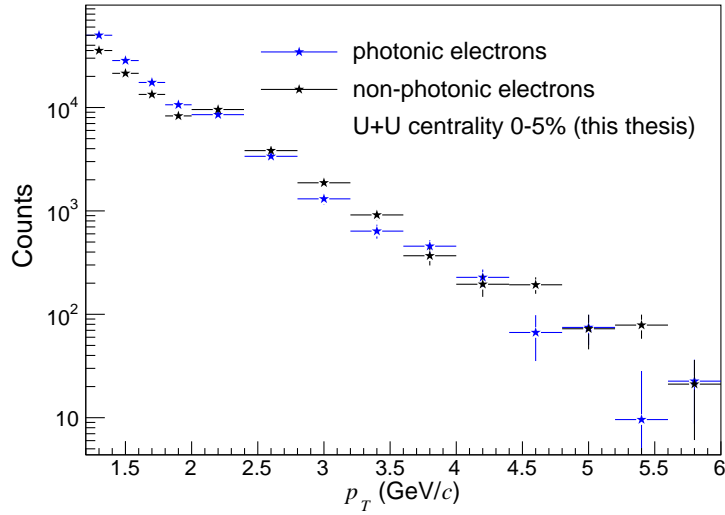


Figure 5.1: Spectra of non-photonic electrons together with photonic electrons.

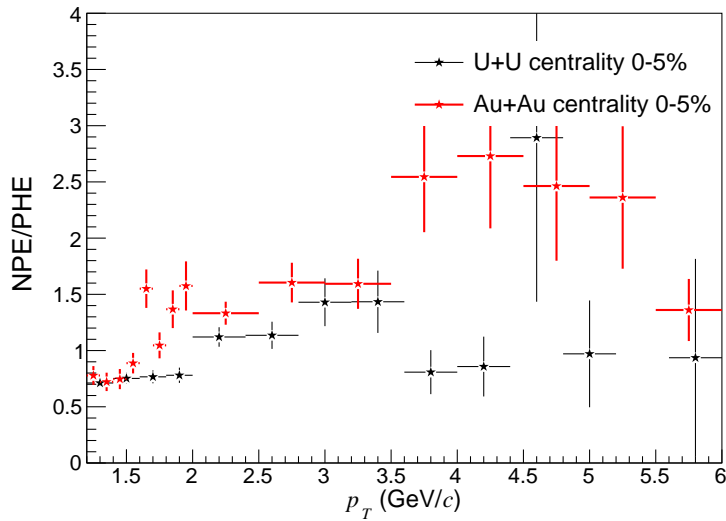


Figure 5.2: Ratio of non-photonic electrons to photonic electrons compared to preliminary results from Au+Au collisions at the same centrality class.

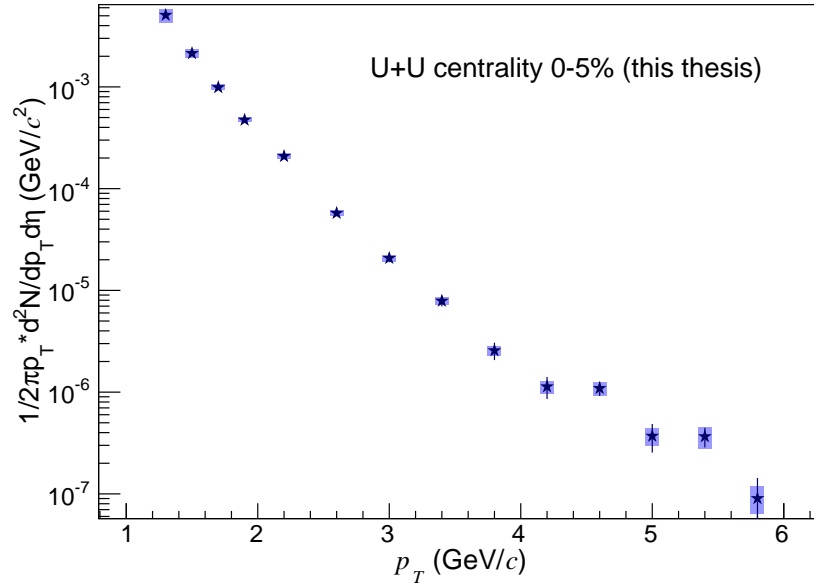


Figure 5.3: Invariant yield of NPE. Statistical uncertainties are drawn with vertical error bars and systematical uncertainties with the blue boxes.

embedding data from Au+Au collisions were used. The provided trees did not contain information about 0-5% centrality needed for this analysis, thus an extrapolation was made. Studies of systematic uncertainty of ϵ_{pho} was not yet made in detail, but a raw estimate can be made based on errors at 0-10% centrality. The relative uncertainty varies from 5-6%. As an extrapolation was made which also brings some discrepancies, a raw estimate of 10% can be made. However, this uncertainty will not be used in the final calculation of systematics as it is just a raw estimate and U+U embedding will be done soon where more precise systematic study will be performed.

Another contributions to systematics come from purity estimation, calculation of efficiencies of EMC, $n\sigma_e$ cuts and single track reconstruction efficiency. Final distributions of these efficiencies were shown in previous sections. In order to obtain systematics, these distributions are fitted with polynomial functions and confidence intervals of these fits are then extracted, as shown in Fig. 5.4. Systematic error from purity is then recalculated as systematic error of N_{npe} .

First, the contributions to systematical errors of NPE yield from each efficiency were calculated. The final systematics were obtained by adding the uncertainties of each contribution in quadratures. The relative contributions to systematics, as well as the total relative uncertainty, is summarized in the Tab. 5.1 and shown in the Fig. 5.5. The N_{npe} represents systematics which comes from the purity, ϵ_{emc} , $\epsilon_{n\sigma_e}$ and ϵ_{rec} are the systematics obtained from the fits of distributions of these efficiencies.

The highest contribution to the systematical error of the yield comes from the efficiency of EMC cuts. On the other hand, the single track reconstruction efficiency has a very small impact on the systematics. The total systematic uncertainty varies from 5 to 30 %.

5.2 Nuclear modification factor

The nuclear modification factor R_{AA} was already defined above: it is the ratio of particle production in heavy-ion collisions to proton-proton collisions scaled by the mean number

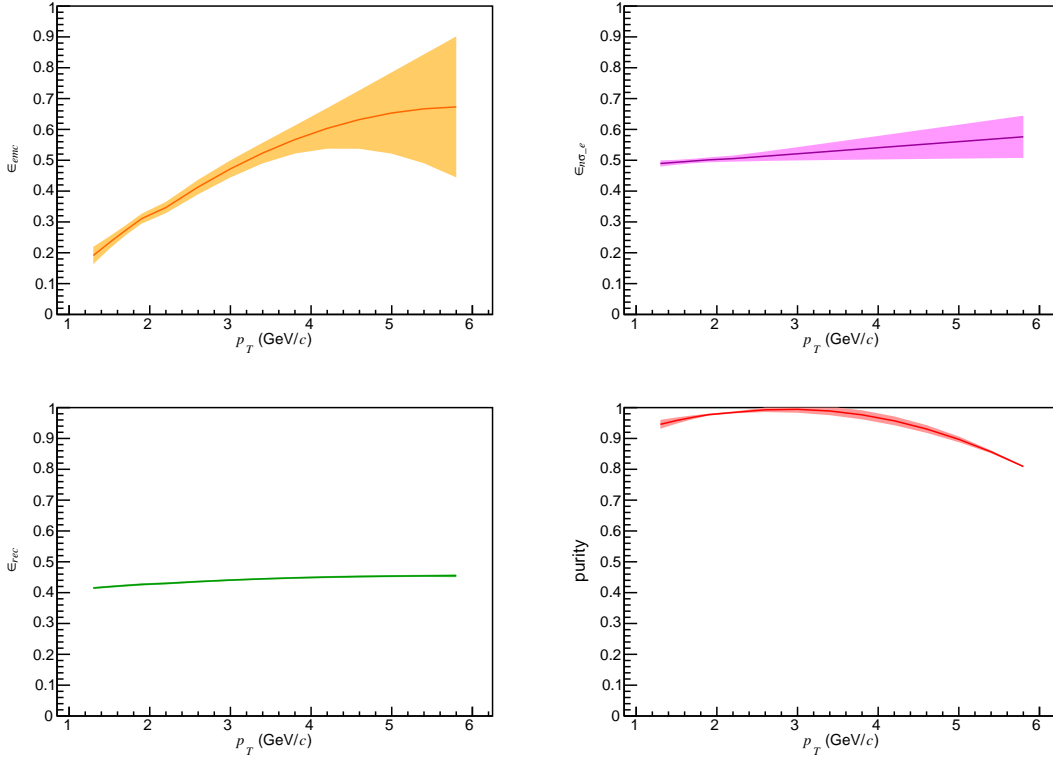


Figure 5.4: Plots of fit results of efficiencies which contribute to the overall systematic uncertainty of NPE yield. The line represents the fit and the colored bands the confidence intervals. On the upper left pad there is ϵ_{emc} , upper right $\epsilon_{n\sigma_e}$, bottom left ϵ_{rec} and on the bottom right pad there is fit of purity distribution.

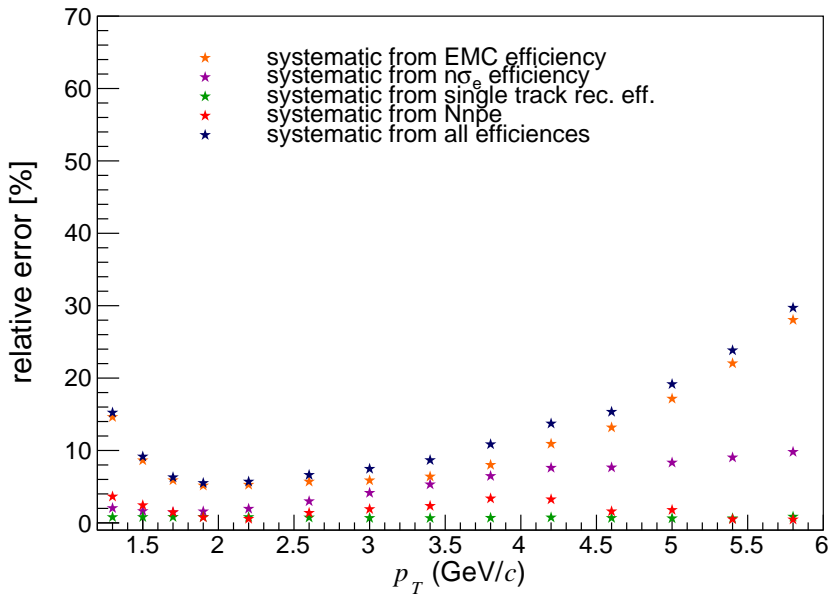


Figure 5.5: Relative systematical uncertainty of the invariant yield of NPE. The relative contributions of each source is shown, as well as the total relative error.

p_T (GeV/ c)	source			
	N_{npe}	ϵ_{emc}	$\epsilon_{n\sigma_e}$	ϵ_{rec}
1.2 - 1.4	3.64 %	14.62 %	2.04 %	0.79 %
1.4 - 1.6	2.44 %	8.64 %	1.63 %	0.80 %
1.6 - 1.8	1.48 %	5.90 %	1.45 %	0.81 %
1.8 - 2.0	1.76 %	5.15 %	1.58 %	0.81 %
2.0 - 2.4	0.56 %	5.27 %	1.95 %	0.80 %
2.4 - 2.8	1.38 %	5.70 %	2.99 %	0.74 %
2.8 - 3.2	1.90 %	5.87 %	4.14 %	0.68 %
3.2 - 3.6	2.34 %	6.40 %	5.32 %	0.66 %
3.6 - 4.0	3.37 %	8.01 %	6.47 %	0.70 %
4.0 - 4.4	3.25 %	10.92 %	7.61 %	0.75 %
4.4 - 4.8	1.59 %	13.18 %	7.66 %	0.67 %
4.8 - 5.2	1.78 %	17.16 %	8.33 %	0.63 %
5.2 - 5.6	1.50 %	22.04 %	9.04 %	0.62 %
5.6 - 6.0	0.47 %	28.03 %	9.80 %	0.85 %

Table 5.1: Relative contributions to systematic uncertainties of the yield of NPE. More details can be found in the text.

of binary collisions. The reference for the calculation of the R_{AA} was taken from p+p collisions at the energy $\sqrt{s} = 200$ GeV from Year 2009 [68]. The invariant cross section was fitted by the power-law function 5.1. The spectra together with the fit are shown in Fig. 5.6.

$$[p0] * (e^{-[p1]*x - [p2]*x^2} + x/[p3])^{-[p4]} \quad (5.1)$$

The mean number of binary collisions $\langle N_{bin} \rangle$ in uranium collisions were estimated from Glauber model for the centrality 0-5%, taken from Ref. [69]. The final value used for the calculation of nuclear modification factor was taken as $\langle N_{bin} \rangle = 1341 \pm 105$.

The R_{AA} of non-photonic electrons in 0-5% central U+U collisions at the energy $\sqrt{s_{NN}} = 193$ GeV is shown in the Fig. 5.7. The statistical uncertainties are propagated from statistical errors of the yield of NPE from U+U collisions. The systematical uncertainties coming from systematics of the yield from U+U collisions are represented by the blue boxes. The errors caused by fitting the p+p reference are shown as white boxes.

The nuclear modification factor of NPE in U+U collisions is also compared to the preliminary results from Au+Au collisions. The statistical uncertainties seem to have the same magnitude as those from Au+Au data. In order to cross-check this statement the relative statistical errors from both collisions are plotted as a function of p_T in Fig. 5.8 where almost no difference is observed.

On the other hand, the difference between relative systematical errors of R_{AA} from U+U and Au+Au collisions is apparent, especially at low and intermediate p_T . Uncertainties in U+U collisions are much lower than in Au+Au collisions. However, this is a preliminary estimation of systematic uncertainties in U+U collisions where systematic error from photonic electron reconstruction efficiency was not included.

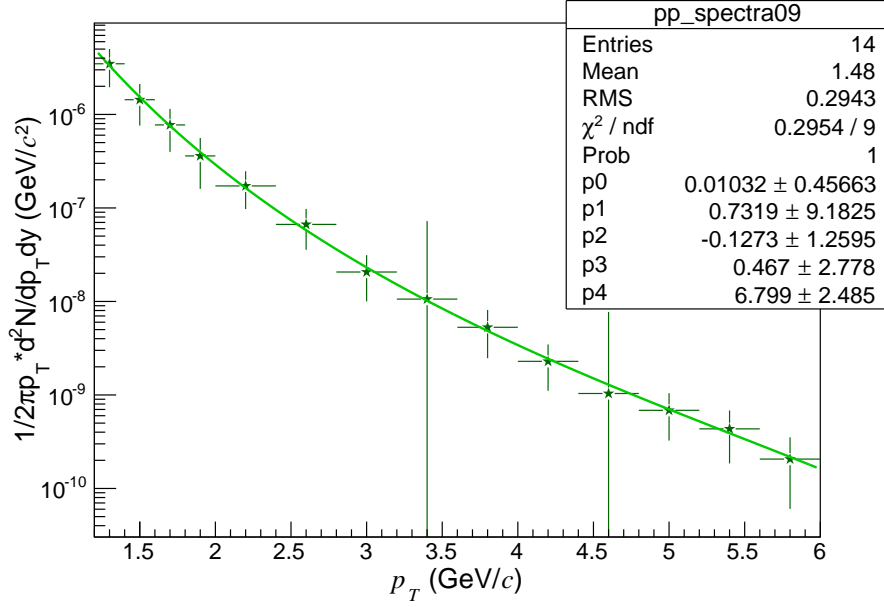


Figure 5.6: Spectra of non-photonic electrons in p+p collisions at $\sqrt{s} = 200$ GeV fitted with power-law function [68].

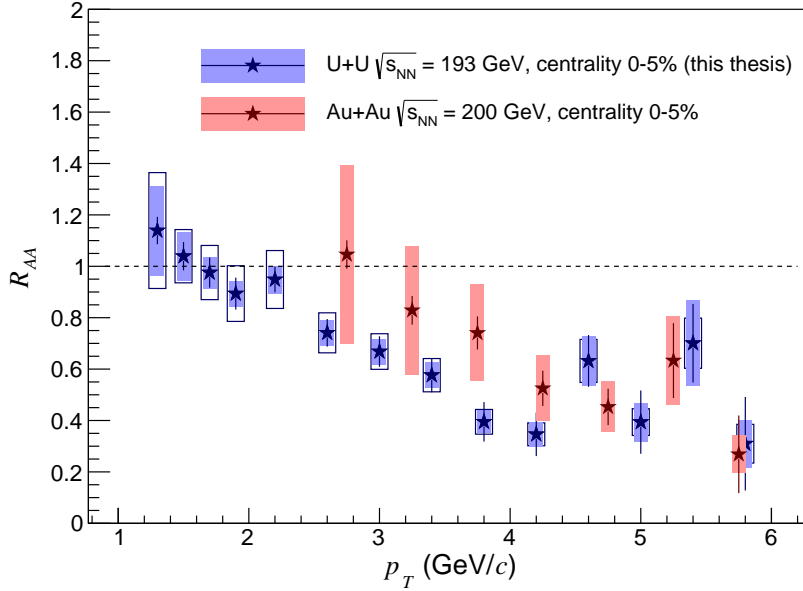


Figure 5.7: Nuclear modification factor of non-photonic electrons in 0-5% central U+U collisions at $\sqrt{s_{NN}} = 193$ GeV compared to the preliminary results from Au+Au collisions at $\sqrt{s_{NN}} = 200$ GeV. The error bars represent the statistical errors, the blue boxes represent the systematical error of the uranium invariant yield of NPE and the systematics from the baseline fit are plotted as white boxes.

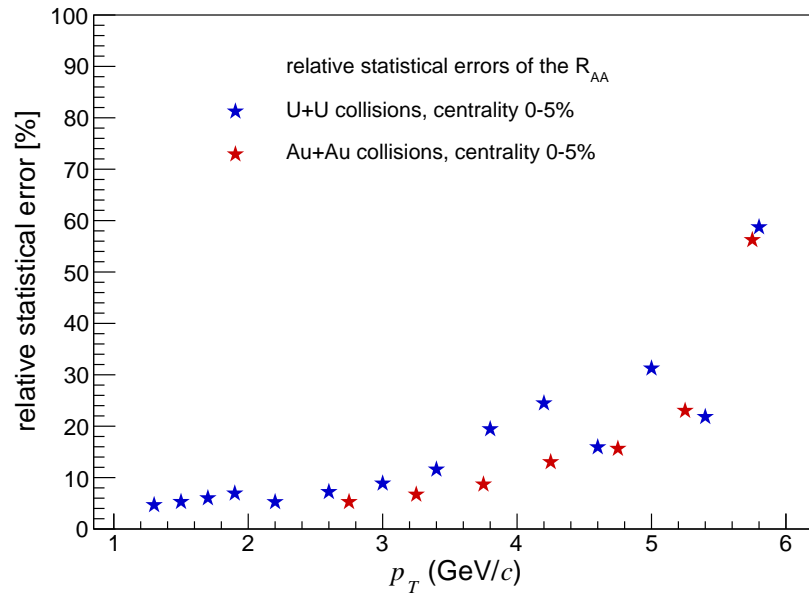


Figure 5.8: Relative statistical uncertainties of the nuclear modification factor of NPE in both U+U and Au+Au collisions at the energy $\sqrt{s_{NN}} = 193$ and 200 GeV, respectively.

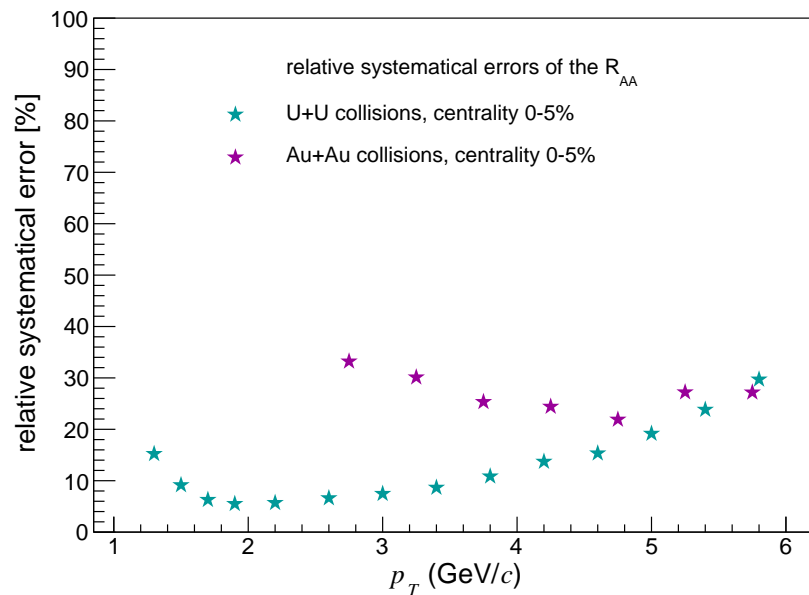


Figure 5.9: Relative systematical uncertainties of the nuclear modification factor of NPE in both U+U and Au+Au collisions at the energy $\sqrt{s_{NN}} = 193$ and 200 GeV, respectively.

5.3 Statement about the author contribution

Results from U+U collisions presented in Chapter 3, 4 and Chapter 5 was original work of the author of this thesis. This included the extraction of raw electron yields, determination of correction factors, evaluation of systematical uncertainties and correction of the non-photonic electron spectra.

Chapter 6

Discussion of results

The main purpose of the analysis described in this work is to study most central U+U collisions in order to investigate the effect of higher energy density on suppression of heavy flavor particles. More detailed explanation is provided in the chapter 1.6. This analysis was performed within the transverse momentum range of $1.2 < p_T < 6.0$ GeV/ c and at midrapidity $\eta < |0.7|$.

First, the inclusive and photonic electrons were selected. The quality assurance plots of the cuts used for the selection show that the photonic electrons, that should contain a pure electron sample, are situated within the boundaries of the cuts. In these plots, photonic electrons are represented with unlike-like sign distribution. A double-check on the purity of the photonic electron yield was also performed. As can be seen from the plots of invariant mass and $n\sigma_e$ distributions of global electron tracks (Fig. 3.5 and 3.6, respectively), there is almost no contamination from other particles. The unlike-like sign entries in m_{ee} distributions are mainly grouped at low values which represent low invariant mass of γ conversion and Dalitz e^+e^- pairs. At higher m_{ee} the distribution just fluctuates around zero and within the statistical uncertainties it can be considered to be equal zero. The same fact reveals also the distribution of $n\sigma_e$ of global partner track of photonic electron pairs. The unlike-like sign points follow the shape of Gaussian function.

Next step was to calculate the efficiencies of cuts used in the analysis which are later used for the correction of invariant yield of NPE. The estimation of ϵ_{emc} and $\epsilon_{n\sigma_e}$ was done using the pure electron sample from data that is, unlike-like sign distributions. The statistics at $p_T > 4$ GeV/ c is rapidly decreasing what affected the estimation of efficiencies and consequently the systematic errors of NPE yield.

The detection efficiency of EMC cuts at low p_T is low due to its large distance from the collision vertex. Many electrons with low energy do not reach the calorimeter and thus their energy deposition cannot be measured; they are not reconstructed in BEMC. With increasing p_T the efficiency is rising and eventually saturates at the value ≈ 0.6 . On the other hand, the efficiency of $n\sigma_e$ cut is almost constant over the whole p_T range used in this analysis and approximately equal 0.5. This fact is not surprising as with the $-0.5 < n\sigma_e < 2.5$ cut half of the Gaussian is thrown away. Finally, the estimation of purity of inclusive electron sample was performed via fitting the $n\sigma_e$ distribution with a multi-Gaussian function. The purity is approaching unity in all p_T bins and the systematic error estimated from fits with different constraints is negligible. Despite of that, the multi-Gaussian fit does not evaluate the hadron widths reasonably well, especially at the crossing region of pions and kaons, as could be seen in Fig. 4.7 (right). Therefore, the calibration studies of the mean and width of hadrons should be done using the data, not the theoretical predictions from Bichsel functions.

Embedding from Au+Au collisions at $\sqrt{s_{NN}} = 200$ GeV was used to calculate the

photonic electron reconstruction efficiency ϵ_{phe} and detector acceptance ϵ_{rec} . As there were no embedding data saved at 0-5% centrality, the ϵ_{phe} was extrapolated towards this centrality class which could introduce some discrepancies. The plots of ϵ_{pho} versus centrality at each p_T bin at the time of extrapolation can result different if the same plot was performed as a function of reference multiplicity. As was explained in the theoretical introduction of this thesis, the multiplicity is used to define centrality classes. As gold nuclei are much smaller and have different shape than uranium nuclei, the multiplicity at given centrality could be different. This fact could then affect the extrapolation and subsequently the magnitude of suppression of NPE production.

The obtained spectra of non-photonic electrons suffer from large background represented by photonic electrons as can be seen in Fig. 5.1 or Fig. 5.2. The ratio of NPE to PHE expresses this statement even better. At low p_T the background dominates while at higher p_T the desired NPE sample is larger. However, it is still contaminated by electrons created in pairs, as the ratio does not differ much from unity. Compared to Au+Au collisions the ratio is smaller. This can be caused by the shape of the photonic electron reconstruction efficiency which can be lower than it is in reality. If the results from U+U embedding shows that the ϵ_{phe} is higher, the photonic electron background would be smaller which would result in higher NPE/PHE ratio.

Finally, the invariant yield of NPE was obtained, scaled by the mean number of binary collisions and divided by the reference data from p+p collisions in order to calculate the R_{AA} . The nuclear modification factor of NPE in U+U collisions was compared to Au+Au collisions. The centrality class is consistent with the one used in analysis of U+U collisions. As can be seen from the Fig. 5.7, the suppression in U+U collisions is slightly higher than that in Au+Au collisions. Higher suppression of heavy flavor particles is expected in very central U+U collisions in comparison to Au+Au collisions, as was explained in the first chapter of this thesis. However, one can be concerned about this result. Measurements of D mesons in 0-10% central U+U collisions reveal the same magnitude of suppression as Au+Au collisions. Thus, even if higher centrality events are selected (0-5%), one would not expect such a decrease of R_{AA} especially if the contribution from vector mesons, such as J/ψ , was not yet subtracted from the NPE invariant yield. The relative statistical errors are the same for both collisions. The systematics in U+U collisions are however smaller than in Au+Au. Nevertheless, the preliminary results are shown which does not take into account yet all sources of systematic uncertainties. Also, U+U embedding is needed in order to obtain final corrections, which may alter currently used efficiencies, especially the photonic electron reconstruction efficiency.

The largest impact on the systematical errors came from the efficiency of electron cuts using the BEMC detector. At high p_T the errors are rising, as could be seen from the Fig. 5.5, where relative systematic errors are shown as a function of p_T . However, possibly the error caused by the estimation and extrapolation of photonic electron reconstruction efficiency, which was not included in the calculation of total systematics, will have even larger influence and could enhance the systematics. The final production of embedding sample of U+U central 5% collisions will be available soon and the proper calculation of ϵ_{pho} and also ϵ_{rec} will be performed, which will give more accurate extraction of the R_{AA} .

Conclusions

The aim of this thesis was to present the theoretical background of the studies of hot and dense medium created in ultrarelativistic heavy-ion collisions, the quark-gluon plasma (QGP), as well as the detailed description of analysis of non-photonic electrons (NPE) in uranium-uranium collisions at $\sqrt{s_{NN}} = 193$ GeV at the STAR experiment.

Non-photonic electrons that originate in semileptonic decays of open heavy flavor mesons are a good proxy for the study of QGP and the mechanisms of energy loss of heavy quarks inside this medium. Recent STAR, PHENIX and ALICE results were shown and an attempt to introduce the need of the analysis performed and presented in this thesis was given.

First, the inclusive and photonic electrons were selected. The p_T distributions look reasonable, also the quality assurance plots of the cuts used in the analysis were shown which proved that the obtained photonic electron yield is not contaminated.

Efficiencies of the selection criteria and detection acceptancies were calculated in order to later correct the yield of non-photonic electrons. Due to small electron sample at high p_T the systematic errors which arise from the fit of efficiencies are large. Embedding data from Au+Au collisions were used in the studies of detector acceptance as U+U embedding has not yet been done. Embedding from Au+Au collisions is a good approximation however, the embedding made precisely for the data sample used in this analysis is needed for better precision.

Finally, the spectra of NPE and their invariant yield was obtained. In order to get the nuclear modification factor, data from p+p collisions from Year 2009 were taken as a baseline. The R_{AA} from U+U collisions was compared to Au+Au collisions results. Despite the expected difference in suppression at central U+U collisions, the results revealed almost similar suppression in U+U and Au+Au collisions. However, considering the uncertainties, the fact that the vector meson contribution has not yet been subtracted and the results from D meson analysis at 0-10% central U+U collisions, the R_{AA} from U+U collisions is lower than expected.

The analysis of NPE in 0-5% central U+U collisions at $\sqrt{s_{NN}} = 193$ GeV has not yet been finished. The future work will include more detailed study of systematic uncertainties, analyse the U+U embedding data as soon as they are ready, and finally estimate the contributions from vector meson decays to the electron spectra and subtract them.

Bibliography

- [1] K. A. Olive *et al.* (Particle Data Group), *Chin. Phys. C* **38**, 090001 (2014).
- [2] J. D. Bjorken, *Phys. Rev. D* **27**, 140 (1983).
- [3] A. Adare *et al.* (PHENIX Collaboration), *Phys. Rev. Lett.* **104**, 132301 (2010).
- [4] K. Adcox *et al.*, *Nucl. Phys. A* **757**, 184 (2005).
- [5] K. Yagi *et al.*, *Quark-Gluon Plasma*, Cambridge University Press 2005.
- [6] STAR Collaboration, *Studying the Phase Diagram of QCD Matter at RHIC*, <https://indico.bnl.gov/getFile.py/access?resId=0&materialId=2&confId=764> (2014).
- [7] Ch. Nattrass, *The Quark Gluon Plasma*, www.quantumdiaries.org. [online] [30. 3. 2015]
- [8] R. Stock, arXiv: 0807.1610v1[nucl-ex] (2008).
- [9] M. L. Miller, K. Reygers, S. J. Sanders, P. Steinberg, *Ann. Rev. Nucl. Part. Sci.* **57**, 205 (2007).
- [10] M. Kliemant, R. Sahoo, T. Schuster and R. Stock, *Lect. Notes Phys.* **785**, p. 23-103 (2010).
- [11] J. Adams *et al.* (STAR Collaboration), *Phys. Rev. Lett.* **91**, 072304 (2003).
- [12] David, *A smorgasboard of major experiment results*, www.ellipsix.net. [online] [30. 3. 2015]
- [13] Y.L. Dokshitzer and D.E. Kharzeev, *Phys. Lett.* **519**, 199 (2001).
- [14] B. Abelev *et al.* (ALICE Collaboration), *JHEP* **09**, 112 (2012).
- [15] W. Florkowski, *Phenomenology of Ultra-Relativistic Heavy-Ion Collisions*, World Scientific, 2010.
- [16] J. Adams *et al.* (STAR Collaboration), *Phys. Rev. Lett.* **92**, 052302 (2004).
- [17] D. Kikola, G. Odyniec and R. Vogt, *Phys. Rev. C* **84**, 054907 (2011).
- [18] H. Satz, *J. Phys. G32*:R25 (2006).
- [19] R. Vogt, *Ultrarelativistic Heavy-Ion Collisions*, Elsevier 2007.
- [20] S. Chatrchyan *et al.* (CMS Collaboration), *Phys. Rev. Lett.* **109**, 222301 (2012).

- [21] J. L. Nagle, A.D. Frawley, L.A. Linden Levy and M. G. Wysocki, Phys. Rev. C **84**, 044911 (2011).
- [22] C. Aidala *et al.* (PHENIX Collaboration), arXiv: 1404.1873 [nucl-ex] (2014).
- [23] A. Adare *et al.* (PHENIX Collaboration), Phys. Rev. C **90**, 034903 (2014).
- [24] L. Adamczyk *et al.* (STAR Collaboration), Phys. Rev. D **86**, 072013 (2012).
- [25] L. Adamczyk *et al.* (STAR Collaboration), Phys. Rev. Lett. **113**, 142301 (2014).
- [26] B. Abelev *et al.* (ALICE Collaboration), JHEP 1207, 191 (2012).
- [27] B. Abelev *et al.* (ALICE Collaboration), Phys. Lett. B **718**, 279 (2012).
- [28] B. Abelev *et al.* (ALICE Collaboration), JHEP 1209, 112 (2012).
- [29] H. Agakishiev *et al.* (STAR Collaboration), Phys. Rev. D **83** 052006 (2011).
- [30] A.D. Frawley, T. Ullrich and R. Vogt, Phys. Rept. 462:125-175 (2008).
- [31] A. Adare *et al.* (PHENIX Collaboration), Phys. Rev. Lett. **97**, 252002 (2006).
- [32] B. Abelev *et al.* (ALICE Collaboration), Phys. Rev. D **91**, 012001 (2015).
- [33] B. Abelev *et al.* (ALICE Collaboration), PLB **738**, 97 (2014).
- [34] B. Abelev *et al.* (ALICE Collaboration), Phys. Rev. D **86**, 112007 (2012).
- [35] B. Abelev *et al.* (ALICE Collaboration), Phys. Lett. B **721**, 13 (2013).
- [36] M. Cacciari, P. Nason and R. Vogt, Phys. Rev. Lett. **95**, 122001 (2005).
- [37] M. Aggarwal *et al.* [STAR Collaboration], Phys. Rev. Lett. **105**, 202301 (2010).
- [38] B. I. Abelev *et al.* (STAR Collaboration), Phys. Rev. Lett. **98**, 19301 (2007); Erratum-*ibid.* **106**, 159902 (2011).
- [39] A. Adare *et al.* (PHENIX Collaboration), Phys. Rev. C **86**, 024909 (2012) and references therein.
- [40] A. Adare *et al.* (PHENIX Collaboration), Phys. Rev. Lett. **98**, 172301 (2007) and references therein.
- [41] M. Djordjevic, M. Gyulassy, R. Vogt and S. Wicks, Phys. Lett. B **632**, 81 (2006).
- [42] M. He, R. J. Fries and R. Rapp, Phys. Rev. C **86**, 014903 (2012).
- [43] J. Uphoff, O.Fochler, Z. Xu and C. Greiner, Phys. Rev. C **84**, 024908 (2011).
- [44] J. Uphoff, O.Fochler, Z. Xu and C. Greiner, Phys. Lett. B **717**, 430 (2012).
- [45] R. Sharma, I. Vitev and B.-W. Zhang, Phys. Rev. C **80**, 054902 (2009).
- [46] W. Horowitz, AIP Conf. Proc. **1441**, 889-891 (2012).
- [47] P. Gossiaux and J. Aichelin, Phys. Rev. C **78**, 014904 (2008).
- [48] P. Gossiaux, J. Aichelin, T. Gousset and V. Guiho, J. Phys. G **37**, 094019 (2010).

- [49] N. Borghini, P. M. Dinh and J.-Y. Ollitrault, Phys.Rev. C **63**, 054906 (2001).
- [50] L. Adamczyk *et al.* (STAR Collaboration), arXiv: 1405.6348 [hep-ex] (2014).
- [51] M. Völkl for the ALICE Collaboration, arXiv: 1412.2670 [nucl-ex] (2014).
- [52] R. Maciula and A. Szczurek, Phys. Rev. D **87**, 094022 (2013).
- [53] A. Adare *et al.* (PHENIX Collaboration), arXiv: 1405.3301[nucl-ex] (2014).
- [54] L. Adamczyk *et al.* (STAR Collaboration), Phys. Lett. B **722** 55 (2013).
- [55] L. Adamczyk *et al.* (STAR Collaboration), Phys. Lett. B **735** 127 (2014).
- [56] M. Strickland, D. Bazow, Nucl.Phys. A **879**, 25 (2012).
- [57] A. Emercik, X. Zhao, R. Rapp, Eur. Phys. J. A **48**, 72 (2012).
- [58] STAR experiment, STAR notes <https://drupal.star.bnl.gov/STAR/starnotes/public>
- [59] N. Xu (STAR Collaboration), Nucl. Phys. A **931**, 1 (2014).
- [60] The STAR Time Projection Chamber: A Unique Tool for Studying High Multiplicity Events at RHIC http://www.star.bnl.gov/public/tpc/NimPapers/tpc/tpc_nim.pdf
- [61] Brookhaven National Laboratory, www.star.bnl.gov
- [62] W. R. Leo, *Techniques for Nuclear and Particle Physics Experiments: A How-To Approach*, Springer, 1994.
- [63] Proposal for a Large Area Time of Flight System for STAR, <https://www.star.bnl.gov/public/tof/>
- [64] The STAR Barrel Electromagnetic Calorimeter, http://www.star.bnl.gov/public/tpc/NimPapers/emc/emc_nim.pdf
- [65] W. J. Llope *et al.*, arXiv: 1403.6855 [physics.ins-det] (2014).
- [66] E. Anderssen *et al.*, A Heavy Flavor Tracker for STAR: <http://www.osti.gov/scitech/servlets/purl/939892>.
- [67] L. Ruan *et al.*, STAR Muon Telescope Detector Proposal: http://www.star.bnl.gov/~ruanlj/MTDreview2010/MTD_proposal_v14.pdf.
- [68] O. Rusňáková, PhD dissertation, Czech Technical University in Prague (2015).
- [69] H. Masui, B. Mohanty and N. Xu, Phys. Lett. B **679**, 440 (2009).

Appendices

Appendix A

QA of EMC cuts

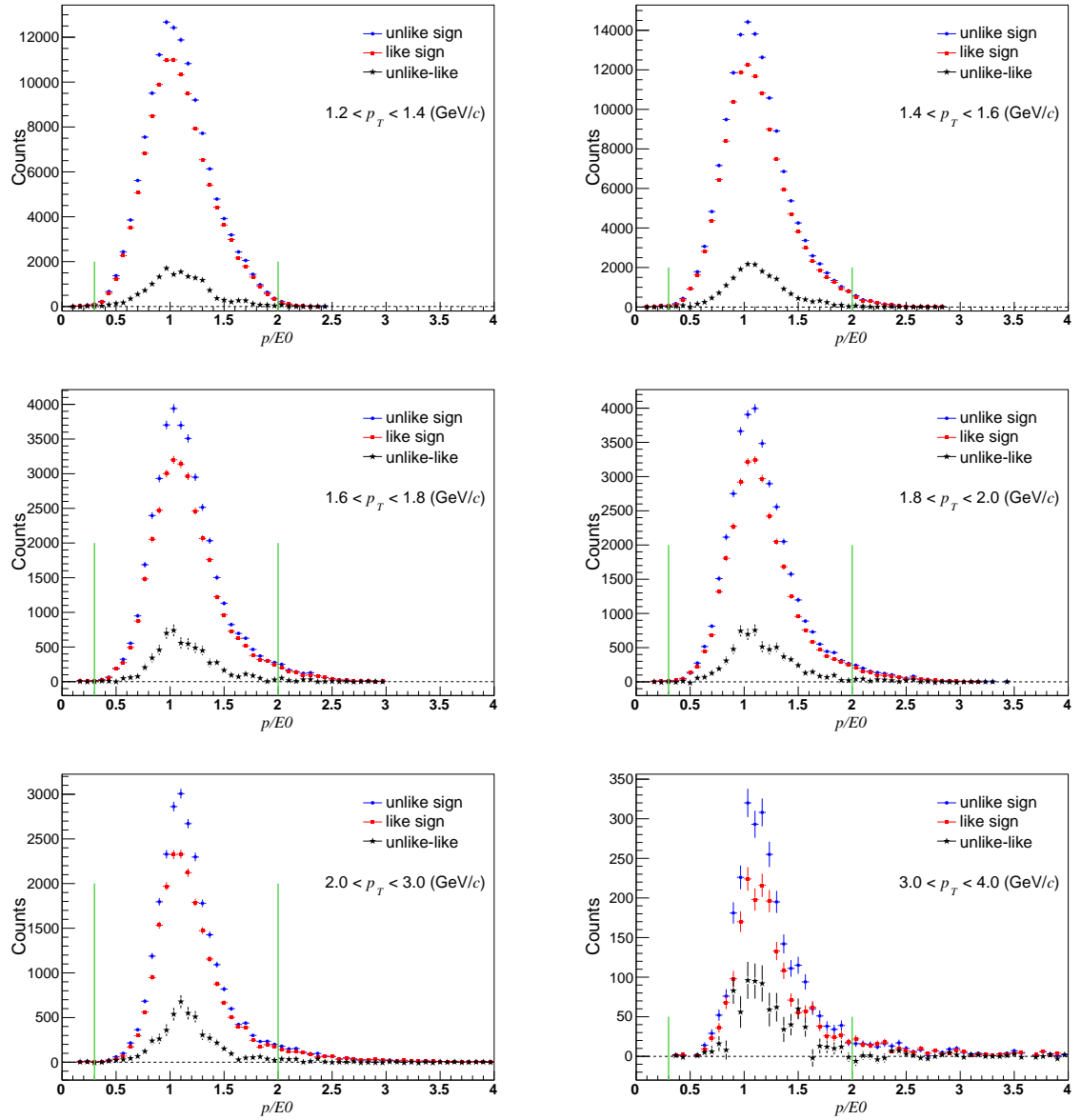
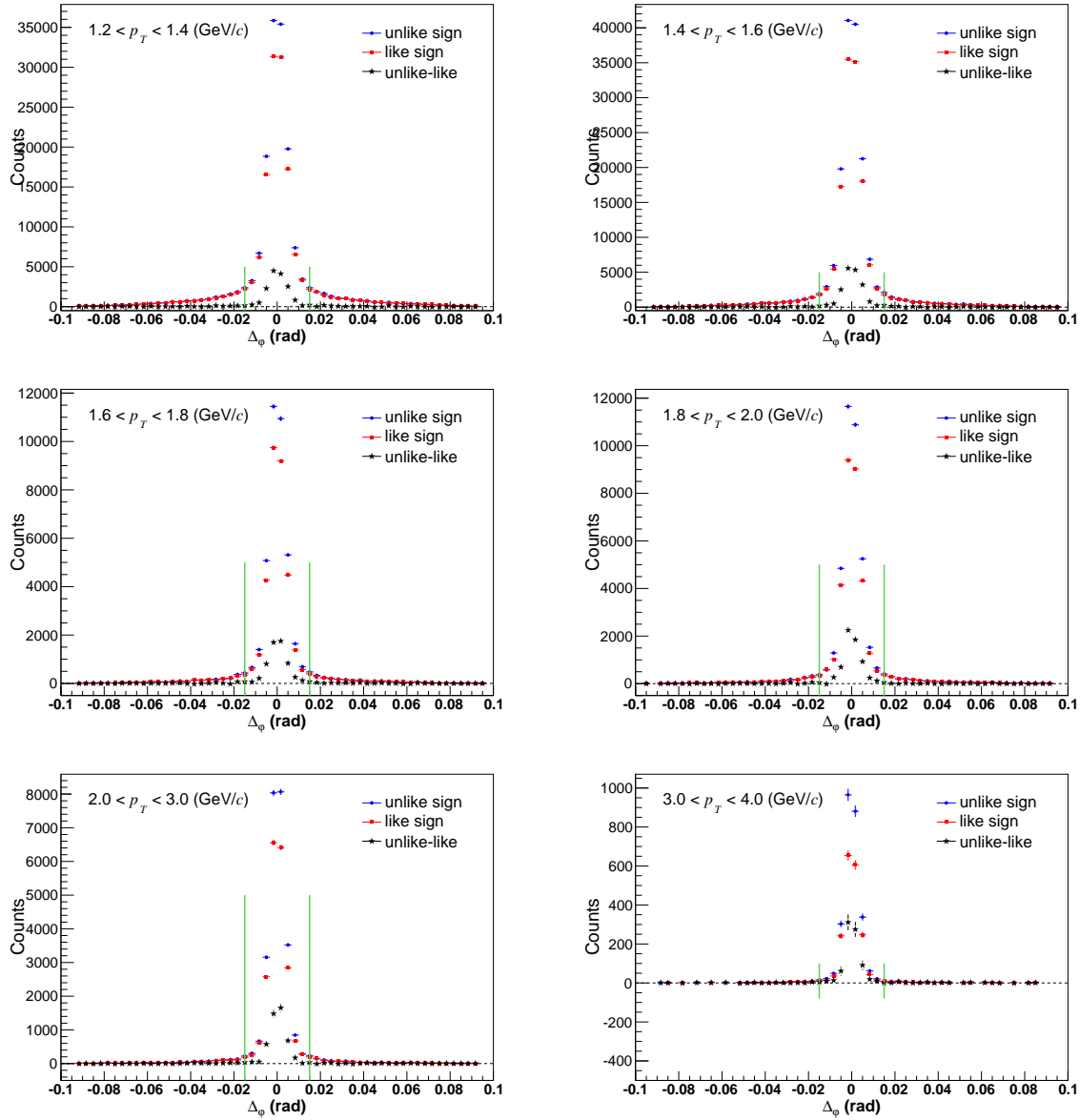


Figure A.1: Distributions of $p/E0$ cut.

Figure A.2: Distributions of Δ_φ cut.

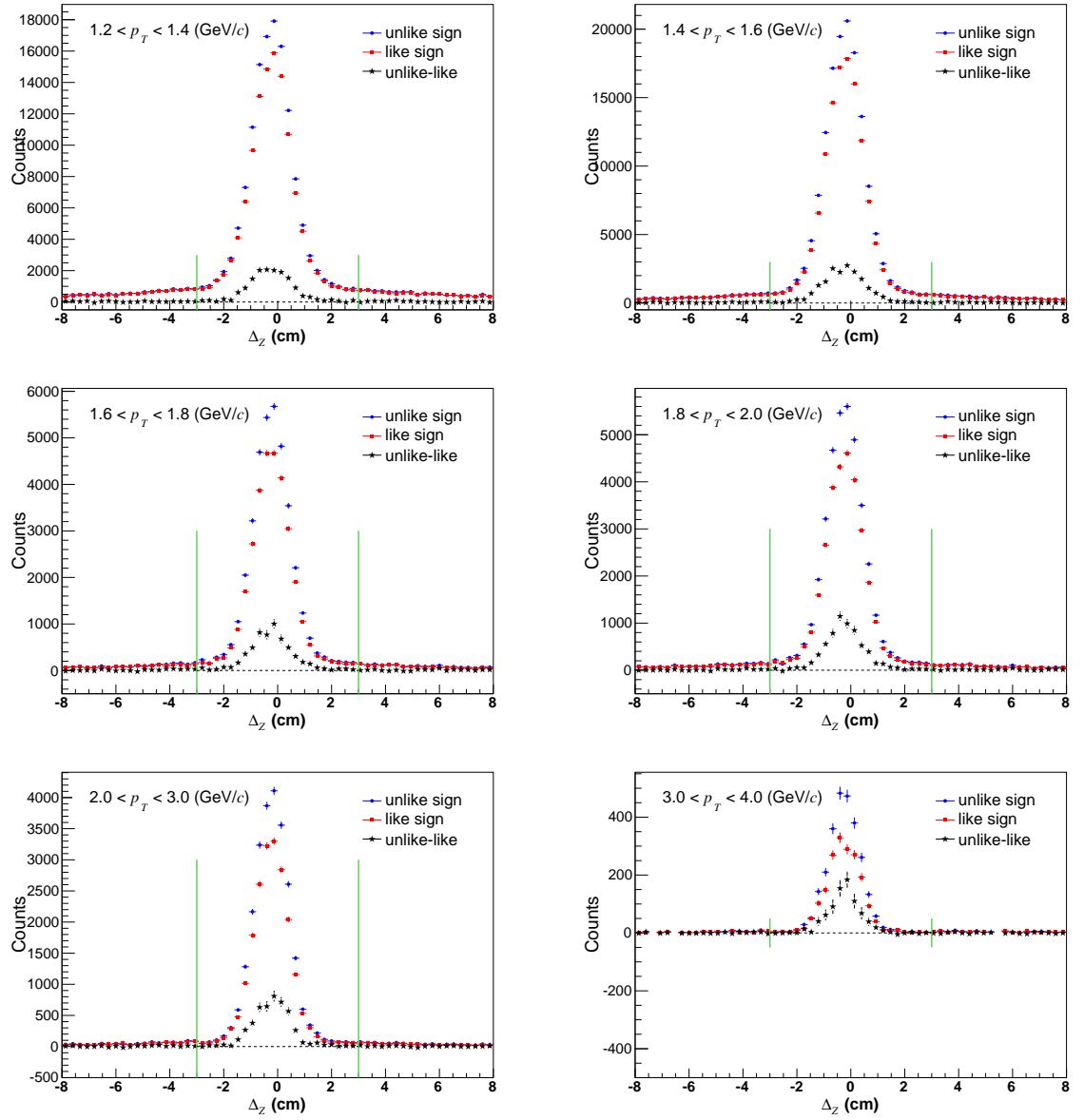


Figure A.3: Distributions of Δ_z cut.

Appendix B

Checking the purity of PHE

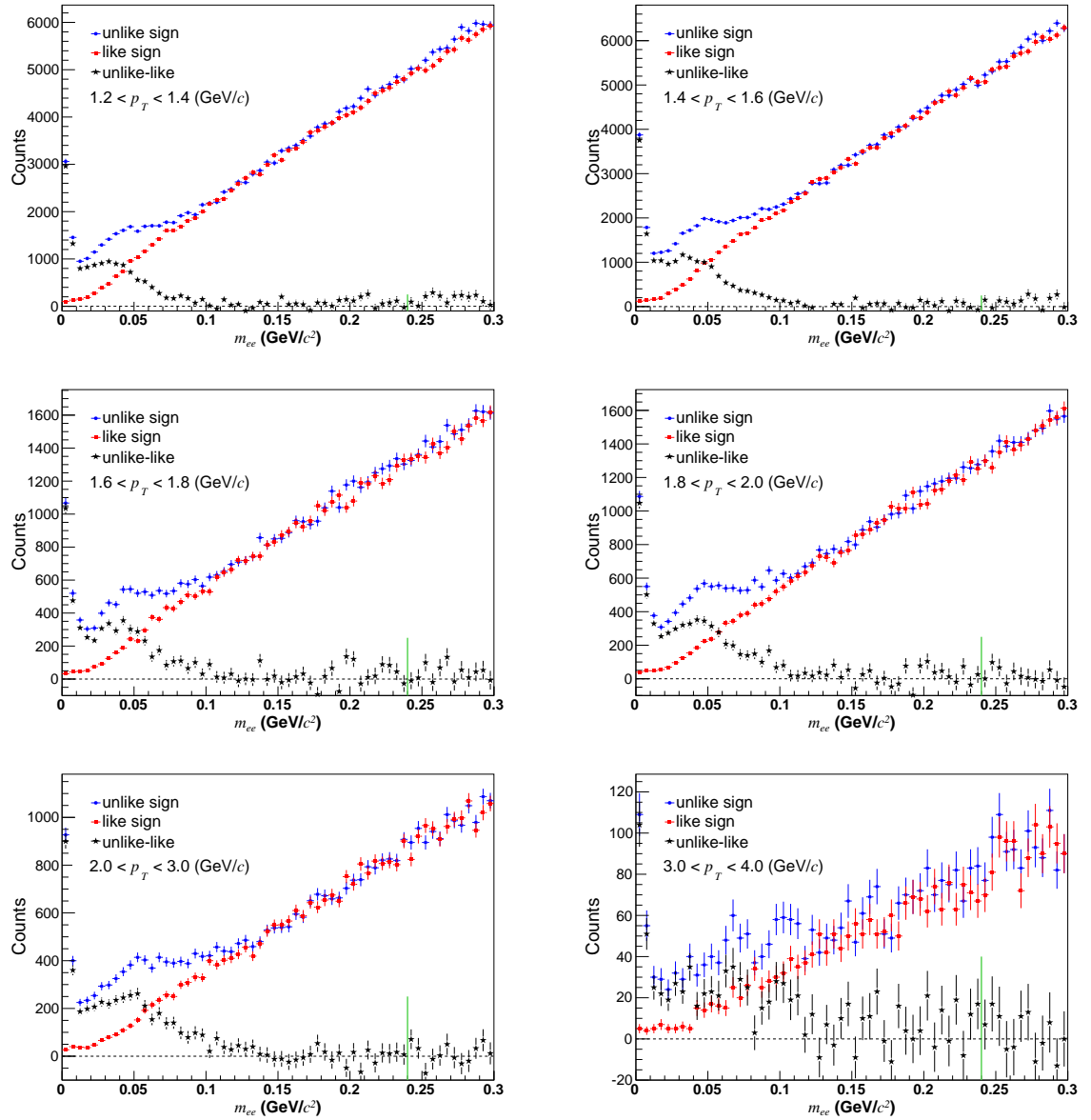
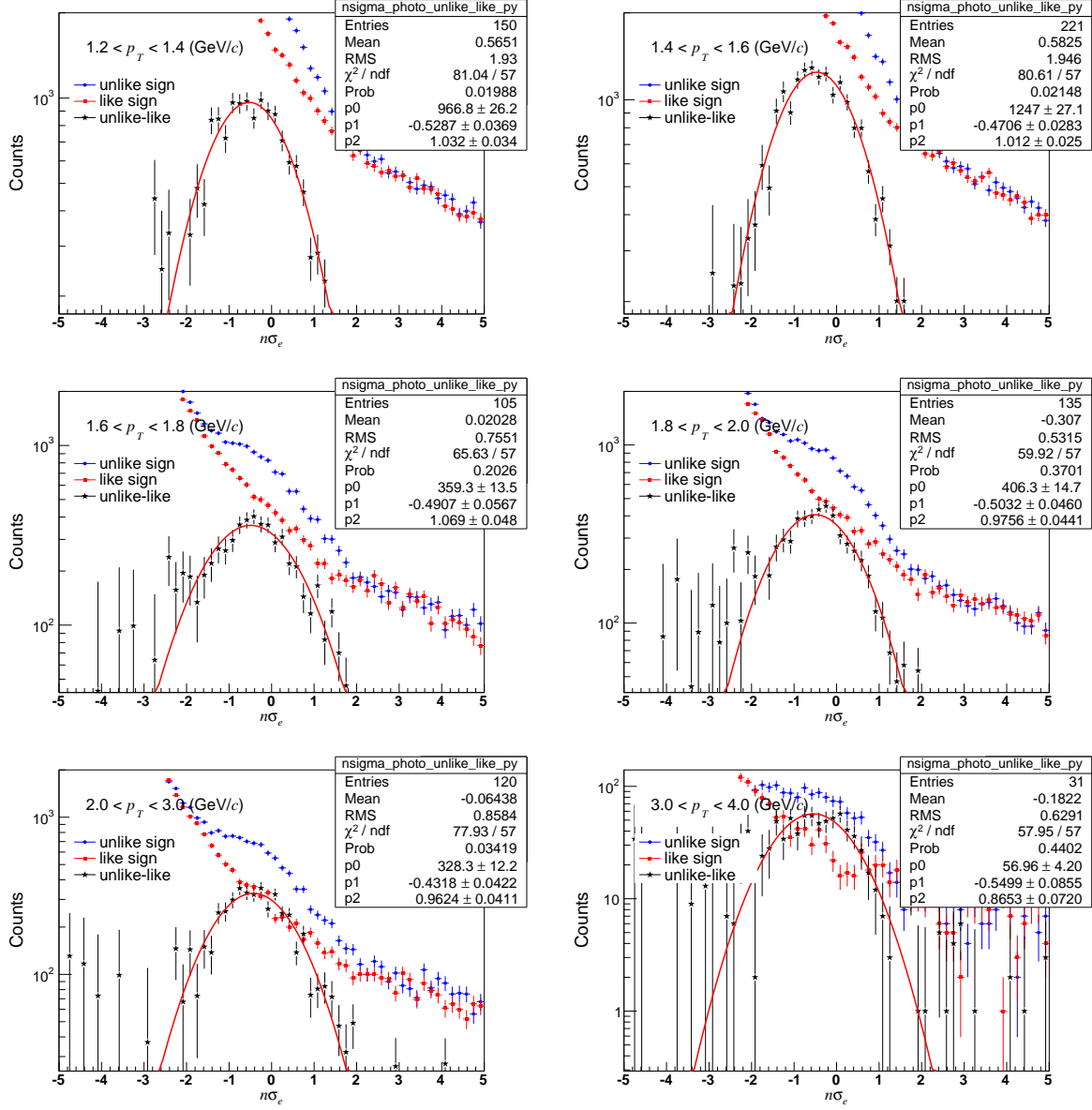


Figure B.1: Distribution of invariant mass of electron pairs.

Figure B.2: Distributions of $n\sigma_e$ of global partner tracks.

Appendix C

Efficiency studies

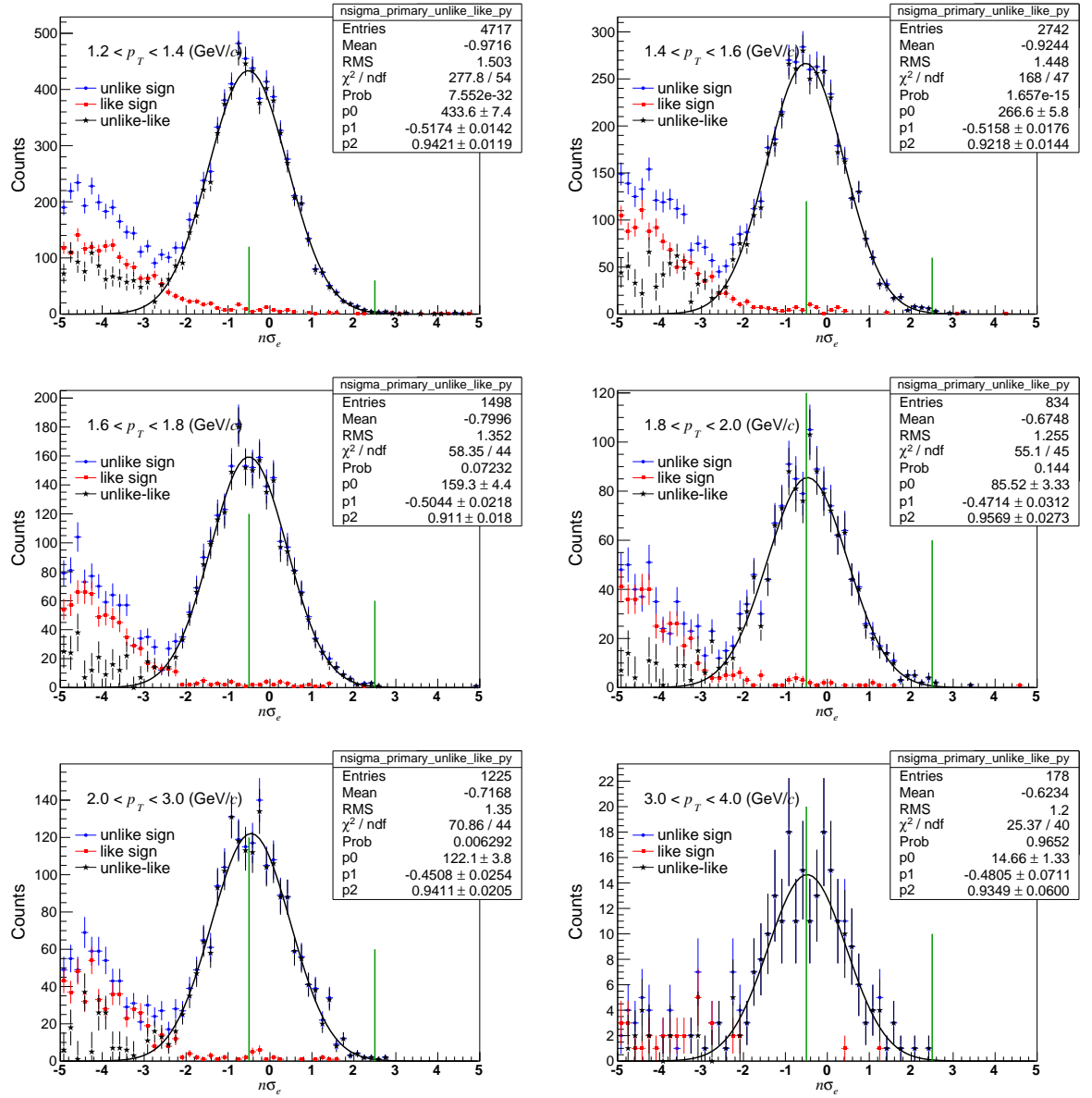


Figure C.1: Distributions of $n\sigma_e$ of primary electron tracks.

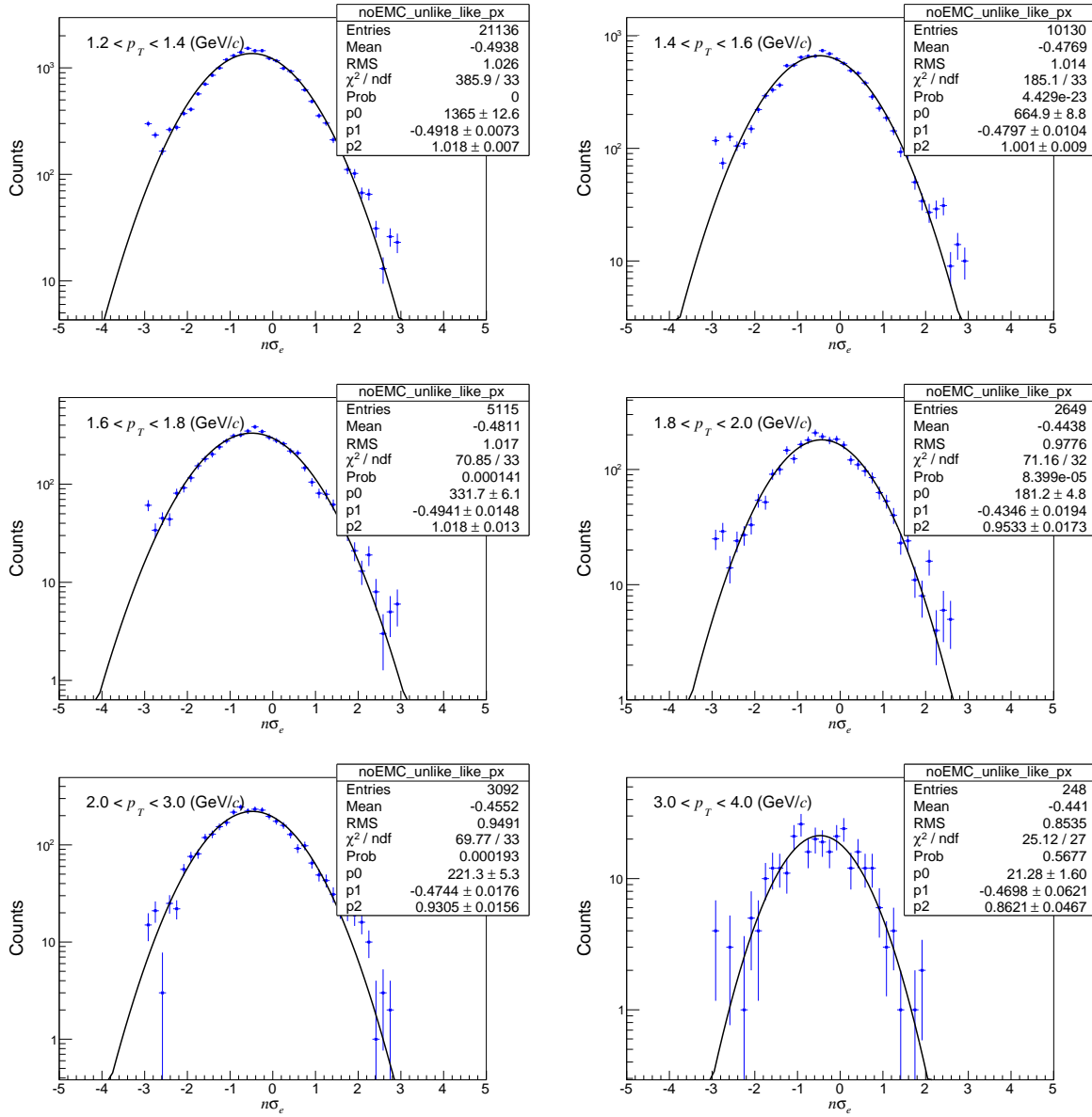


Figure C.2: Distributions of $n\sigma_e$ of global partner tracks without EMC cuts.

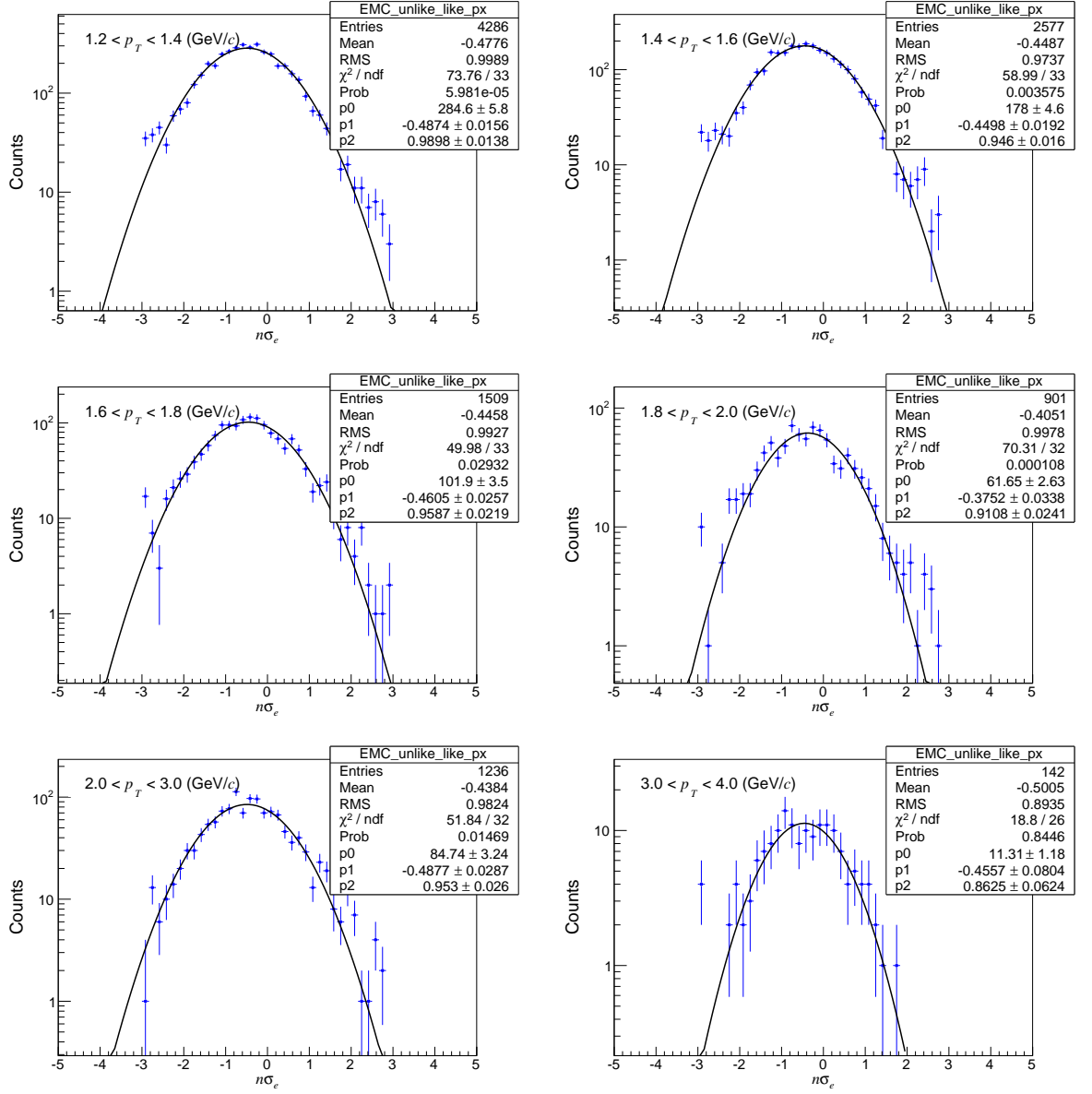


Figure C.3: Distributions of $n\sigma_e$ of global partner tracks with EMC cuts.

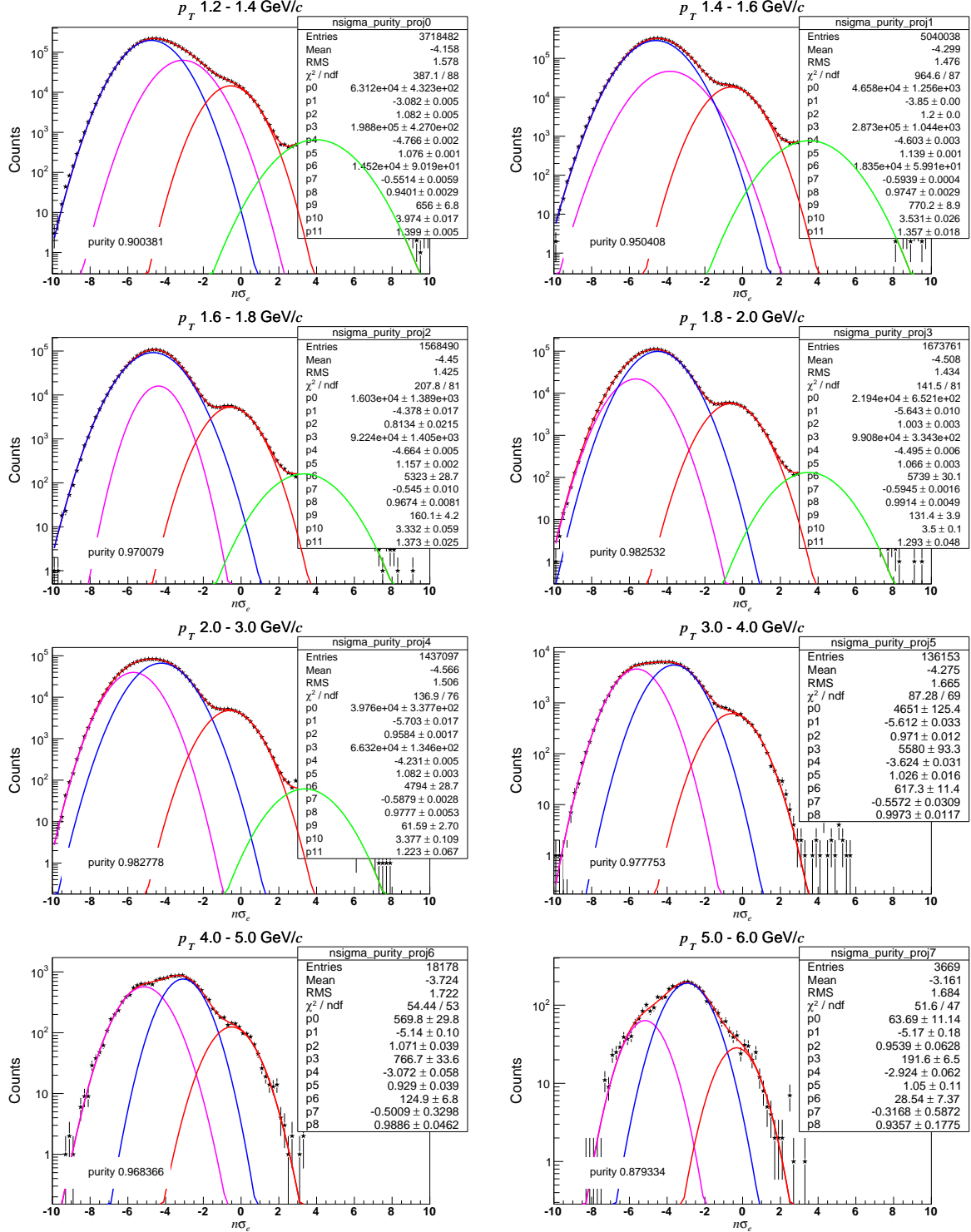


Figure C.4: Distributions of $n\sigma_e$ of inclusive electrons fitted with multi-Gaussian functions.

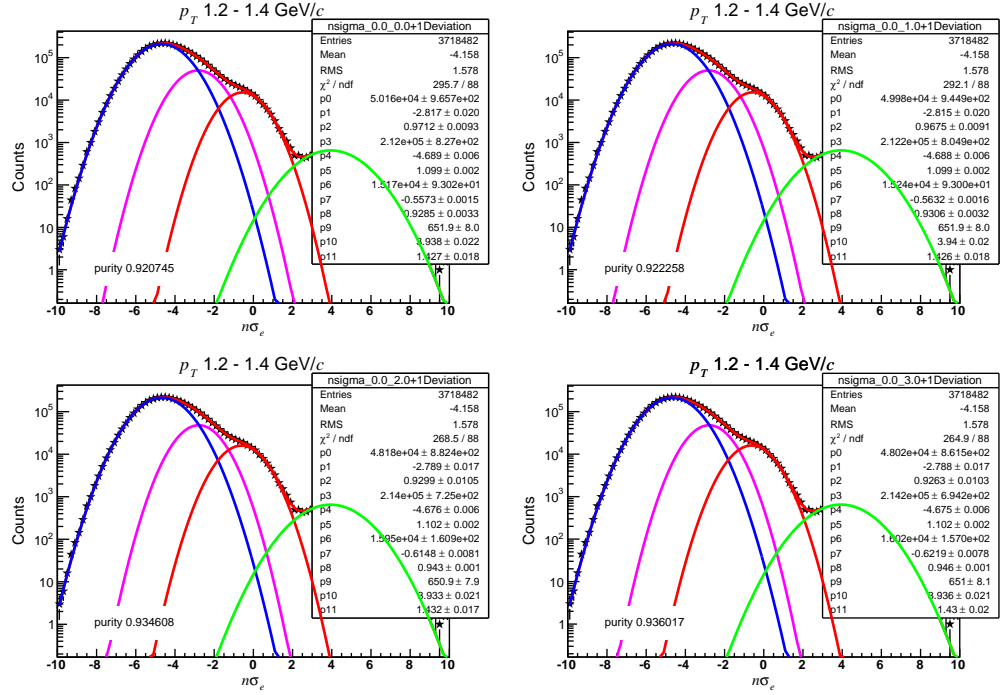


Figure C.5: Distributions of $n\sigma_e$ of inclusive electrons at $1.2 < p_T < 1.4$ GeV/c fitted with multi-Gaussian functions with different constraints on electron Gaussians.

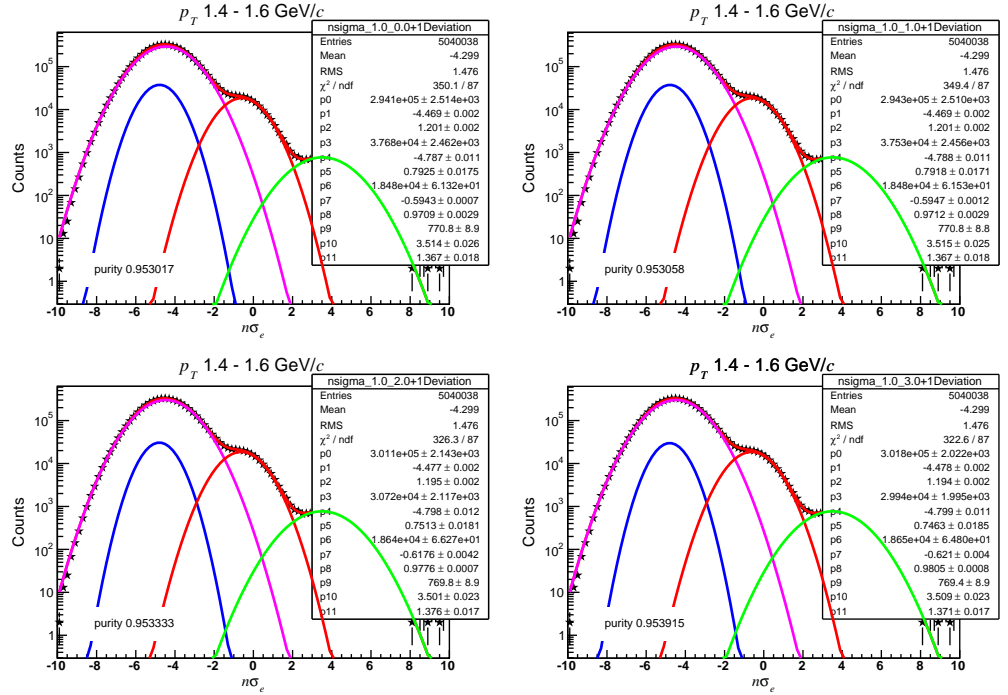


Figure C.6: Distributions of $n\sigma_e$ of inclusive electrons at $1.4 < p_T < 1.6$ GeV/c fitted with multi-Gaussian functions with different constraints on electron Gaussians.

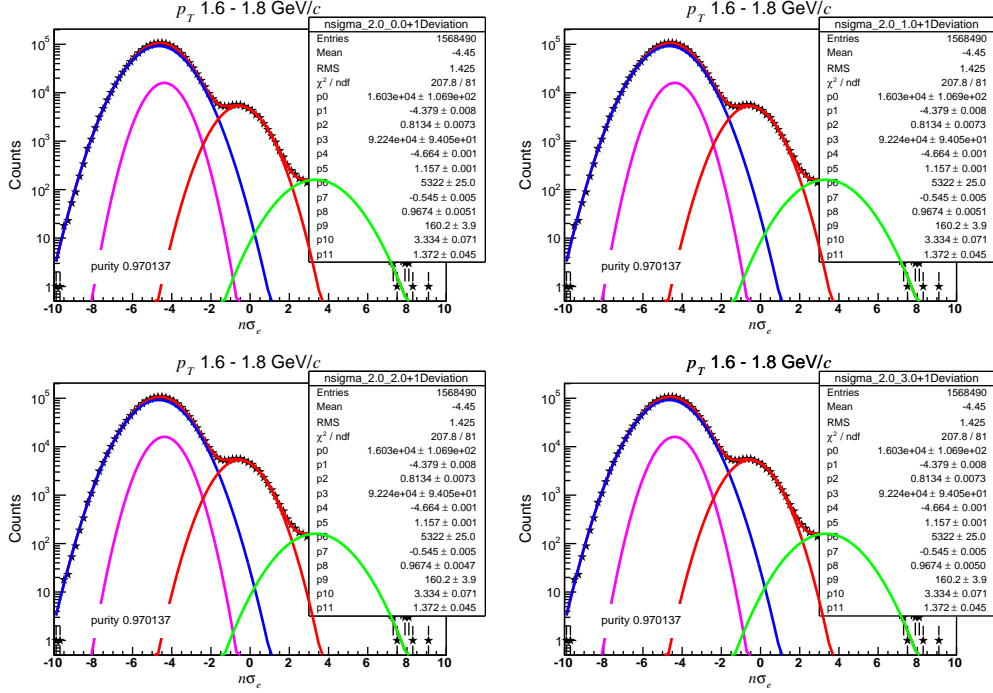


Figure C.7: Distributions of $n\sigma_e$ of inclusive electrons at $1.6 < p_T < 1.8$ GeV/c fitted with multi-Gaussian functions with different constraints on electron Gaussians.

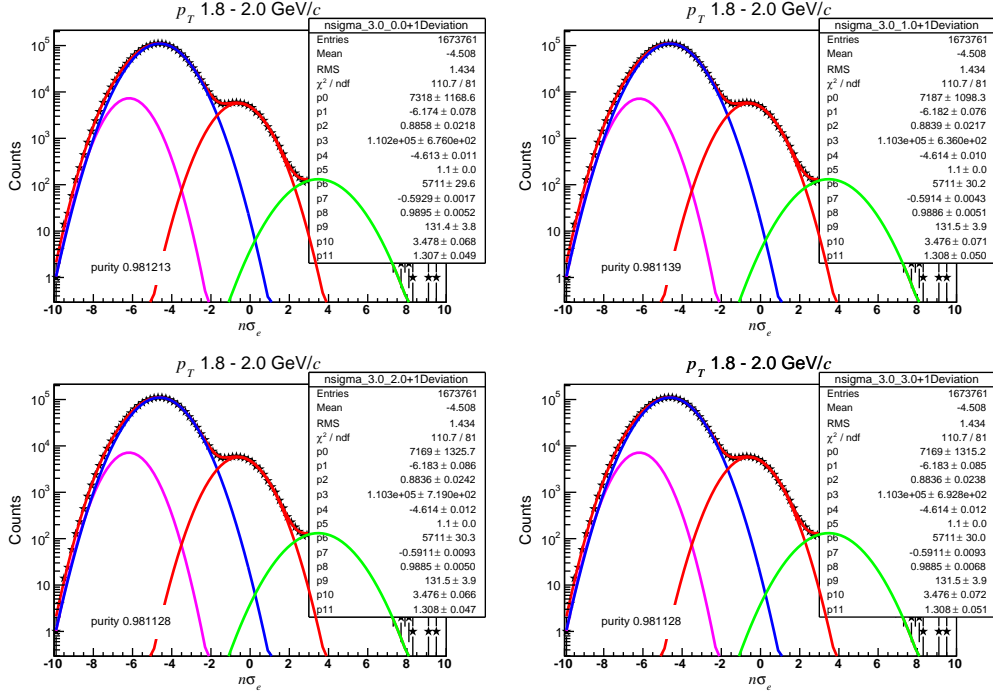


Figure C.8: Distributions of $n\sigma_e$ of inclusive electrons at $1.8 < p_T < 2.0$ GeV/c fitted with multi-Gaussian functions with different constraints on electron Gaussians.

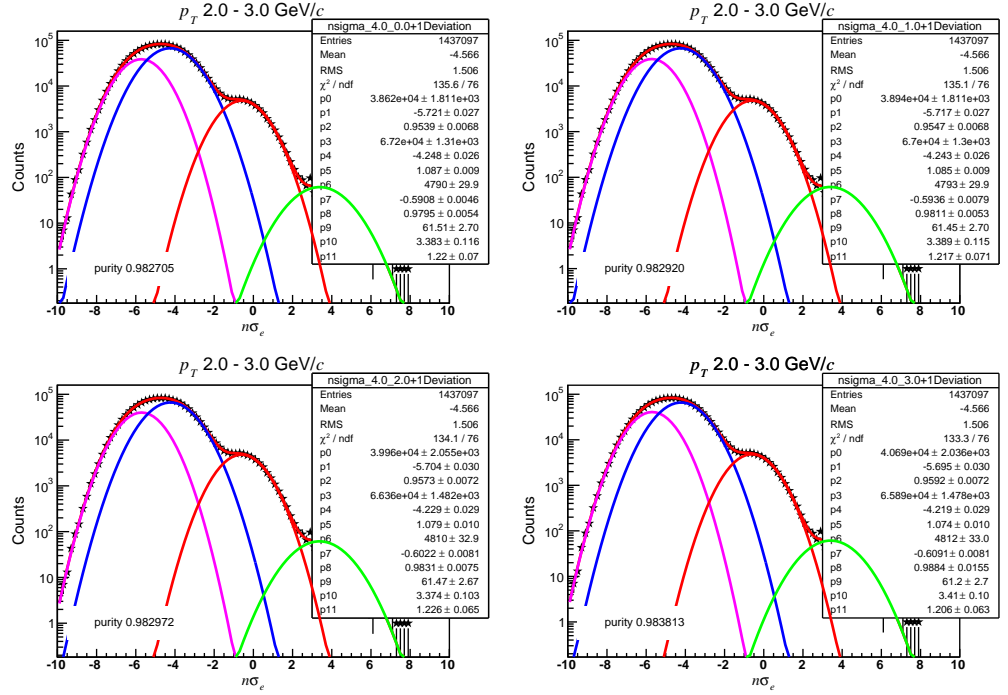


Figure C.9: Distributions of $n\sigma_e$ of inclusive electrons at $2.0 < p_T < 3.0$ GeV/c fitted with multi-Gaussian functions with different constraints on electron Gaussians.

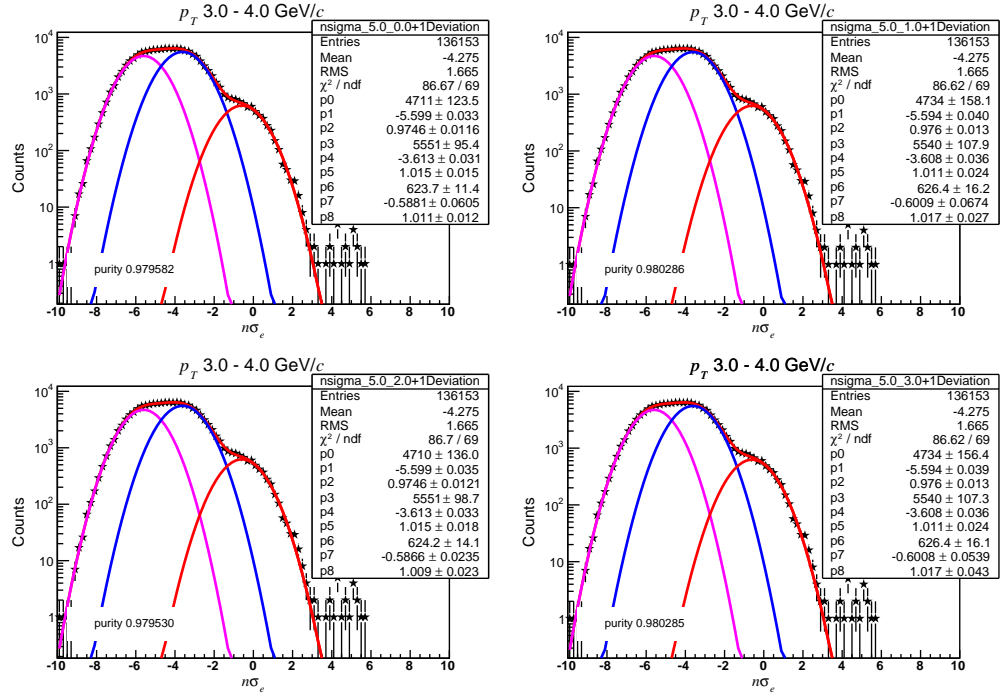


Figure C.10: Distributions of $n\sigma_e$ of inclusive electrons at $3.0 < p_T < 4.0$ GeV/c fitted with multi-Gaussian functions with different constraints on electron Gaussians.

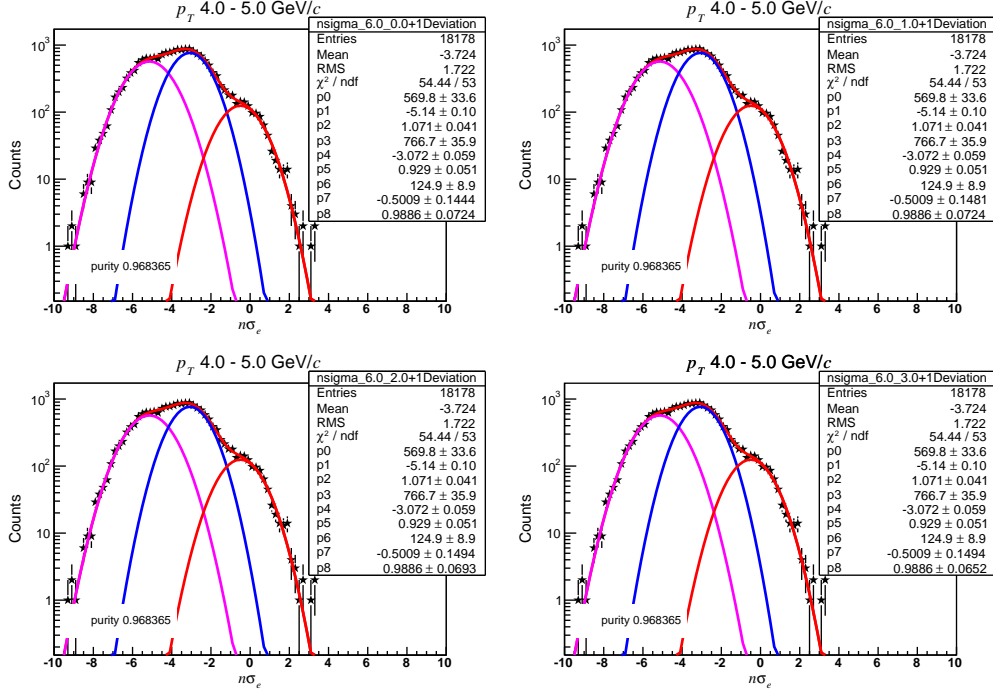


Figure C.11: Distributions of $n\sigma_e$ of inclusive electrons at $4.0 < p_T < 5.0$ GeV/c fitted with multi-Gaussian functions with different constraints on electron Gaussians.

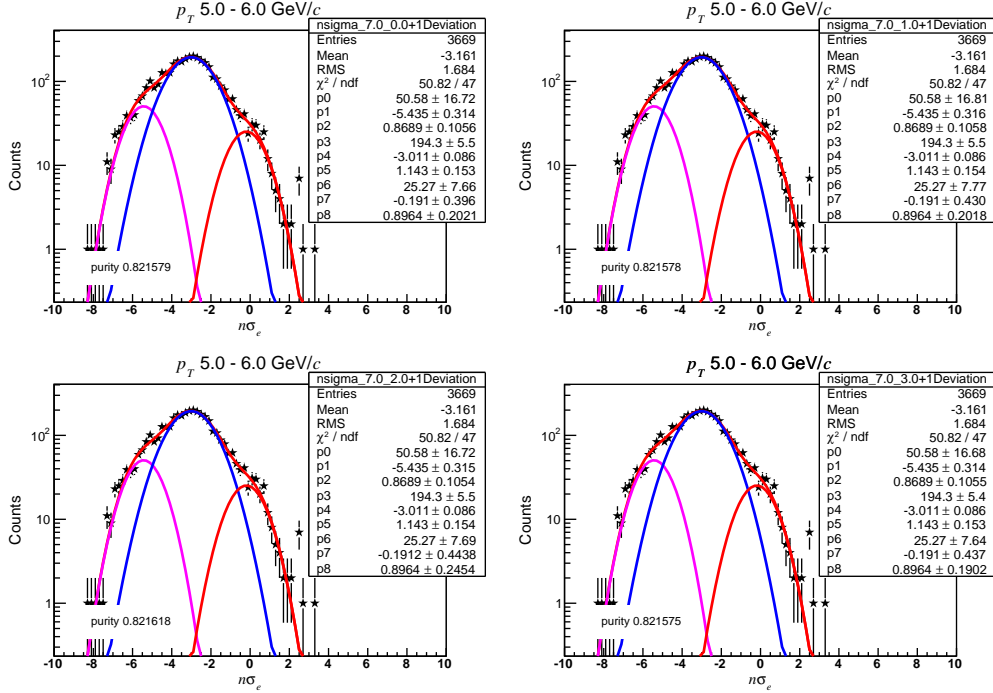


Figure C.12: Distributions of $n\sigma_e$ of inclusive electrons at $5.0 < p_T < 6.0$ GeV/c fitted with multi-Gaussian functions with different constraints on electron Gaussians.

Appendix D

List of public presentations and posters

1. Studentská vědecká konference 2014, University of Ostrava, May 6th 2014.
2. Poster from 53rd International Winter Meeting on Nuclear Physics, Bormio, Italy, 26-30 January 2015.
3. Proceedings from 53rd International Winter Meeting on Nuclear Physics, Bormio, Italy, 26-30 January 2015. Published in Proceedings of Science http://pos.sissa.it/archive/conferences/238/010/Bormio2015_010.pdf

NEFOTONICKÉ ELEKTRÓNY NA EXPERIMENTE STAR

Katarína Gajdošová

Fakulta jaderná a fyzikálně inženýrská

České vysoké učení technické v Praze

Břehová 7, 115 19 Praha 1

+420721511505

gajdokat@fifi.cvut.cz

Abstrakt

Kvarkovo-gluónová plazma (QGP) je husté a horúce médium, kde sa kvarky a gluóny voľne pohybujú. V laboratóriu sme schopní tieto podmienky vytvoriť v ultrarelativistických jadro-jadrových zrážkach na urýchľovačoch RHIC a LHC. QGP nemôžeme pozorovať priamo, len pomocou vlastností častíc, ktoré z nej vyletujú. Jednou z metód je štúdium nefotonických elektrónov (NPE), ktoré pochádzajú zo semileptonických rozpadov mezónov otvorených vôní obsahujúce ťažké kvarky c a b . V tomto príspevku diskutujeme meranie nefotonických elektrónov v experimente STAR v $p+p$ a $Au+Au$ zrážkach pri energii 200 GeV. Invariantné spektrum NPE z pp zrážok je konzistentné s hornou hranicou výpočtov z pQCD. V jadro-jadrových zrážkach pozorujeme, pôvodne neočakávané, potlačenie produkcie nefotonických elektrónov s vysokou hybnosťou rovnakej veľkosti ako u hadrónov, ktoré vznikajú z ľahkých kvarkov.

Keľúčové slová: kvark-gluónová plazma, STAR, jadrový modifikačný faktor, nefotonické elektróny.

Úvod

Jedným z hlavných predmetov výskumu súčasnej časticovej fyziky je hustá a horúca jadrová hmota zložená z voľných kvarkov a gluónov nazývaná kvarkovo-gluónová plazma (QGP). Predpokladá sa, že toto médium vzniklo pri Veľkom Tresku, kedy prevládali vysoké teploty a hustoty. Aby sme kvarkovo-gluónovú plazmu mohli pozorovať v laboratóriu, je potrebné zraziť ťažké častice pri vysokej energii, čo je možné na urýchľovačoch ako napríklad Relativistický urýchľovač ťažkých jadier RHIC v BNL. Tu sa okrem iného zrážajú jadrá zlata pri energii 200 GeV, a pokiaľ sa jadrá zrazia s dostatočnou centralitou, teda ak stredy zrážajúcich sa jadier budú dostatočne blízko pri sebe, vzniká QGP.

Vastnosti jadrovej hmoty za týchto podmienok ale nie sme schopní skúmať priamo, pretože trvá len veľmi krátku dobu (rádovo fs). Keď teplota média klesne pod kritickú hodnotu $T=175$ MeV [1], nastáva fázový prechod medzi QGP a plynom z hadrónov, kedy sa voľné kvarky a gluóny zviažu do hadrónových stavov. Vzniknuté častice vyletujú z miesta zrážky, a vďaka ich interakcii s materiálmi detektoru ich dokážeme identifikovať a na základe ich vlastností spätne zistiť, čo sa s kvarkami a gluónmi v QGP dialo.

Dôležitou časťou výskumu je štúdium ťažkých vôní, teda mezónov obsahujúcich jeden alebo dva ťažké c a b kvarky. Medzi ťažké vône sa radia kvarkonia a otvorené ťažké vône. Kvarkonia sú častice skladajúce sa z páru ťažkého kvarku a príslušného antikvarku. Príkladom je J/Ψ ($c\bar{c}$) a Υ ($b\bar{b}$). Otvorené ťažké vône sú mezóny skladajúce sa z jedného ťažkého c a b kvarku a jedného ľahkého kvarku. Medzi otvorené ťažké vône patria D a B mezóny.

Ťažké vône sú vhodnými sondami na skúmanie QGP, pretože vznikajú, pri dostatočnej energii, v ťažkých procesoch počas prvých fáz zrážky. Tým pádom sú prítomné vo všetkých

nasledujúcich fázach. Vďaka tomu je ich konečný výťažok, ktorý meriame, ovplyvnený interakciami s QGP. Aby sme zistili vplyv QGP na produkciu častíc otvorených vôní, je potreba ich výťažok z jadro-jadrových zrážok, kde QGP vzniká, porovnať s výťažkom z protón-protónových zrážok, kde sa QGP nevyskytuje. Veličina používaná na určenie efektov QGP na produkciu častíc je jadrový modifikačný faktor R_{AA} , čo je podiel produkcie častíc v jadro-jadrových zrážkach k produkcii v protón-protónových zrážkach. Celý podiel je škálovaný prelínacou funkciou z Glauberovho modelu, ktorá vyjadruje počet nukleón-nukleónových zrážok pri danom zrážkovom parametri b . Zrážkový parameter vyjadruje vzdialenosť stredu dvoch zrážajúcich sa jadier [1].

$$R_{AA} = \frac{d^2 N_{AA} / dy dp_T}{\langle T_{AA} \rangle (b) d^2 \sigma_{pp} / dy dp_T}$$

Ak sa jadrový modifikačný faktor pohybuje okolo 1, znamená to, že nepozorujeme rozdiel v produkcii častíc v pp a AA zrážkach. Vtedy sa nepredpokladá, že by v počiatkovej fáze vývoja jadrovej hmoty po zrážke existovala QGP. Ak je R_{AA} nad 1, nazývame to navýšenie. Ak je R_{AA} naopak pod 1, je to potlačenie. Ak výsledný jadrový modifikačný faktor vykazuje potlačenie, znamená to možnú existenciu QGP.

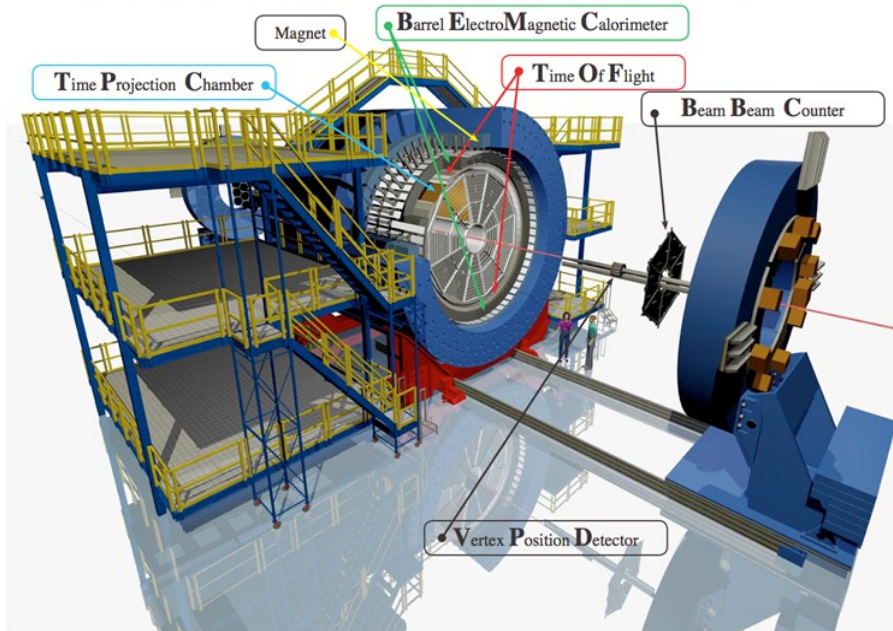
Vďaka javu v literatúre nazývanom jav mŕtveho kužeľu (dead-cone efekt) predpokladáme, že potlačenie produkcie otvorených vôní v jadro-jadrových zrážkach bude menšie ako potlačenie hadrónov pozostávajúcich z ľahkých kvarkov. Podľa tohto efektu ťažké kvarky strácajú menej energie v QGP vďaka potlačeniu emisie gluónov v uhloch menších ako je pomer ich energie a hmotnosti. Mali by sme teda pozorovať $R_{AA}^{ch} < R_{AA}^c < R_{AA}^b$ [2].

Detektor STAR

Detektor STAR, anglicky Solenoidal Tracker at RHIC, je jeden z dvoch detektorov fungujúcich na RHIC-u, ktorý je určený na skúmanie QGP. Pokrýva celý azimutálny uhol okolo zrážacej trubice. Skladá sa z viacerých podsystemov, z ktorých dôležité pre skúmanie ťažkých vôní sú Časovo projekčná komora TPC, Detektor doby letu TOF, Valcový elektromagnetický kalorimeter BEMC a novo pridané detektory Sledovač ťažkých vôní HFT a Miónový teleskopický detektor MTD. Celý detektor ešte obkolesuje magnet so silou 0,5 T, ktorý slúži na ohnutie trajektórií nabitých častíc. Na Obrázku 1. je znázornený detektor STAR spolu s označením jeho základných častí.

Časová projekčná komora je hlavný detektor STAR-u, ktorý slúži hlavne na zaznamenanie trajektórií nabitých častíc, teda na indentifikáciu častíc. Pomocou detektoru TOF môžeme rozlíšiť častice vo väčších intervaloch hybnosti. Na ich indentifikáciu použijeme dobu letu častice v detektore. Valcový elektromagnetický kalorimeter BEMC je potrebný pre zistenie energie častíc. Novo pridané detektory predstavujú významný krok pre fyziku ťažkých vôní. HFT bude schopný rozoznať rozpady ťažkých mezónov. Kvôli ich krátkej dobe života, a teda ich krátkej dráhe, sa rozpadajú ešte skôr ako stihnú vniknúť do TPC, a teda sme ich doteraz nemohli priamo indentifikovať. Detektor MTD je umiestnený za magnetom na olovených nohách, čo vedie k oddeleniu hadronického pozadia od miónov. Analýzou miónového rozpadového kanálu by sme mali byť schopní dostať signály s oveľa väčším rozlíšením.

Solenoidal Tracker At RHIC : $-1 < \eta < 1, 0 < \phi < 2\pi$



Obrázok 1. Detektor STAR [3].

Nefotonické elektróny

D a B mezóny sa môžu rozpadat' hadrónovým alebo leptónovým kanálom. V tomto príspevku sa zaoberám leptónovými kanálmi rozpadu ($D, B \rightarrow X l \nu_l$), hlavne rozpadmi na hadrón, elektrón (pozitron) a príslušné antineutrino (neutrino). Elektróny pochádzajúce prevažne z rozpadov otvorených ťažkých vóní sa nazývajú nefotonické elektróny. Túto analýzu sprevádza pozadie pochádzajúce z konverzií fotónov na elektron-pozitronový pár a Dalitzových rozpadov π_0 a η mezónov, hromadne nazvané fotonické elektróny [4].

Analýza na experimente STAR prebieha tak, že najprv sa zo všetkých vyprodukovaných častíc pri zrážke vyberú elektróny (tzv. inclusive yield), a následne sa podľa vzťahu

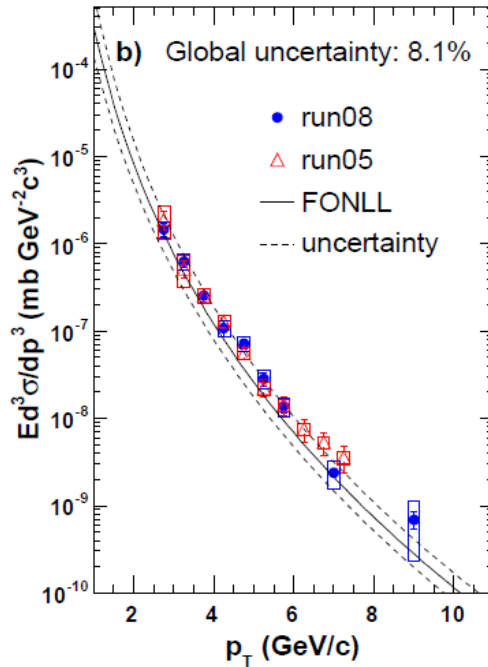
$$N(npe) = N(inc) / \epsilon_{purity} - N(pho) \cdot \epsilon_{pho}$$

od nich odčítajú fotonické elektróny. $N(npe)$ je nefotonický výťažok, $N(inc)$ celkový výťažok elektrónov, $N(pho)$ sú fotonické elektróny, ϵ_{pho} je efektívnosť rekonštrukcie fotonických elektrónov a ϵ_{purity} je čistota, ktorá udáva kontamináciu vzorky elektrónov hadrónmi [4].

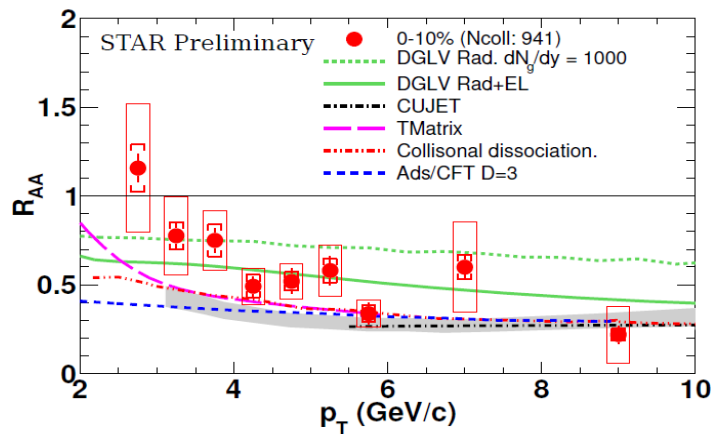
Analýzou nefotonických elektrónov v pp zrážkach testujeme teoretické výpočty Fixed Order Next to Leading Log poruchovej QCD. Invariantné spektrum, ktoré dostaneme z analýzy NPE, porovnávame s predpoveďami tejto teórie. Na Obrázku 2. je znázornené spektrum NPE v pp zrážkach pri energii 200 GeV v závislosti na pričnej hybnosti spolu s predpoveďou FONLL. Dáta sa zhodujú s hornou hranicou výpočtov [4].

Spektrum získané z AuAu zrážok pri energii 200 GeV bolo porovnané so spektrom z pp zrážok pri rovnakej energii pomocou jadrového modifikačného faktoru. Ukážka je na Obrázku 3. Dáta sú porovnané s rôznymi teoretickými výpočtami straty energie ťažkých kvarkov v prostredí

QGP. Teoretické predpovede založené na strate energie emisiou gluónov nedokážu popísať veľké potlačenie NPE, aj keď potlačenie ľahkých hadrónov popisujú dobre. Aby sme mohli rozhodnúť o platnosti iných teoretických modelov, potrebujeme dáta s väčšou presnosťou a merania iných citlivých veličín [5].



Obrázok 2. Invariantné spektrum NPE v závislosti na priečnej hybnosti. Modré body sú z dát z roku 2008 a červené z roku 2005. Plná čiara je výpočet FONLL a čiarkované čiary sú nepresnosti výpočtov FONLL [4].



Obrázok 3. Jadrový modifikačný faktor NPE v závislosti na priečnej hybnosti. Dáta sú porovnané s rôznymi teoretickými modelmi [5].

Záver

Nefotonické elektróny pochádzajúce zo semileptonických rozpadov otvorených vôní sú vhodnými sondami, pomocou ktorých môžeme späť zistiť, ako husté a horúce médium zvané kvarkovo-gluónová plazma vplýva na ťažké kvarky. Dáta z pp zrážok používame na otestovanie

FONLL poruchovej QCD. Dáta sa zhodujú s hornou hranicou predpovede. Porovnaním jadrového modifikačného faktoru z dát z AuAu zrážok s teoretickými výpočtami dostaneme spôsob straty energie ťažkých kvarkov v QGP. Kvôli veľkým štatistickým a systematickým chybám zatiaľ nie je možné presne určiť ktorý model vyhovuje dátam, no je už jasné, že modely založené na strate energie emisiou gluónov dáta dobre nepopisujú. Pre ďalšie konštatovania potrebujeme dáta s väčšou štatistikou.

Táto práca bola podporovaná grantom 13-02841S Grantovou agentúrou Českej republiky (GACR) a grantom Studentské grantové súťaže ČVUT č. SGS13/215/OHK4/3T/14.

Literatura

- [1.] STOCK, R. *Relativistic Nucleus-Nucleus Collisions and the QCD Matter Phase Diagram*, arXiv: 0807.1610v1 (2008).
- [2.] Y.L. Dokshitzer and D.E. Kharzeev, *Phys. Lett.* **B 519**, 199 294 (2001).
- [3.] Bielčík, J. *Quarkonium measurements in the STAR experiment*, prezentácia na 6th International Conference on Hard and Electromagnetic Probes of High-Energy Nuclear Collisions, Cape Town (2013).
- [4.] STAR Collaboration, *High p_T non-photonic electron production in $p+p$ collisions at $\sqrt{s}=200$ GeV*, *Phys. Rev.* **D83**, 052006 (2011).
- [5.] M. Mustafa for STAR Collaboration, *Measurements of Non-photonic Electron Production and Azimuthal Anisotropy in $\sqrt{s}=39,62.4$ and 200 GeV in Au+Au Collisions from STAR at RHIC*, arXiv: 1210.5199v2 (2012).

Abstract

Quark-gluon plasma (QGP) is a hot and dense medium in which quarks and gluons move freely. In laboratory we are able to create this medium in ultrarelativistic heavy-ion collisions on accelerators RHIC and LHC. We cannot observe QGP directly, just through properties of particles that come out from the medium. One of the methods is study of non-photonic electrons (NPE), which come from semileptonic decays of open flavors containing heavy c and b quarks. In this letter we discuss the measurement of non-photonic electrons in STAR experiment in $p+p$ and Au+Au collisions at energy 200 GeV. Invariant spectrum of NPE in pp collisions is consistent with the upper limit of pQCD calculations. In heavy-ion collisions we observe the same suppression of NPE production at high momenta as suppression of hadrons created from light quarks, which was not expected.



Measurement of electrons from heavy flavor decays at the STAR experiment

Katarína Gajdošová for the STAR Collaboration

Faculty of Nuclear Sciences and Physical Engineering
Czech Technical University in Prague



CZECH
TECHNICAL
UNIVERSITY
IN PRAGUE

Introduction

Heavy quarks, charm (c) and bottom (b), are one of the most promising probes for the hot QCD medium created in the later stages of ultrarelativistic heavy-ion collisions at RHIC and the LHC. These quarks are created during the early stages of heavy-ion collisions before the creation of the QGP. Electrons from semi-leptonic decays of D and B mesons, the so-called non-photonic electrons (NPE), can serve as a good proxy for heavy flavor quarks. Studies of NPE production in p+p collisions are important as a test of perturbative QCD calculations. In heavy-ion collisions the nuclear modification factor R_{AA} is studied as a variable sensitive to the effects of QGP on heavy quarks. Elliptic flow, v_2 , characterizes azimuthal anisotropy and is used to further study the interaction between the heavy quarks and the medium. Finite v_2 and modified R_{AA} indicates the strong interaction of these quarks with the medium. At the moment, models can not reproduce R_{AA} and v_2 simultaneously.

Detector layout

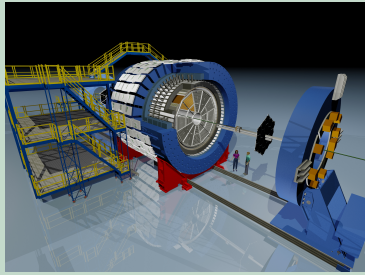


Figure 1: View of the STAR detector.

The Solenoidal Tracker at RHIC (STAR) covers 2π in azimuth and two units of pseudorapidity around mid-rapidity. It is wrapped inside the magnet, which has a field strength of 0.5 T. The main tracking detector Time Projection Chamber (TPC) is used for tracking and par-

ticle identification utilizing the ionization energy loss in the TPC gas. The Time of Flight (ToF) detector is able to further improve the electron identification at low p_T via the measurements of the velocity of particles. The energy of electrons is obtained via the Barrel Electromagnetic Calorimeter (BEMC), which also improves electron identification at high p_T .

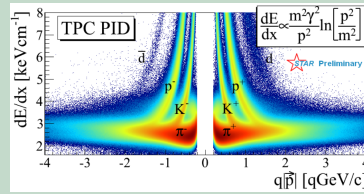


Figure 2: Particle identification using TPC.

Methods

- Non-photonic electrons originate from semileptonic decays of open heavy flavor $D(B) \rightarrow X e, \Lambda_c \rightarrow e X$
- Studies of NPE production need to be corrected for a large background composed mainly of conversion electrons, electrons from Dalitz decays and also leptonic decays of vector mesons

$$N_{npe} = N_{inclusive} * \epsilon_{purity} - N_{photon}/\epsilon_{photon}$$

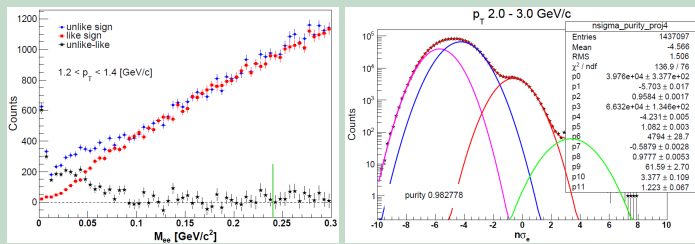


Figure 3: Invariant mass of electron pairs (left); Electron energy loss distribution (right).

- Nuclear modification factor** is defined as the ratio of particle production in heavy-ion collisions to production in p+p collisions scaled by mean number of binary collisions

$$R_{AA} = \frac{1}{\langle N_{bin} \rangle} \frac{d^2 N_{AA}/dp_T dy}{d^2 N_{pp}/dp_T dy}$$

- Elliptic flow** describes the azimuthal anisotropy of final particles due to collective motion.

$$\frac{dN}{d\varphi} \approx [1 + 2v_1 \cos\varphi + 2v_2 \cos(2\varphi) + \dots]$$

Conclusion

The invariant yield of NPE from p+p collisions agree well with FONLL perturbative QCD calculations within theoretical uncertainties. The nuclear modification factor of non-photonic electrons in Au+Au collisions at 200 GeV reveal strong suppression at high p_T . The comparison with models shows that heavy quarks lose energy in QGP not only through gluon radiation. The elliptic flow of non-photonic electrons in heavy-ion collisions is finite at low p_T , which together with the suppression indicates strong interaction of heavy quarks with the Quark-Gluon Plasma.

p+p collisions at $\sqrt{s} = 200$ GeV

- The invariant yield of non-photonic electrons in p+p collisions is important as a test of pQCD calculations.
- STAR measured NPE yield in the region $0.5 < p_T < 14$ GeV/c [1]; measurements are consistent with PHENIX data [2].
- The invariant yield of non-photonic electrons is well described by Fixed Order Next-to-Leading Logarithm (FONLL) pQCD calculations [3].

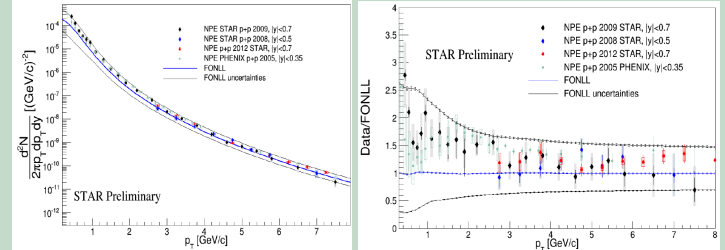


Figure 4: Spectrum of NPE (left); Ratio of the NPE spectrum and theory (right) [1].

Au+Au collisions at $\sqrt{s_{NN}} = 200$ GeV

- At 0-10% central Au+Au collisions at $\sqrt{s_{NN}} = 200$ GeV the STAR experiment observes a strong **suppression at high p_T** . NPE production in heavy-ion collisions is suppressed due to energy loss of heavy quarks in the strongly interacting medium.
- The theoretical model based on the energy loss caused only by gluon radiation does not describe the data well in the measured p_T region.

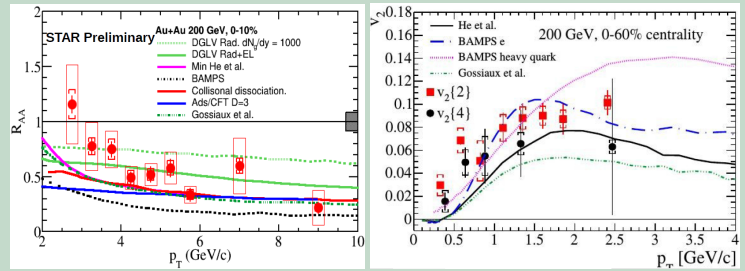


Figure 5: Nuclear modification factor of NPE (left); Elliptic flow of NPE (right) [4].

- A finite v_2 is observed at low p_T in Au+Au collisions, which indicates strong in-medium interactions of heavy quarks [4].
- The increasing v_2 towards higher p_T can be described by jet-like correlations that are also present in p+p collisions.
- Theoretical models that are able to describe the nuclear modification factor fail in explaining the elliptic flow.

Au+Au collisions at $\sqrt{s_{NN}} = 39, 62.4$ GeV

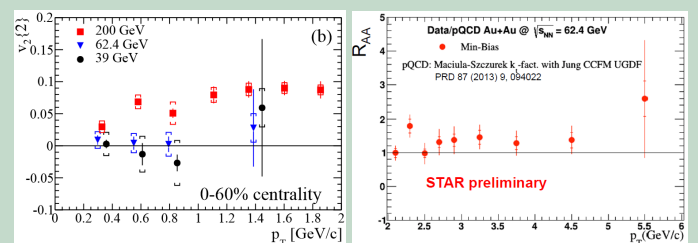


Figure 6: Elliptic flow of NPE (left) [4]; Nuclear modification factor of NPE (right).

- v_2 is consistent with zero for $p_T < 1$ GeV/c and statistically different from that at 200 GeV; no suppression to pQCD calculation is observed at $\sqrt{s_{NN}} = 62.4$ GeV.
- Cold Nuclear Matter effect (for instance Cronin enhancement) could be more significant at lower beam energies and needs to be studied.

References

- H. Agakishiev for STAR Collaboration, *Phys. Rev. D* **83**, 052006 (2011).
- A. Adare for PHENIX Collaboration, *Phys. Rev. C* **84**, 044905 (2011).
- A.D. Frawley, T. Ullrich and R. Vogt, *Phys. Rept.* **462**, 125 (2008).
- STAR Collaboration, arXiv: 1405.6348 (2014).

This work was supported by Grant Agency of the Czech Technical University in Prague, grant No. SGS13/215/OHK4/35/14 and by Grant Agency of the Czech Republic, grant No. 13-20841S.

This poster was presented at the 53rd International Winter Meeting on Nuclear Physics in Bormio, Italy.

Measurements of electrons from heavy flavor decays at the STAR experiment

Katarina Gajdosova for STAR Collaboration*

Department of Physics

Faculty of Nuclear Sciences and Physical Engineering

Czech Technical University in Prague

Břehová 7, 115 19 Prague 1, Czech Republic

E-mail: gajdokat@fjfi.cvut.cz

A hot and dense form of matter with deconfined quarks and gluons is called the quark-gluon plasma (QGP). The properties of this medium are being studied in ultrarelativistic heavy-ion collisions at the Relativistic Heavy Ion Collider (RHIC). One of the experimental probes that enable us to reveal the properties of the QGP are heavy quarks, such as c and b . Non-photonic electrons (NPE) that originate from semileptonic decays of D and B mesons can serve as a good proxy for heavy quarks. NPE in both p+p and Au+Au collisions are measured at RHIC. The p+p collisions are important as a baseline for the comparison with heavy-ion collisions and as a test of pQCD calculations. In Au+Au collisions the nuclear modification factor R_{AA} is measured, which is sensitive to the effects of QGP on heavy quark production. Also the measurements of azimuthal anisotropy parameter, v_2 , are important to further study the interaction between the heavy quarks and the medium.

In this proceedings measurements of NPE in different collision systems and at different beam energies are presented. In p+p collisions at $\sqrt{s} = 200$ GeV the invariant NPE spectra are shown in a wide transverse momentum range. In Au+Au collisions the results of R_{AA} and v_2 at $\sqrt{s_{NN}} = 200$ GeV are discussed, as well as the dependence of these variables on the collisional energy $\sqrt{s_{NN}} = 39, 62.4$ and 200 GeV.

*53rd International Winter Meeting on Nuclear Physics,
26-30 January 2015
Bormio, Italy*

*Speaker.

1. Introduction

Heavy quarks, charm (c) and bottom (b), are one of the most promising probes for the hot QCD medium created in later stages of ultrarelativistic heavy-ion collisions at RHIC and the LHC, called the Quark-Gluon Plasma (QGP). These quarks are created during the early stages of heavy-ion collisions from scatterings with large momentum transfer before the creation of the QGP. Therefore, their initial production is not affected by the QGP. However, the final distribution of particles composed of these heavy quarks is affected by the interaction between heavy quarks and the QGP.

Heavy quarks have been studied at the STAR experiment via measurements of open heavy flavor mesons through hadronic decay channels in p+p and Au+Au collisions at $\sqrt{s_{NN}} = 200$ GeV [1], [2]. Also, measurements of heavy quarks confined in charmonia or bottomia were performed. Results on J/ψ production in Au+Au and Cu+Cu collisions at $\sqrt{s_{NN}} = 200$ GeV are presented in [3] and Υ measurements in d+Au and Au+Au collisions at $\sqrt{s_{NN}} = 200$ GeV can be found in [4]. Studies reveal a clear sign of interaction of heavy quarks with the hot and dense medium.

Electrons from semi-leptonic decays of D and B mesons, the so-called non-photonic electrons (NPE), can serve as a good proxy for heavy quarks. Semileptonic decay channel of open heavy flavor mesons is also an interesting approach to the study of heavy quarks because of the ability of STAR detector to trigger on high p_T electrons. The STAR experiment has already seen a large suppression of electrons produced from semileptonic decays of heavy flavor mesons in central Au+Au collisions [5] and we discuss these results later on. The PHENIX experiment has also performed numerous studies of the heavy flavor quarks. Studies of NPE production in proton-proton collisions are important as a test of perturbative QCD calculations and also serve as a baseline for the studies of NPE spectra in heavy-ion collisions. Heavy flavor decay electrons were measured in p+p collisions at $\sqrt{s} = 200$ GeV [6], [7] as well as in Cu+Cu and Au+Au collisions at $\sqrt{s_{NN}} = 200$ GeV [8], [9]. Observation of dependence on system size was published in [10] and the Cold Nuclear Matter effects, such as Cronin effect, were studied in d+Au collisions at $\sqrt{s_{NN}} = 200$ GeV [11], [12].

In heavy-ion collisions the nuclear modification factor R_{AA} is a variable sensitive to the effects of QGP on heavy quark production. It is defined as the ratio of particle production in heavy-ion collisions to particle production in proton-proton collisions scaled by the mean number of binary collisions:

$$R_{AA} = \frac{1}{\langle N_{bin} \rangle} \frac{dN_{AA}^2/dydp_T}{dN_{pp}^2/dydp_T}. \quad (1.1)$$

If $R_{AA} = 1$, a heavy-ion collision is just a superposition of multiple proton-proton collisions. If the nuclear modification factor is below unity, it indicates a suppression, which means that at given p_T and rapidity there are less particles produced in heavy-ion collisions compared to p+p collisions due to possible effects of Quark-Gluon Plasma.

The elliptic flow v_2 is used to further study the interaction between heavy quarks and the medium. It is defined as the second parameter in the Fourier series of particle production in terms of azimuthal angle ϕ with respect to reaction plane:

$$\frac{dN}{d\phi} \propto [1 + 2v_1 \cos \phi + 2v_2 \cos(2\phi) + \dots]. \quad (1.2)$$

2. Detector layout

The Solenoidal Tracker at RHIC (STAR), is one of the two detectors active at the Relativistic Heavy Ion Collider at the Brookhaven National Laboratory. The detector covers 2π in azimuth and two units of pseudorapidity around mid-rapidity and is wrapped inside a solenoidal magnet, which has a field strength of 0.5 T.

The STAR detector is composed of various subdetectors, each of them fulfilling different task in the particle detection. The detector is shown in the Fig. 1 (left).

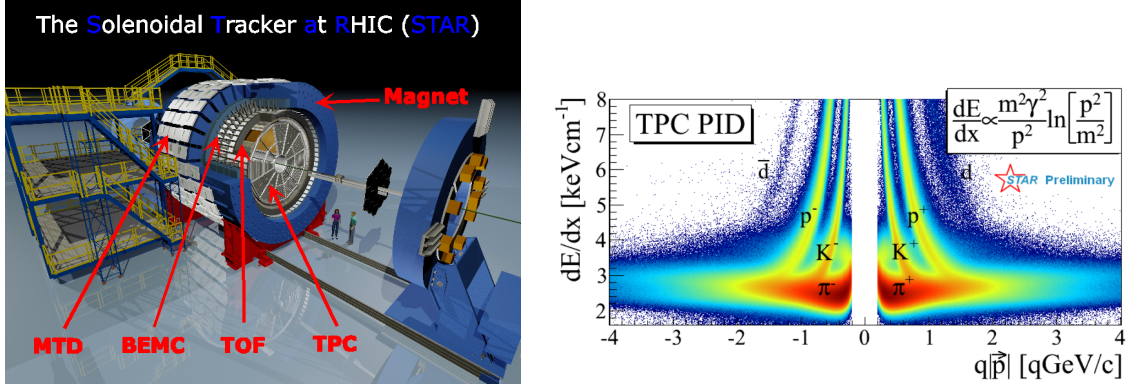


Figure 1: Left: View of the STAR detector. Right: Particle identification using TPC.

The main detector of the STAR is the so-called Time Projection Chamber (TPC), which is a gas detector designed for tracking and particle identification using their ionization energy loss in the gas as can be seen in Fig. 1 (right). The Time of Flight (ToF) detector is situated outside of the TPC. This detector is able to improve the particle identification at low p_T via the measurements of velocities of particles. The energy of electrons is obtained from the Barrel Electromagnetic Calorimeter (BEMC), which is outside of the ToF and also improves electron identification at high transverse momentum p_T .

The STAR detector was upgraded in the year 2014 with two new subdetectors. The Heavy Flavor Tracker (HFT) is situated in the center of STAR close to the beam pipe and will be able to directly measure the decay vertices of heavy flavor mesons, such as D and B . Outside of the magnet is the Muon Telescope Detector (MTD) designed for the detection of muons, as these are the only particles which pass through all the material of all subdetectors and the magnet. Using the MTD detector, the heavy flavor particles decaying into muons can be studied.

3. Analysis procedure

Non-photonic electrons originate in semileptonic decays of heavy flavor mesons. It is not possible to reconstruct the invariant mass of $D(B)$ meson so we measure continuous spectrum. The contribution of background has to be subtracted.

The non-photonic electron yield is obtained according the following formula

$$N_{npe} = N_{inclusive} \epsilon_{purity} - N_{photonic} / \epsilon_{photonic}, \quad (3.1)$$

where N_{inc} is the inclusive electron yield, ε_{purity} is the purity of the electron yield, $N_{photonic}$ is the photonic electron yield and $\varepsilon_{photonic}$ is the photonic electron reconstruction efficiency. First, the inclusive electron sample is obtained and corrected with the purity for hadron contamination. Second, the background represented by photonic electrons has to be subtracted. Photonic electrons are those created in pairs e^+e^- . They come mainly from γ conversions or Dalitz decays. Only part of the pairs can be completely reconstructed. Therefore, the photonic electron yield needs to be corrected for the photonic electron reconstruction efficiency.

In order to obtain the purity of inclusive electron sample the normalized electron energy loss distribution is fitted with multi-Gaussian function at various p_T bins. Figure 2 (left) shows one p_T bin. The multi-Gaussian function is used due to hadron contamination, which is denoted in different colors in Fig. 2 (left). The dashed pink line represents π , the dot-dashed blue line K , the dashed red line are electrons, dot-dashed cyan color stands for protons and finally the dotted green line are the so called merged pions which are just wrongly reconstructed two tracks as one. The purity is then defined as the ratio of electron Gaussian to the multi-Gaussian within the $n\sigma_e$ cut.

In Fig. 2 (right) the invariant mass of electron pairs at $0.8 < p_T < 8.5$ GeV/c is shown. Electrons are paired with each other and grouped together according their charges. The unlike-sign distribution represents all e^+e^- pairs while like-sign distribution characterises the combinatorial background which is subtracted from the unlike-sign pairs. The resulting distribution contains the real photonic electrons as can be seen in Fig. 2 (right): only at low m_{ee} there are entries reflecting the low invariant mass of γ or π^0 , η Dalitz decays.

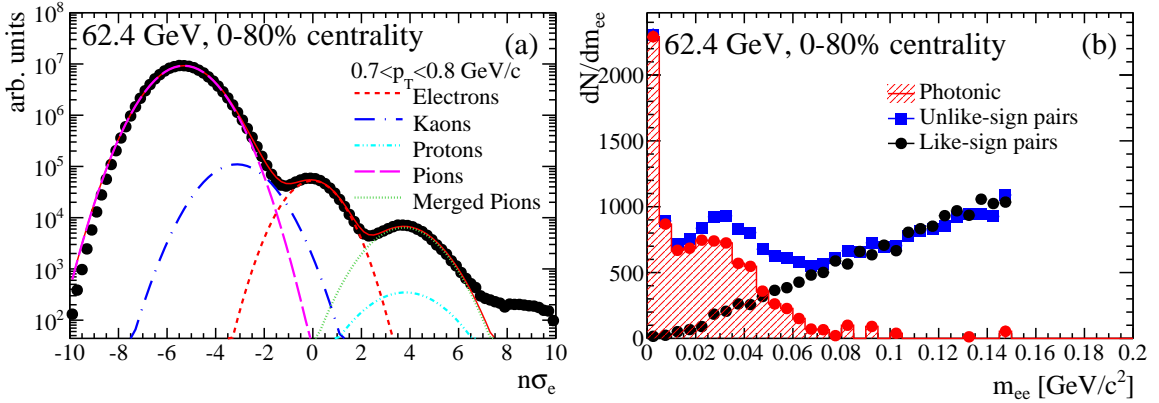


Figure 2: Left: Electron energy loss distribution. Taken from ref. [13]. Right: Invariant mass of electron pairs. Taken from ref. [13].

4. p+p collisions at $\sqrt{s} = 200$ GeV

The invariant yield of non-photonic electrons in proton-proton collisions at $\sqrt{s} = 200$ GeV is important as a test of perturbative QCD calculations. In Fig. 3 (left) the invariant yield of NPE is plotted as a function of transverse momentum p_T . Published STAR data from year 2008 [14] and published PHENIX results from year 2005 [6] are drawn in Fig. 3 together with the preliminary results of STAR from years 2009 and 2012. In the first case the NPE spectra were extended towards lower p_T and the latter analysis results were obtained up to $p_T = 14$ GeV/c. However, in Fig. 3 the

spectra are drawn only up to $p_T = 8 \text{ GeV}/c$ for better comprehensibility. On the same plot the data are compared to the theoretical calculations of Fixed Order Next-to-Leading Logarithm (FONLL) of pQCD [15].

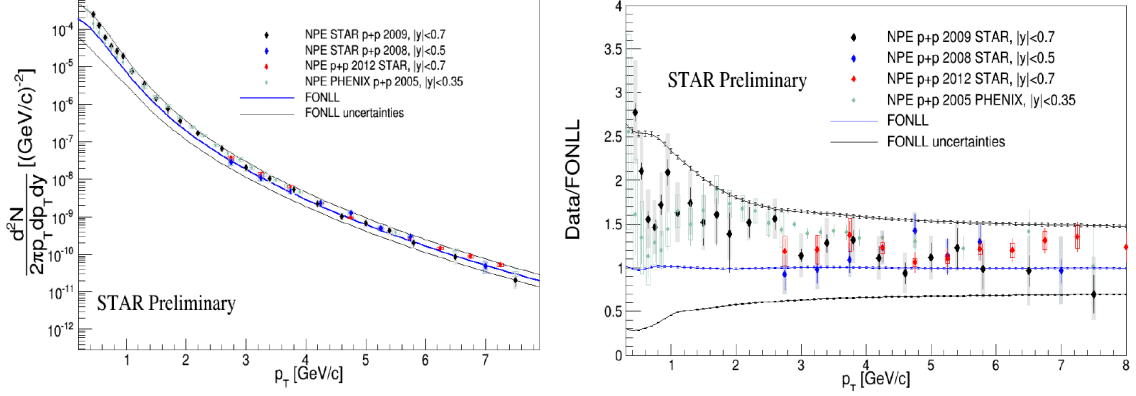


Figure 3: Left: Invariant yield of non-photonic electrons compared to FONLL pQCD calculations from ref. [15]. Published STAR data from year 2008 [14], PHENIX results from year 2005 [6], as well as the preliminary STAR results from years 2009 and 2012 are shown. Right: Ratio of measured invariant yield of non-photonic electrons to FONLL pQCD theoretical calculations. Taken from ref. [14], [6], [15].

The data agree well with each other and are consistent with the FONLL pQCD calculations within their uncertainties. This can be seen in Fig. 3 (right) where the ratio of the data to FONLL calculations is shown [14].

5. Au+Au collisions at $\sqrt{s_{NN}} = 200 \text{ GeV}$

The nuclear modification factor R_{AA} as defined above can reveal the effects of QGP on the particle production. At 0-10 % central Au+Au collisions at the energy of $\sqrt{s_{NN}} = 200 \text{ GeV}$ the STAR experiment observes a strong suppression of non-photonic electrons at high p_T (Fig. 4 left). The R_{AA} is also compared to theoretical models based on different types of energy loss of heavy quarks inside the QGP.

The DGLV Rad. model [16] marked with dashed green line considers only gluon radiation energy loss mechanism and does not describe the suppression at high p_T . A DGLV model which includes in addition the collisional energy loss (DGLV Rad. + El.) predicts larger suppression compared to the previous one. The non-perturbative approach to quark energy loss presented by He *et al.* [17] is marked with magenta line. The BAMPS partonic transport model [18], [19] marked with black dashed line calculates the quark energy loss due to elastic collisions with the medium. A collisional dissociation model represented by the red line uses the energy loss caused by the dissociation of heavy mesons in the strongly interacting medium [20]. This model, together with the AdS/CFT model [21], agree well with the data at high p_T . Finally, the model described by Gossiaux *et al.* [22], [23] calculates the radiative and collisional energy loss using pQCD description with non-perturbative corrections.

The measurement of elliptic flow of NPE in Au+Au collisions at $\sqrt{s_{NN}} = 200 \text{ GeV}$ is shown in Fig. 4 (right). The v_2 variable was obtained using 2-particle correlations $v_2\{2\}$ or 4-particle

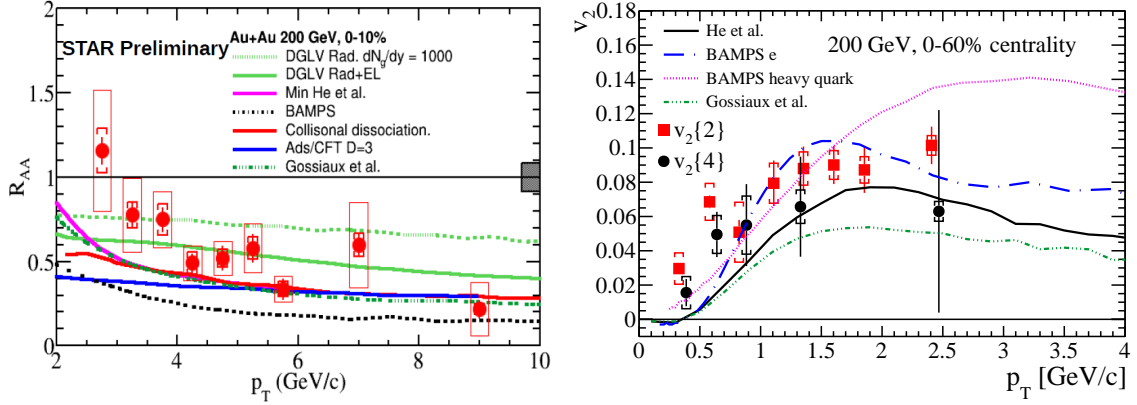


Figure 4: Left: The nuclear modification factor of non-photonic electrons in Au+Au collisions at $\sqrt{s_{NN}} = 200$ GeV compared to models from ref. [16], [17], [18], [19], [20], [21], [22], [23]. Right: The elliptic flow of non-photonic electrons in Au+Au collisions at $\sqrt{s_{NN}} = 200$ GeV compared to models. Taken from ref. [13], [17], [18], [19], [22], [23].

correlations $v_2\{4\}$ [24]. A finite v_2 is observed at low p_T which indicates strong in-medium interactions of heavy quarks [13]. Increasing v_2 at high p_T can be described by jet-like correlations that are also present in p+p collisions. The measurements of elliptic flow are compared to the same theoretical models as is the R_{AA} [17], [18], [19], [22], [23]. In general, models which are able to reproduce the azimuthal anisotropy do not describe well the nuclear modification factor.

6. Au+Au collisions at $\sqrt{s_{NN}} = 39, 62.4$ GeV

In Au+Au collisions at lower beam energies of $\sqrt{s_{NN}} = 62.4$ GeV the NPE measurements are not suppressed. The preliminary results on R_{AA} of NPE at the energy of $\sqrt{s_{NN}} = 62.4$ GeV are shown in Fig. 5 (left). The Au+Au NPE yield was divided by the spectra calculated theoretically using pQCD [25]. The PHENIX experiment revealed the same pattern of R_{AA} of heavy flavor electrons at this beam energy [26]. The enhancement of nuclear modification factor can be caused by Cold Nuclear Matter effects (e.g. the Cronin effect), which seems to be more significant at lower beam energies and need to be studied in the future.

The azimuthal anisotropy using 2-particle correlations $v_2\{2\}$ was also measured at low beam energies of $\sqrt{s_{NN}} = 39$, and 62.4 GeV, which can be seen in Fig. 5 (right). While the elliptic flow v_2 at $\sqrt{s_{NN}} = 200$ GeV has positive values, at lower collisional energies it is consistent with zero up to $p_T = 1.6$ GeV/c. The difference between energy $\sqrt{s_{NN}} = 200$ GeV and the lower beam energies are statistically significant [13].

7. Conclusions

In this proceedings the recent STAR results of electrons originating from decays of open heavy flavor mesons were discussed. First, the NPE spectra in p+p collisions at $\sqrt{s} = 200$ GeV were shown and compared to theoretical predictions of FONLL pQCD calculations. The data from different years agree with each other as well as with the PHENIX results and FONLL calculations

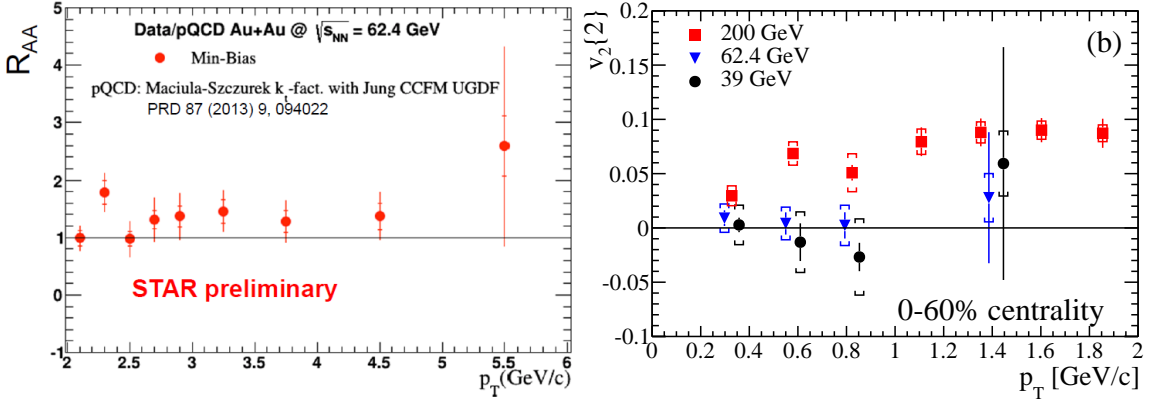


Figure 5: Left: The nuclear modification factor of non-photonic electrons in Au+Au collisions at $\sqrt{s_{NN}} = 62.4$ GeV. The baseline was calculated theoretically using pQCD from ref. [25]. Right: The elliptic flow of non-photonic electrons in Au+Au collisions at $\sqrt{s_{NN}} = 39, 62.4, 200$ GeV. Taken from ref. [13].

within uncertainties. Second, the preliminary results of nuclear modification factor at 0-10% central Au+Au collisions at $\sqrt{s_{NN}} = 200$ GeV was shown and compared to various models. The data reveal strong suppression at high p_T . The comparison with models shows that heavy quarks lose energy in QGP not only through gluon radiation. Also, the elliptic flow v_2 was presented and compared with the same models. Models which describe the R_{AA} are not able to reproduce the azimuthal anisotropy. Finally, the measurements of NPE at lower collisional energies $\sqrt{s_{NN}} = 39, 62.4$ GeV were presented. The nuclear modification factor in Au+Au collisions at $\sqrt{s_{NN}} = 62.4$ GeV was shown with no indication of suppression. These observations demonstrate that Cold Nuclear Matter effects could be more significant at these energies. The elliptic flow at $\sqrt{s_{NN}} = 39$ and 62.4 GeV presented in this proceedings was consistent with 0.

The STAR experiment has been recently upgraded with two new detectors Heavy Flavor Tracker (HFT) and Muon Telescope Detector (MTD) which will help to improve the heavy flavor measurements. The HFT [27] will be able to reconstruct the decay vertices of D and B mesons. The studies of heavy flavor measurements via muon decay channels will be available using the MTD detector ($|\eta| < 0.5$) [28].

Acknowledgements

This work was supported by Grant Agency of the Czech Technical University in Prague, grant No. SGS13/215/OHK4/35/14 and by Grant Agency of the Czech Republic, grant No. 13-20841S.

References

- [1] L. Adamczyk *et al.* (STAR Collaboration), Phys. Rev. D **86**, 072013 (2012).
- [2] L. Adamczyk *et al.* (STAR Collaboration), Phys. Rev. Lett. **113**, 142301 (2014).
- [3] L. Adamczyk *et al.* (STAR Collaboration), Phys. Rev. C **90**, 024906 (2014).
- [4] L. Adamczyk *et al.* (STAR Collaboration), Phys. Lett. B **735**, 127 (2014).

- [5] B. I. Abelev *et al.* (STAR Collaboration), Phys. Rev. Lett. **98**, 19301 (2007); Erratum-ibid. **106**, 159902 (2011).
- [6] A. Adare *et al.* (PHENIX Collaboration), Phys. Rev. Lett. **97**, 252002 (2006).
- [7] A. Adare *et al.* (PHENIX Collaboration), Phys. Rev. Lett. **103**, 082002 (2009).
- [8] A. Adare *et al.* (PHENIX Collaboration), Phys. Rev. C **86**, 024909 (2012).
- [9] A. Adare *et al.* (PHENIX Collaboration), Phys. Rev. Lett. **98**, 172301 (2007).
- [10] A. Adare *et al.* (PHENIX Collaboration), Phys. Rev. C **90**, 034903 (2014).
- [11] A. Adare *et al.* (PHENIX Collaboration), Phys. Rev. Lett. **109**, 242301 (2012).
- [12] A. Adare *et al.* (PHENIX Collaboration), Phys. Rev. Lett. **112**, 252301 (2014).
- [13] L. Adamczyk *et al.* (STAR Collaboration), arXiv: 1405.6348 [hep-ex] (2014).
- [14] H. Agakishiev *et al.* (STAR Collaboration), Phys. Rev. D **83**, 052006 (2011).
- [15] A.D. Frawley, T. Ullrich and R. Vogt, Phys. Rept. 462:125-175 (2008).
- [16] M. Djordjevic, M. Gyulassy, R. Vogt and S. Wicks, Phys. Lett. B **632**, 81 (2006).
- [17] M. He, R. J. Fries and R. Rapp, Phys. Rev. C **86**, 014903 (2012).
- [18] J. Uphoff, O.Fochler, Z. Xu and C. Greiner, Phys. Rev. C **84**, 024908 (2011).
- [19] J. Uphoff, O.Fochler, Z. Xu and C. Greiner, Phys. Lett. B **717**, 430 (2012).
- [20] R. Sharma, I. Vitev and B.-W. Zhang, Phys. Rev. C **80**, 054902 (2009).
- [21] W. Horowitz, AIP Conf. Proc. **1441**, 889-891 (2012).
- [22] P. Gossiaux and J. Aichelin, Phys. Rev. C **78**, 014904 (2008).
- [23] P. Gossiaux, J. Aichelin, T. Gousset and V. Guiho, J. Phys. G **37**, 094019 (2010).
- [24] N. Borghini, P. M. Dinh and J.-Y. Ollitrault, Phys.Rev. C **63**, 054906 (2001).
- [25] R. Maciula and A. Szczurek, Phys. Rev. D **87**, 094022 (2013).
- [26] A. Adare *et al.* (PHENIX Collaboration), arXiv: 1405.3301[nucl-ex] (2014).
- [27] E. Anderssen *et al.*, A Heavy Flavor Tracker for STAR:
<http://www.osti.gov/scitech/servlets/purl/939892>.
- [28] L. Ruan *et al.*, STAR Muon Telescope Detector Proposal:
http://www.star.bnl.gov/~ruanlj/MTDreview2010/MTD_proposal_v14.pdf.